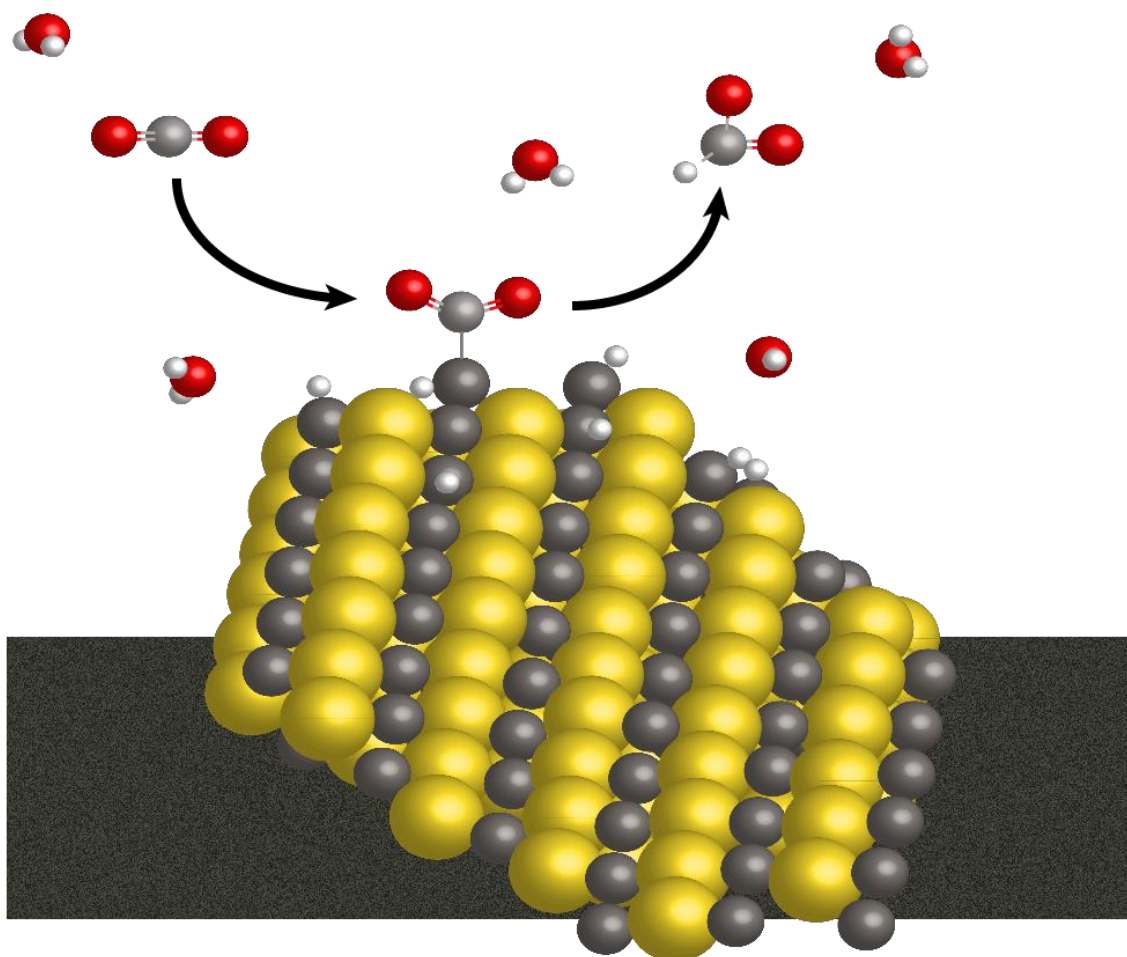# The influence of $Cu_{2-x}S$ nanoparticles on the electroreduction of CO_2

Master thesis, 2019

Kristiaan H. Helfferich
Under daily supervision of: Christa van Oversteeg, Msc.; Marisol Tapia Rosales, Msc.
Main supervisor: Prof. dr. Petra de Jongh
Second examiner: Dr. Celso de Mello-Donega
Utrecht University

Abstract

With CO_2 playing a profound role in climate change, valorizing CO_2 is receiving increasing attention. A promising route is to use CO_2 as a feedstock to produce hydrocarbons by CO_2 Reduction Reaction (CO_2RR). Previous research showed the formation of various C_1 and C_2 hydrocarbons through CO_2RR using Cu catalysts, albeit with relatively low activity and low selectivity. A potential strategy to achieve higher selectivity is to introduce p-block elements into the Cu crystal since these may participate in bond formation at the surface, thus circumventing scaling relations. In this work CuS and Cu_2S nanoparticles were scrutinized for CO_2RR. These nanoparticles were synthesized by incipient wetness impregnation and heating up synthesis. This produced graphite nanoplatelets (GNP) supported Cu_{2-x}S nanoparticles and colloidal Cu_{2-x}S nanoparticles respectively.

X-ray diffraction showed monophasic CuS/GNP and Cu_2S/GNP nanoparticles. Transmission electron microscopy revealed for both colloidal and impregnated samples that Cu_2S nanoparticles favored spherical morphology. The diameter of Cu_2S/GNP nanoparticles was 14.5±2.5 nm and the diameter of colloidal Cu_2S nanoparticles was 10.2±1.0 nm. CuS favoured the formation of nanoplatelets. The CuS/GNP nanoparticles were 43.7±8.9 nm long and 15.2±8.9nm wide. The colloidal CuS nanoparticles were 20.7±2.7 nm long and 8.7±1.4 nm wide.

After synthesis, the nanoparticles were deposited on carbon paper substrates. Scanning electron microscopy verified the homogeneous dispersion of individual Cu_2S and Cu_2S carbon supported nanoparticles. These Cu_{2-x}S loaded electrodes were then electrochemically evaluated for CO_2RR. Cyclic voltammetry revealed the immediate reduction of both CuS/GNP and colloidal CuS nanoparticles to presumably another Cu_{2-x}S phase under production of H_2S(g). For both Cu_2S/GNP and colloidal Cu_2S this reduction was less apparent. However, in-situ x-ray absorption fine structure spectroscopy suggested the partial reduction of CuS/GNP to Cu_2S/GNP and metallic Cu(s) at -1.2V vs RHE. Cu_2S/GNP seemed to partially reduce to Cu/GNP.

Gas chromatography and high-performance liquid chromatography were employed to analyze gaseous and liquid product selectivity respectively. Both Cu_{2-x}S/GNP catalysts showed the production of formate with approximately 12% faradaic efficiency at -0.9V vs RHE with 4.28 μmol/h formate production for Cu_2S/GNP and 2.72 μmol/h formate production for CuS/GNP. The remainder of faradaic efficiency was attributed to hydrogen production. It could not be established to what extent the Cu_{2-x}S nanoparticles were active for HER due to the high activity of GNP for HER. No HPLC for CO_2RR on colloidal Cu_{2-x}S nanoparticles was performed at -0.9V vs RHE to observe formate production, but the selectivity for HER with both CuS and Cu_2S was minor.

List of abbreviations

Ag/AgCl - Silver/Silver chloride reference electrode
CA – Chronoamperometry
CO_2RR – CO_2 Reduction Reaction
CV – Cyclic Voltammetry
DDT – 1-Dodecanethiol
DFT – Density Functional Theory
DLC – Double-Layer Capacitance
ECSA – Electrochemically active surface area
ED – Electron Diffraction
EDX – Energy dispersive X-rays
EIS – Electrical Impedance Spectroscopy
ESRF – European Synchrotron Radiation Facility
FTO – Fluorine-doped Titanium oxide
GC – Gas Chromatography
GDE – Gas diffusion Electrode
GNP – Graphite nanoplatelets
HER – Hydrogen Evolution Reaction
HPLC – High Performance Liquid Chromatography
IPA – Isopropanol
IWI – Incipient Wetness Impregnation
LE – Ligand exchange
NHE – Normal Hydrogen Electrode
OA – Oleic acid
OLAM – Oleylamine
RHE – Reversible Hydrogen Electrode
RID – Refractive index detector
SEM – Scanning Electron Microscopy
SHE – Standard Hydrogen Electrode
TEM – Transmission Electron Microscopy
TOPO – Trioctyl phosphine oxide
UPD – Underpotential Deposition
XAFS – X-ray Absorption Fine Structure
XRD – X-ray Diffraction

Contents

1. Introduction

1.1 Relevance CO$_2$ valorization

With CO$_2$ being a major industry waste product and its profound role in global warming, global efforts are made to reduce its emissions.[1] There are two main approaches for this; Carbon Capture and Storage (CCS) and Carbon Capture and Utilization (CCU). While CCU is economically more challenging, using CO$_2$ as feedstock allows for sustainable production of chemicals and fuels.[2,3]

Once captured, a promising way to valorize CO$_2$ is the electrochemical reduction of CO$_2$ – commonly referred to as CO$_2$ Reduction Reaction (CO$_2$RR).[4,5] This process utilizes a power supply to thermodynamically drive the reduction of CO$_2$ over a metal surface as depicted in Figure 1. Herein, water is oxidized on a platinum anode forming oxygen and protons. A proton exchange membrane can then pass these protons to the cathode compartment. In the cathode compartment the feedstock CO$_2$ is reduced with the former protons and electrons from the power supply. Using a renewable energy source for this power supply makes the process carbon neutral. A major advantage of this technique, as opposed to hydrogenation of CO$_2$, is that no separate hydrogen production needs to be addressed as protons for CO$_2$ reduction are provided by the oxidation of water.
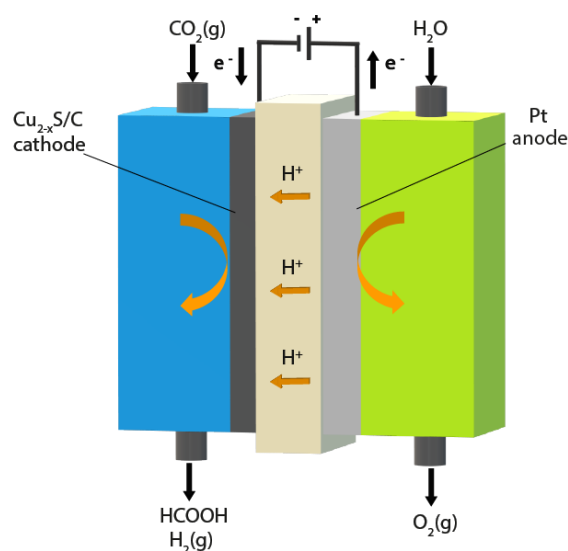

Figure 1: A simplified illustration of CO$_2$ electroreduction in a fuel cell. H$_2$O is oxidized at the Pt anode to produce protons for subsequent reduction of CO$_2$ on the Cu cathode.

Pioneered by Hori et al. in the 1980's, various transition metals were screened for the electroreduction of CO$_2$.[6] It was reported that the product selectivity depends greatly on the metal electrodes used.[7,8] Ultimately, Cu electrodes proved to be the most efficient in the conversion of CO$_2$ to a wide range of hydrocarbons and oxygenates – see Figure 2, typically C$_1$ and C$_2$. CO$_2$RR involves complex reaction mechanisms requiring a great number of electrons to be transferred. Unfortunately, this results in rather low activity and the efficiency of the desired reduction reaction with respect to other faradaic processes needs to be increased (higher faradaic efficiency).[9-11] This low faradaic efficiency is mainly attributed to the competition of the Hydrogen Evolution Reaction (HER).[12,13] Furthermore, the poor selectivity and a high overpotential – the potential difference between the working electrode and the theoretical half-cell value – hamper

the CO_2RR from being an attractive process. Therefore, new catalysts need to be designed with a higher selectivity and activity for CO_2RR to make the process industrially relevant.
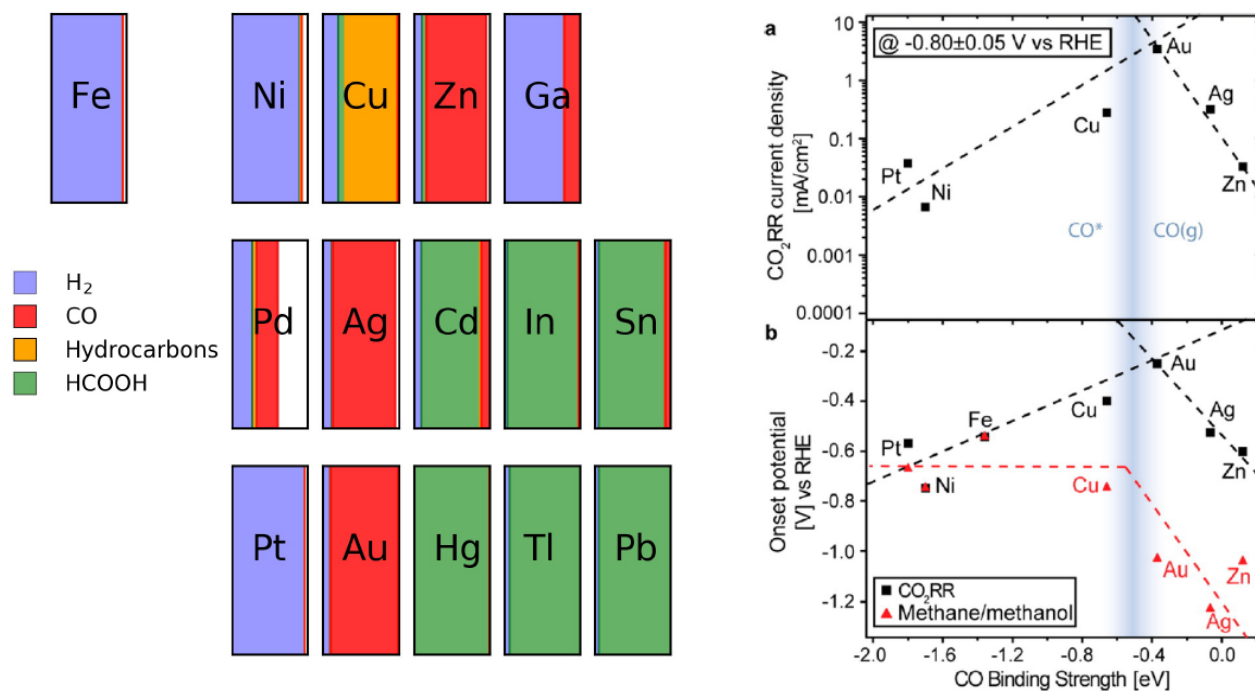

Figure 2: left) A schematic overview of transition metals probed for CO_2RR regarding selectivity, only Cu is promising for production of hydrocarbons. Adopted from Ida Hjorth (2017).[57] right) Graphs showing the activity and overpotential of certain transition metals for CO_2RR. Gold is among the most active at low overpotential. Adopted from Kendra Kuhl et al. (2012)

1.2 Cu$_{2-x}$S nanoparticles

Copper sulfides compositions can be abbreviated with the structure formula Cu$_{2-x}$S, in which x represents the amount of Cu vacancies in the crystal. x=0 constitutes chalcocite (Cu$_2$S) and x=1 covellite (CuS), as shown in Figure 3. However, a wide range of Cu:S compositions exist with different properties. Thus, controlling the size and composition of Cu$_{2-x}$S nanoparticles allows for a certain degree in tunability of its properties. Cu$_{2-x}$S compounds also have rather low toxicity and are of relatively low cost.[14]

Furthermore, the material is a p-type semiconductor with a band-gap ranging from 1.2 eV to 2.0 eV. For these reasons, Cu$_{2-x}$S nanomaterials are of great interest to optoelectronic research.[15-17]

Recent Density Functional Theory (DFT) studies showed that the compound had modified binding energies for key intermediates that are potentially beneficial to improving selectivity.[18,19] Perhaps S^{2-} may also participate in bond breaking/formation. Hence, Cu$_{2-x}$S materials were also investigated for CO$_2$RR; e.g. using CuS microcubes for CO$_2$RR [4] and using Cu$_{2-x}$S nanoparticles to increase the selectivity towards alcohols.[20] Although more interest in Cu$_{2-x}$S materials for CO$_2$RR is emerging, there is still a lot unknown about Cu$_{2-x}$S as CO$_2$RR electrocatalyst. It would be interesting to gain a better understanding regarding structure-functional relationships. Particle size effect studies could proof useful in the same way these have been done for CO$_2$RR with Cu nanoparticles.[21] Secondly, CO$_2$RR dependence on composition and geometry of Cu$_{2-x}$S nanoparticles may be beneficial as promotion of facets that have favorable adsorption energies for reaction intermediates can boost activity/selectivity.
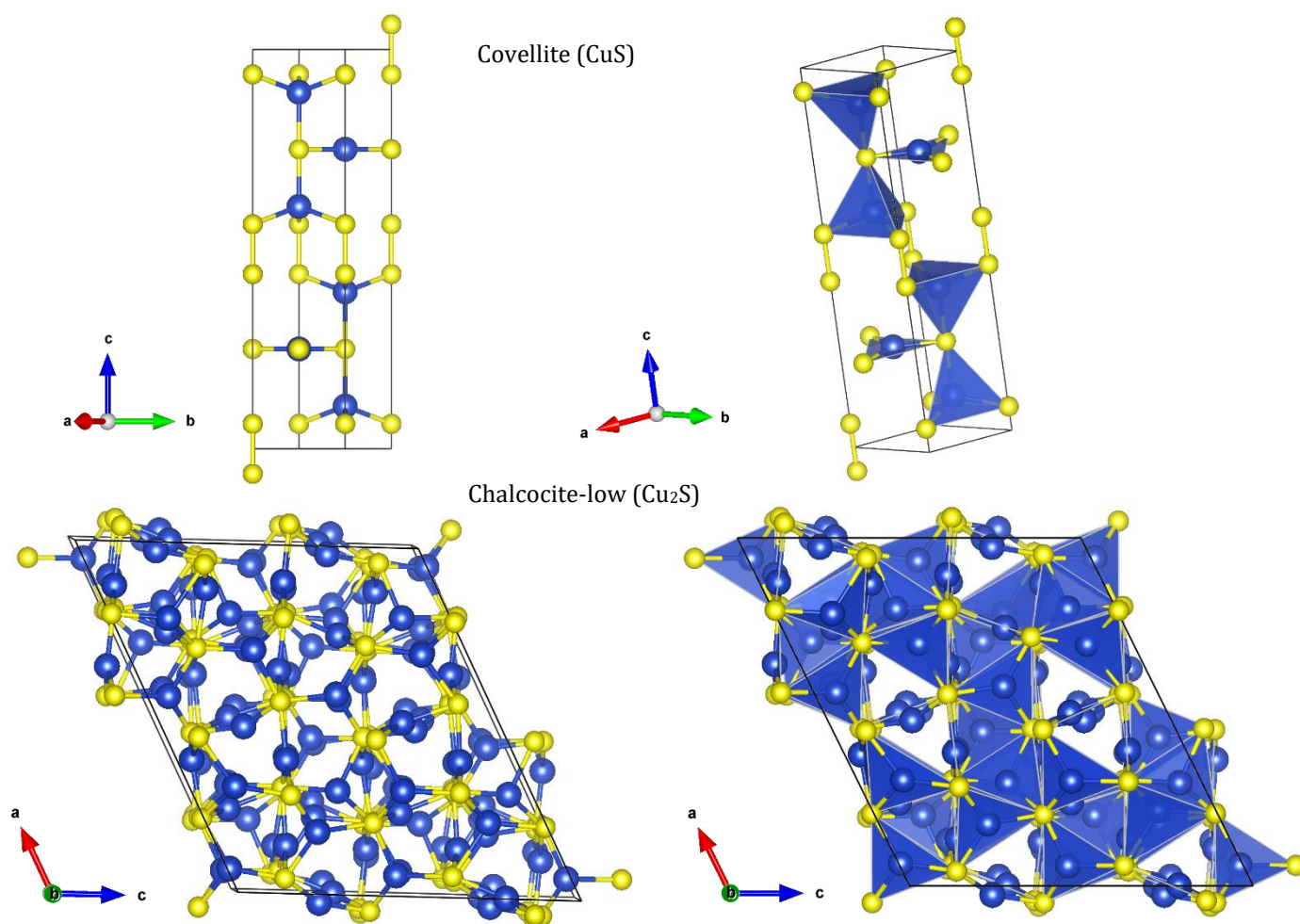

Covellite (CuS)

Chalcocite-low (Cu$_2$S)

Figure 3: Unit cells of covellite (CuS) and Chalcocite-low (Cu$_2$S) crystal structures made with Vesta based on experimental data. Blue = Cu and Yellow = Sulfide.

1.2 Approach

In this work $Cu_{2-x}S$ nanoparticles were investigated to help bridge the knowledge gap for CO_2RR with $Cu_{2-x}S$. The focus was thereby to gain a better understanding of how differently sized and composed $Cu_{2-x}S$ nanoparticles in terms of morphology and Cu:S stoichiometry, influence the activity, selectivity and stability of CO_2RR.

To achieve this, first $Cu_{2-x}S$ nanoparticles had to be synthesized. For that purpose, CuS and Cu_2S were chosen to represent the boundaries of possible $Cu_{2-x}S$ compositions. To assess the influence of size and morphology and the influence of their synthesis, two different synthesis approaches were chosen.

The first method was incipient wetness impregnation. The relatively facile synthesis is relevant for its applicability in industry. However, electrochemical reactions inherently require conductive materials. Therefore, a carbon support, graphite nanoplatelets (GNP), was chosen as support for this synthesis. Additionally, GNP offers a high surface area to support $Cu_{2-x}S$ nanoparticles on which is beneficial to surface-dependent reactions like CO_2RR. The other method used was a colloidal heating up synthesis to make CuS/Cu_2S nanoparticles. This method allowed for the greater particle size and composition control.

The synthesized nanoparticles could then be used to fabricate electrodes so that the different $Cu_{2-x}S$ catalysts could be scrutinized for electroreduction of CO_2. Finally, the catalysts were subjected to different potentials, blank tests and complementary analysis techniques to elucidate the performance of $Cu_{2-x}S$ catalysts in CO_2RR regarding the activity, selectivity and stability. A graphical abstract of the research is shown in Figure 4 for clarification.
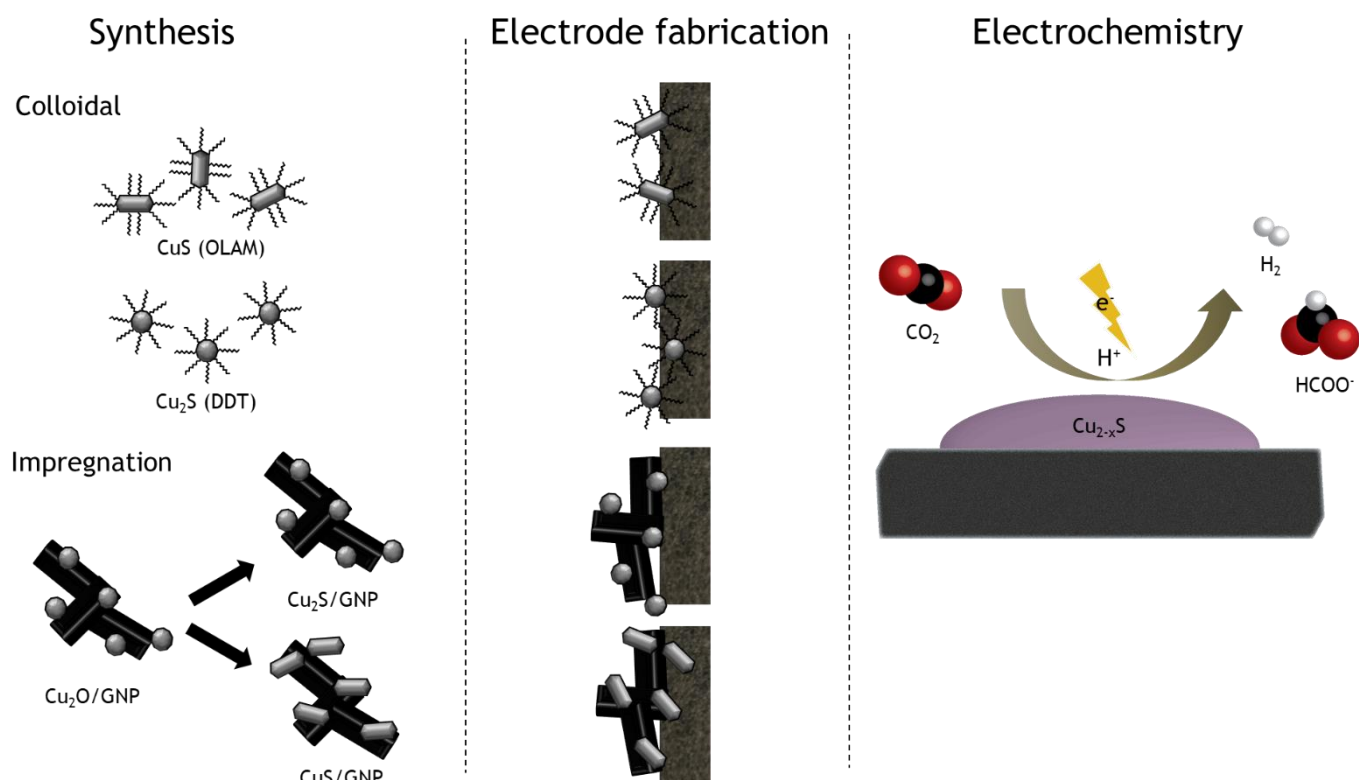

Figure 4: Graphical abstract of the project. 1) Synthesis of $Cu_{2-x}S$ nanoparticles by impregnation and colloidal synthesis. 2) Electrode fabrication by spraying inks of $Cu_{2-x}S(/GNP)$ nanoparticles on carbon paper. 3) Electrochemical evaluation of the as prepared catalysts.

2. Theory

2.1 General electrochemistry

For any electrochemical reduction reaction an oxidizing agent is reduced with a certain number of electrons dictated by the stoichiometry of the reaction:

$$Ox + ne^- \leftrightarrow Red$$
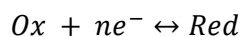
Where n is the moles of electrons, the reaction can be evaluated with thermodynamics if the system is in equilibrium. The general thermodynamic expression for the Gibbs free energy is:

$$\Delta G = \Delta G^{\ominus} + RTln(Q)$$

In this equation ΔG is the Gibbs free energy, $\Delta G^{\ominus}$ the standard state Gibbs free energy, R the gas constant, T the temperature and Q the equilibrium quotient. With ΔG<0 representing a spontaneous reaction, it becomes possible to determine the outcome of a reaction. Another expression for the Gibbs free energy in electrochemistry is:

$$\Delta G = -nFE$$

Where n is the moles of electrons that is required in the reduction equation, F is the faradaic constant and E is the electrochemical potential difference in the cell. Considering that ΔG<0 for a spontaneous reaction, the potential for that reaction should be E>0.[22] The combination of equation 1.2 and 1.3 gives the Nernst equation;

$$E = E^{\ominus} - \frac{RT}{nF}ln(Q)$$

Herein, E is the the potential difference of a cell and $E^{\ominus}$ the standard electrode potential.[22] This equation is highly important in electrochemistry because it states the reduction potential as function of temperature, standard reduction potential and activities of the reduced and oxidized species involved. In an ideal solution (i.e. the enthalpy and volume change of mixing is zero) the potential is dependent on the concentration of reactants and products. This is however not the case when using ions to facilitate electrochemical reactions. Therefore, the activity of the ions involved (b) needs to be used considered. The equation for the equilibrium quotient then becomes;

$$Q = \frac{m_{red}}{m_{ox}}$$

With

$$m_x = \gamma \frac{\alpha}{\alpha_0}$$

Where m_x is the effective concentration of compound x, γ is the activity coefficient and m_x is the activity coefficient for compound x.[22] Typically values for activity coefficients are experimentally determined and found in literature. It should be noted that the Nernst equation only applies when no current flows through a cell. When a potential is applied to a cell that induces a current flow, a potential equal to the standard reduction potential will no longer suffice to bring about that reaction; a higher potential is then required, the overpotential η. The overpotential can be divided into three terms:

$$\eta = \eta_{act} + \eta_{Ohm} + \eta_{Conc}$$

With η_{act} the overpotential that is required to overcome the activation barrier for a reaction, η_{Ohm} the overpotential that is associated with resistive losses as consequence of current flow through the cell and η_{Conc} is the overpotential that is related to the depleting concentration of charge carriers upon polarization of the electrical double layer present at the interface of a solid electrode surface and the liquid electrolyte that make up an electrochemical cell.[23]

Measuring the potential that is required brings about another challenge. Typically, a reference electrode is used with a known potential compared to the standard reduction reaction for hydrogen:

$$2H^+ + 2e^- \rightarrow H_2(g)$$
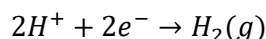
The standard reduction potential of this reaction is set to zero ($E^0 = 0$). There are multiple ways to report the potential applied for an electrochemical reaction. In literature reporting the potential against the Standard Hydrogen Electrode (SHE) is favored. The SHE assumes working under standard pressure ($p_{H_2} = 1\ bar$), using an ideal platinized platinum electrode and the activity of protons in solution to be; $\alpha_{H^+} = 1$. Since this is an impractical way to report a potential value against, it is common to report of potential values versus the Normal Hydrogen Electrode (NHE) using a reference electrode with known potential.[24] For practical reasons all potentials measured in this work were reported in another sub-type of the SHE; the Reversible Hydrogen Electrode (RHE). RHE is dependent on the pH. Typically, a reference electrode with a known potential is used to determine the potential vs RHE. A commonly used reference electrode, that was used in this work, is the Ag/AgCl electrode;

$$AgCl(s) \leftrightarrow Ag^+ + Cl^-$$
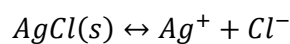
The standard potential for which is +0.22249V at 25°C.[25] The potential measured with the reference electrode is then converted to the potential versus RHE using the following relationship;

$$E_{RHE} = E_{Ref} - \frac{RT}{F}ln(\alpha_{H^+}) + E_{Ag/AgCl}$$

Where E_{RHE} is the potential versus RHE, E_{Ref} is the potential versus the reference electrode and $E_{Ag/AgCl}$ is the concentration dependent potential for the Ag/AgCl reaction. Typically, the values for the latter are tabulated. Commonly, the above equation is simplified to:

$$E_{RHE} = E_{Ref} + (0.05916\ x\ pH) + E_{Ag/AgCl}$$

Where the +0.05916 originates from the conversion of RT/F (with T=298K) and the conversion factor of $ln(\alpha_{H^+})$ to $log(\alpha_{H^+})$. Subsequent substitution of $-log(\alpha_{H^+}) = pH$ yields the equation as shown above.

2.2 The electrode

The interface between the solid electrode and the liquid electrolyte is an important concept in electrochemistry. There are several models for the electrode-electrolyte interface, but for simplicity only the Stern model is shown in Figure 5. Depending on the potential applied to the electrode, the electrode surface will either be positively or negatively charged. Counter-charged
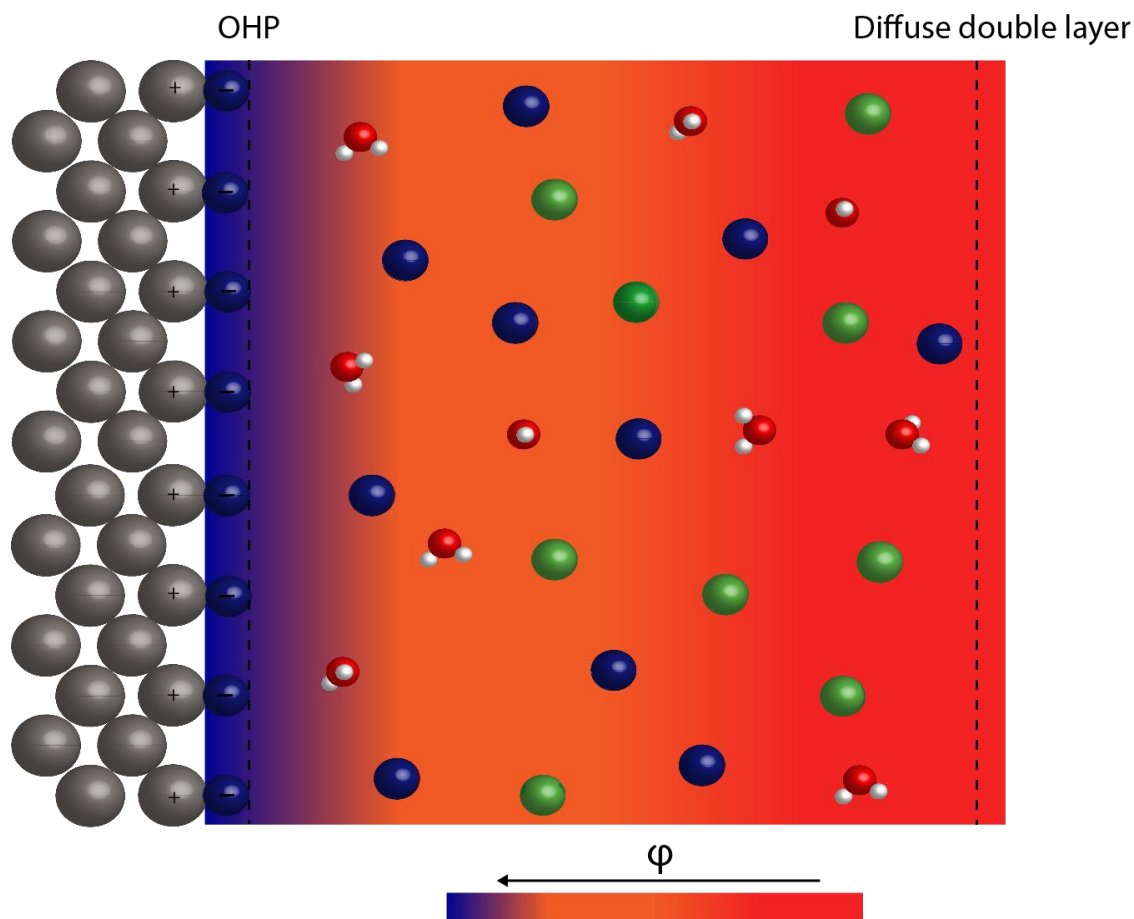

Figure 5: Schematic illustration of the double electrical layer and diffusion layer near a metallic electrode.

ions are therefore attracted to the electrode. These ions make up the Helmholtz plane consisting of the Inner Helmholtz plane (IHP) and the outer Helmholtz plane (OHP). Outside the OHP also other ions are present. Hence, a potential gradient ($\Delta\varphi$) is present across the double electrical layer. Reducible species within the diffusion layer outside the Helmholtz plane can diffuse to the electrode so that reduction can occur.

Furthermore, the electrical double layer's charging behavior means that it can be treated as a capacitor. The capacitance (C_{dl}) of which is given by:

$$i_c = C_{dl}(E)\frac{dE}{dt}$$

In which i_c is the charging current and $\frac{dE}{dt}$ is the differential of potential over time. By scanning over a potential range in a non-faradaic region (i.e. no product formation), the charging current can be determined to yield the capacitance of an electrode. The capacitance can be used to determine the electrochemically active surface area (ECSA) of an electrode by cross-referencing the measured double layer capacitance (F) of a sample with a specific capacitance (F/cm²).[26] This is further explained in appendix 9.1.

2.3 Electrochemical reduction

In electroreduction, a power supply is connected to an electrical circuit. With the negative side of the power supply connected to the cathode (which is called the working electrode) and the positive side to the anode. In other words, a negative potential is applied to an electrochemical cell. This negative potential induces a current flow in the cell from the electrode to the electrolyte solution (a reducing current).[27] As illustrated in Figure 6, the negative potential increases the energy of electrons in the electrode. An electron from the electrode can then transfer to an
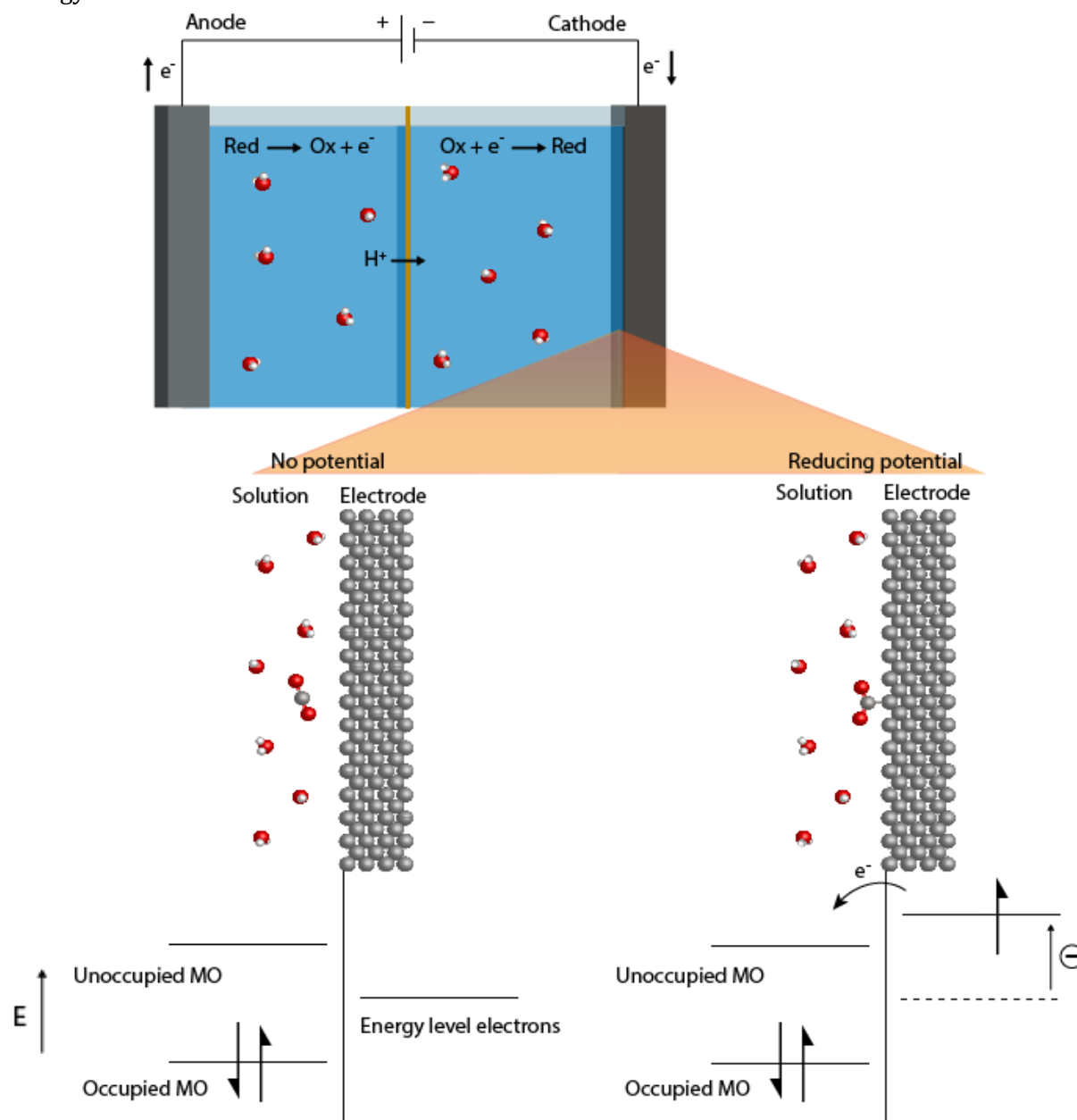
Figure 6: Overview of an electrochemical cell and Molecular Orbital (MO) diagrams when no potential and a reducing potential are applied. Adapted from Bard and Faulkner.14

unoccupied molecular orbital of an adsorbed molecule with lower energy. In which the amount of chemical reaction caused by the flow of electrons is proportional to the amount of electricity passed according to Faraday's law. This transfer of electrons from the electrode to the solution is therefore commonly referred to as a faradaic process.[27]

There are different mechanisms for CO_2RR on Cu found in literature. Yet it is generally found that the production of $HCOO^-$, CH_4, CH_3OH arises from Cu(111) whereas C_2H_4 and C_2H_5OH production is predominant on the Cu(100) plane.[10,11,28,29,21] These simplified mechanisms are illustrated in Figure 7. With $Cu_{2-x}S$, DFT calculations show that the sulfide weakens the adsorption energies for HCOO* and *COOH such that the formation of CO is suppressed and the formation of HCOO* to

Figure 7: Simplified CO_2RR mechanisms for Cu(111) and Cu(100) planes. Adapted from Kortlever et al. 2015.

formate is favored.[18] Thus the formation of $HCOO^-$ is expected when using $Cu_{2-x}S$ catalysts.

2.4 The electrolyte

The large number of protons required for the reactions (along with HER), means that substantial concentration of OH⁻ is formed near the electrode-electrolyte interface. Hence, the pH increases significantly as opposed to the bulk of the electrolyte. Therefore, in electrochemistry the bulk pH is distinguished from the local pH.[27] The local pH also has a drastic impact on the selectivity of CO_2RR. Hori et al. (1983) found that decomposition of HCO_3^- to CO_2 was required before electroreduction could take place.[30] Therefore, they concluded that dissolved CO_2 is the reducible species in CO_2RR. Unfortunately, CO_2 dissolves poorly in high pH.

Selecting the right electrolyte may keep the local pH from significantly fluctuating with respect to the bulk pH. Another important factor for the electrolyte is its concentration since electrolyte resistance may dominate the current flow through an electrochemical cell when low concentrations are used, even though HER is less prominent in lower concentrated electrolytes.[27,31] A commonly used aqueous electrolyte used for CO_2RR is $KHCO_3$.[32] Therefore this electrolyte is also used in this work.

2.5 Kinetics of electroreduction

Until now only thermodynamics have been discussed. A reaction may not occur at a significant rate even when the potential applied overcomes the activation energy of a certain electrochemical reaction. Therefore, it is also important to consider the kinetics of CO_2RR. Consider the following electrochemical reaction:

$$Ox + ne^- \leftrightarrow Red$$
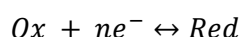
The rate of the reduction reaction is proportional to the current flow from the electrode to the solution. This proportional relationship is given in this expression:

$$i_c = nFAk_f C_{Ox}$$

In which k_f is the heterogeneous rate constant of reduction (cm/s), A is the surface area (cm^2) and C_{Ox} is the surface concentration of reactant Ox. Using the same expression for the oxidation reaction one gives;

$$i_a = nFAk_b C_{Red}$$

k_b is the heterogeneous rate constant of oxidation, i_a the current from the solution to the electrode and C_{Red} is the surface concentration of reactant Red. The rate constant k is dependent on the potential (E) applied through equation:

$$k = k_0 e^{\frac{-\alpha nFE}{RT}}$$

Resembling the Arrhenius equation, the activation energy (E_a) is included in k_0. A reduction reaction implies that the value for potential E is negative and thus the rate (k) increases with increasingly negative E. When both the forward (reduction) and backward (oxidation) reaction are in equilibrium, the equation below can be derived. This equation is known as the Butler-Volmer equation (when no mass transfer limitations are present).[27,33,34]

$$i = i_0 \{ e^{[\alpha f \eta]} - e^{[(1-\alpha) f \eta]} \}$$

i_0 is the exchange current; $f = \frac{nF}{RT}$; α is the transfer coefficient ranging from 0 to unity and η is the overpotential.[27] Often the current and exchange current are normalized to unit area to yield the current density (J) and exchange current density (J$_0$) respectively. The Butler-Volmer equation and the model where it's based on is an important concept in electrochemistry that describes the relation between the (over)potential and the current for both the anodic and cathodic reaction on the same electrode. In Figure 8 the effects of varying exchange current density and transfer coefficient on the response of faradaic current to the overpotential applied are shown.
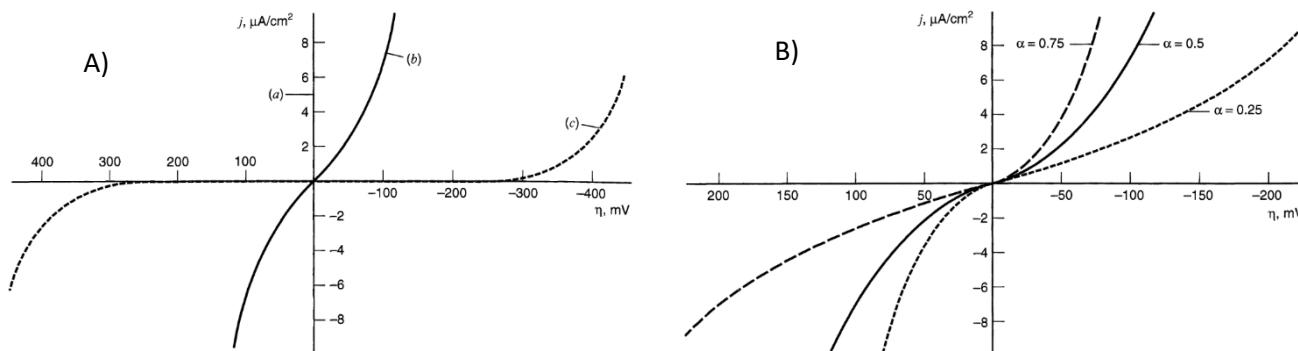

Figure 8: A) Butler-Volmer plots demonstrating the effect of different exchange current densities J; (a) 10^{-3} A/cm^2, (b) 10^{-6} A/cm^2, (c) 10^{-9}A/cm^2. B) Butler-Volmer plots demonstrating varying transfer coefficients. These figures are adapted from Bard and Faulkner.

Another useful relation between the current and overpotential applied is the Tafel equation.[35,36]

$$\eta = a + b\log(i)$$

In this equation, b is the Tafel slope which is a useful indicator of electrocatalytic activity which is independent of surface area. b is obtained by the following relation:

$$b = \frac{dE}{dlog|i|} = \frac{2.3RT}{\alpha nF}$$

The Tafel slope can be obtained by performing linear sweep voltammetry (LSV) scans on an electrochemical cell disregarding mass transfer limitations and electrolyte resistance. Figure 9, demonstrates how the Tafel slope and exchange current can be obtained.
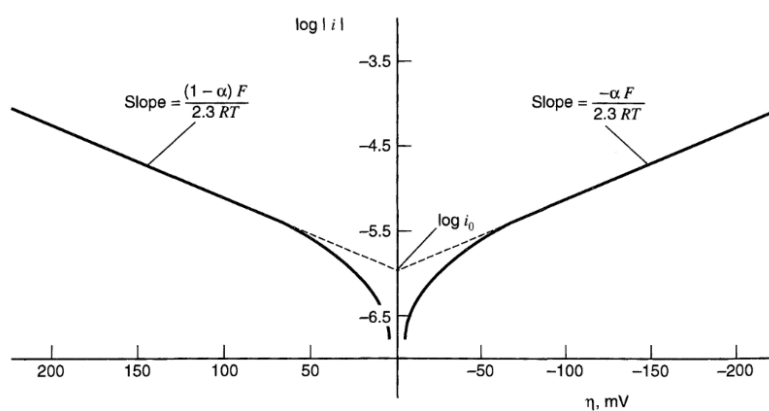

Figure 9: Tafel plots given for the oxidation (left) and reduction reaction (right). Adapted from Bard and Faulkner.

3. Experimental

3.1 Synthesis of $Cu_{2-x}S$ nanoparticles

3.1.1 Incipient wetness Impregnation

Typically, 1 g of vacuum dried graphite nanoplatelets (GNP) was impregnated with the equivalent of its pore volume (0.84 mL/g) of a $Cu(NO_3)\cdot 3H_2O$ solution in 0.1M HNO_3 to achieve a 20 wt% Cu loading. The wetted GNP support was then dried by vacuum overnight. Subsequent heat and reduction treatment at 350°C under 5.5% N_2/NO flow produced monocrystalline Cu_2O/GNP nanoparticles.

Sulfidation to Cu_2S/GNP ensued by weighing 250 mg of Cu_2O/GNP powder in a roundbottomflask with stirring bean. Then 15 mL of 1-dodecanethiol was added and the mixture was heated to 200°C for 2 hours. After cooling down to room temperature the mixture was washed with 15 mL of toluene using centrifugation (5 min @ 2500 rpm). The latter step was repeated another 2 times before leaving the wet Cu_2S/GNP powder to dry in air.

Sulfidation to CuS/GNP was performed by weighing 250mg Cu_2O/GNP powder in a roundbottomflask with stirring bean. Then, 40 mL de-ionized water was added. Finally, 0.107 g of thioacetamide was weighed and added dropwise with 10 mL de-ionized water to the roundbottomflask. The mixture was then refluxed at 130°C for 2h. After cooling down to RT, the mixture was filtrated under vacuum while washing 1L of demineralized water. The filtrate was discarded and the filter with residue was dried under vacuum in a roundbottomflask overnight.

3.1.2 Colloidal synthesis

Cu_2S nanoparticle synthesis was based on the article of van Oversteeg et al.[37] 406mg of $Cu(SO_4)\cdot 5H_2O$ was weighed in a three-necked flask along with 12 mL oleic acid and 15 mL of the sulfur precursor; 1-dodecanethiol (DDT). The mixture was then flushed with N_2 and vacuum in a reflux set-up connected to a Schlenk-line. Subsequent heating to 200°C for 2h enabled nucleation and growth of colloidal Cu_2S nanoparticles. After cooling down to RT the particles were collected by syringe and washed with an excess of a 1:1 MeOH:BuOH mixture in a glovebox. The nanoparticles were centrifuged at 2500 rpm for 5 min, yielding precipitated nanoparticles and the solvent supernatant. The latter was discarded and the nanoparticles were dispersed in an excess of toluene compared to the previously added MeOH:BuOH. The washing step was repeated another 2 times to purify the nanoparticles. Finally, the particles were re-dispersed in toluene.

An adapted method from Y. Xie, G. Bertoni et al (2015) was used for CuS nanoparticle synthesis.[38] 20 mL oleylamine (OLAM), 4 mmol Sulphur powder (99.98%, Sigma-Aldrich) and 20 mL 1-octadecene (ODE) were degassed using a Schlenk line at 130°C under vacuum for 30 min. The yellow solution was then cooled down under N_2 atmosphere to add the Cu precursor. This $Cu(Acetate)_2\cdot H_2O$* powder was added by opening the system to air. Thus, another degassing step of 60 min ensued at RT. The mixture was then heated to 200°C and kept at this temperature for 30 min. After cooling down to RT the solution was collected by syringe and washed with an excess of a 1:1 MeOH:BuOH mixture. Finally, the particles were re-dispersed in 10 mL toluene.

3.1.3 Supported Cu_2S colloidal nanoparticles

0.5 g of High Surface Area Graphite ($HSAG_{300}$)/Graphite Nanoplatelets (GNP_{500})/Vulcan Carbon XC-72R (VC72) was dispersed in 15 mL n-hexane in a centrifuge tube. Then 3 mL of Cu_2S colloidal nanoparticles dispersed in toluene was added. The mixture was then sonicated for 20 minutes in an ultrasound bath. Subsequent centrifugation at 2200 rpm for 5 minutes yielded the precipitated carbon support with its supported Cu_2S colloidal nanoparticles. The transparent supernatant was discarded and the precipitate dried in the parafilm covered centrifuge tube overnight.

3.1.4 S^{2-} Ligand exchange of Cu_2S colloidal nanoparticles

A procedure based on the method from C. van Oversteeg et al. was used for ligand exchange of DDT for S^{2-} with Cu_2S colloidal nanoparticles.[37] In this procedure, 1 mL of Cu_2S colloidal nanoparticles (5mg/mL) was mixed with 1 mL Na_2S in formamide (5 mg Na_2S/1 mL formamide) in a glovebox. The (black) apolar toluene Cu_2S phase segregated from the (transparent) polar formamide phase. With S^{2-} ligand exchange, the Cu_2S nanoparticles transferred to the bottom formamide phase. The now colorless toluene phase was decanted and the dispersion washed, then centrifuged and the nanoparticles were re-dispersed in toluene.

3.2 Electrode fabrication

3.2.1 Drop cast spraying

Generally, 20mg of Cu_xS/GNP was dispersed in 5 mL of Milli-Q water and 1.5 mL of Isopropanol. Subsequent 30 min ultrasound treatment yielded a homogeneous dispersion. The ink was then quickly sprayed over the electrode to prevent precipitation of the Cu_xS/GNP. This occurred by pipetting 0.5mL of the 6.5 mL ink dispersion in an Iwata HP-BP HI Performance Plus airbrush feed. The catalyst ink was then sprayed with 40 psi over a 4.9 cm^2 Toray Gas Diffusion Electrode (GDE) consisting of carbon fiber paper from 10 cm distance – see Figure 10b). The spraying step was repeated one more time to cast 1 mL of the 6.5 mL ink over each electrode. The resulting electrode was left to dry at least 30 min before electrochemical testing.

Since the colloidal $Cu_{2-x}S$ nanoparticles were already dispersed in toluene and highly concentrated, this was used as the ink itself. Therefore, the $Cu_{2-x}S$ dispersion in toluene was quickly sonicated and 50 µL of ink was sprayed over each electrode.

3.2.2 Spray pyrolysis

An ink was prepared of either 20 mg of $Cu_{2-x}S$/GNP catalyst dispersed in 15 mL isopropanol and 30 mL Milli-Q or 2.5 mL colloidal $Cu_{2-x}S$ dispersion was diluted with 45mL toluene (99.8% anhydrous, Sigma Aldrich). The resulting dispersion was sonicated and loaded in a custom build spray pyrolysis set-up – see Figure 10a). Afterwards, the catalysts ink was sprayed in cycles with 15 seconds interval. During each cycle the ink was sprayed with 2mL/min through an ultrasound nozzle on a carbon paper substrate. Meanwhile, the carbon paper substrate was heated to 100°C to allow for quick evaporation of the finely dispersed ink droplets.
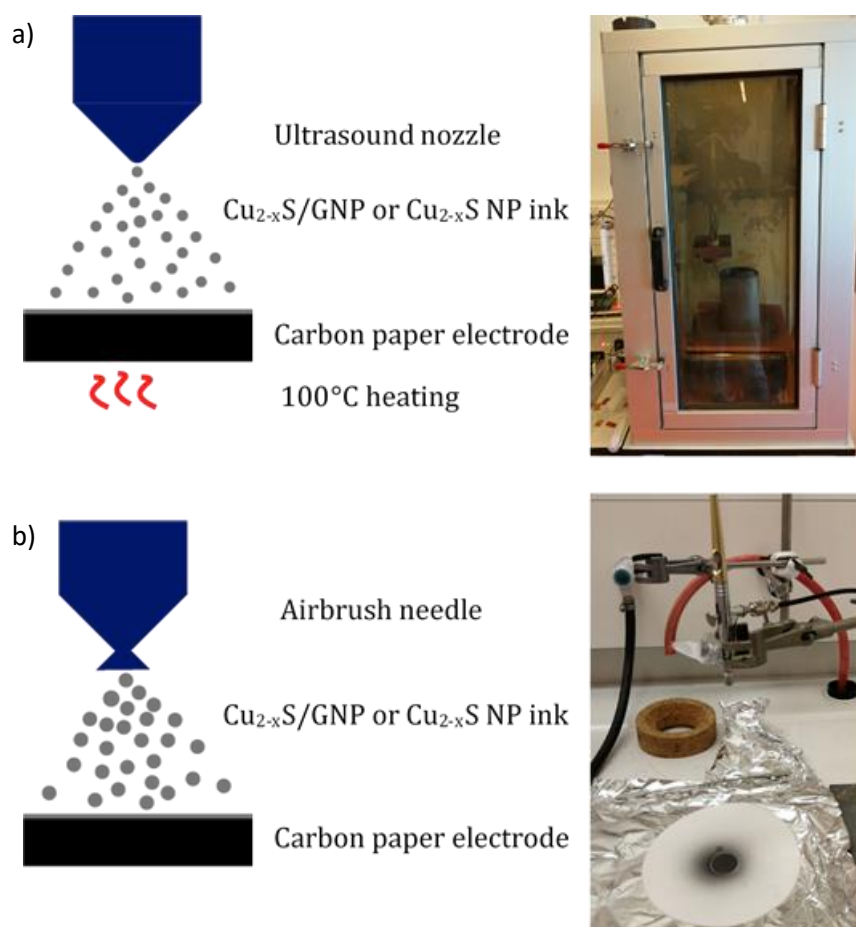

Figure 10: a) A schematic illustration and picture of the spray pyrolysis set-up and b) for the spray pyrolysis set-up.

3.3   Catalyst characterization

3.3.1   Electron Microscopy and Energy dispersive X-rays analysis

For impregnated samples, Cu_xS/GNP powder was dispersed in ethanol and the deposited on either a Holey Cu or Holey Ni grid and left to dry. For colloidal samples toluene was used for dispersion. Typically, TEM images were taken at 120 kV acceleration voltage on a FEI Tecnai 10 electron microscope. For images taken with a FEI Tecnai 20 electron microscope, the acceleration voltage was 200 kV.

Carbon paper supported Cu_xS nanoparticles before and after CO_2RR were analyzed using focused ion beam scanning electron microscopy with energy dispersive X-ray spectroscopy (FIB-SEM-EDX). The analysis was performed on a FEI Helios nanolab 600 Dualbeam with an Oxford instruments Silicon Drift Detector X-Max energy dispersive spectroscope. An electron beam of 5 kV and 0.2 nA was used for EDX mapping.

3.3.2   Electron diffraction (ED)

Electron diffraction experiments were performed using a FEI Tecnai 20 using 100 to 120 kV acceleration voltage. The Aperture length was 310mm for analysis of Cu_2S colloidal nanoparticles. Cu_2S colloidal nanoparticles were dispersed in ethanol and left to dry on a Holey Cu grid after synthesis. Cu_2S nanoparticles were also loaded on a carbon paper electrode with spray pyrolysis and analyzed with chronoamperometry at -1.2V vs RHE for 2h. Colloidal Cu_2S nanoparticles were then collected by immersion of the spent electrode in ethanol assisted with ultrasound. This dispersion was directly dried on a TEM grid for ED analysis.

3.3.2   X-ray diffraction (XRD)

Analysis of the crystal structure of catalysts prepared by IWI was performed by X-ray Diffraction (XRD) on a Bruker D2 Phaser. For this, GNP supported Cu_xS or Cu_2O powder was leveled in a sample holder and analyzed from 25° to 85° using Cu Kα1 radiation (λ=1.5406 Å).

3.3.3   X-ray Absorption Fine Structure (XAFS) spectroscopy

XAFS analysis of the active Cu crystal phase in CO_2RR was done at the Dutch and Belgian beamline (DUBBLE) at the European Synchrotron Radiation Facility (ESRF). A Si (111) crystal was used from 8800 eV to 9500 eV for Cu k-edge (8900 eV) analysis. Ex-situ samples were measured in transmission mode and in-situ samples were measured in fluorescence mode. A custom-built cell from TU Delft was used for the analysis. The data was then normalized and analyzed using Athena XAFS analysis software. The potentiostat used was a SP-240 from Bio-logic Science Instruments.

3.3.4   Underpotential Deposition

Cyclic voltammetry analysis of Cu_2S colloidal nanoparticles loaded electrode was performed to determine the electrochemical active surface area. In 0.1M $HClO_4$ electrolyte a blank scan was recorded from $-0.375V$ to -0.110 V vs Ag/AgCl at 10 mV·s^{-1} after which underpotential deposition (UPD) and stripping of lead was performed in 0.001M PbO_2 + 0.1M $HClO_4$. Subtraction of the blank scan from the lead UPD experiment yielded the current associated with lead deposition.

3.4   Electrochemical measurements

For all electrochemical measurements in Utrecht an Autolab Potentiostat (PGSTAT204) was used. With maximum potential range of +- 10V and a maximum current of +-400mA. Current and Potential accuracy are +- 0.2%. A custom-made H—type electrochemical cell was used with a nafion proton exchange membrane. Ar(g) was fed in the anolyte compartment to induce hydrodynamic stirring and CO_2(g) was fed in the catholyte compartment at 10mL/min. The catholyte compartment had an outlet leading to an online gas chromatograph and the anolyte

compartment had an outlet leading to a vent. The anode was a flat Pt electrode and the $Cu_{2-x}S$ loaded carbon paper electrode was supported with a glassy carbon back-end electrode. As the glassy carbon back-end electrode became dirty under reducing conditions, this electrode was often scrubbed with a cloth using alumina polish and washed after. The reference electrode was an Autolab Ag/AgCl (3M) - EQCM.REF.EL - electrode.

3.4.1   Cyclic voltammetry (CV)

For catalyst performance electrodes were probed by scanning from -0.45 to -2.2V vs Ag/AgCl (3M) reference electrode. Furthermore, cyclic voltammograms in CO_2 saturated 0.1M $KHCO_3$ electrolyte were recorded in non-Faradaic regions at multiple scanning rates to determine the double layer capacitance. The experimental findings were used in approximation of the electrochemically active surface area (ECSA) in an adapted method as reported by E.H. Sargent et al. (2018). Further details are discussed in Appendix 9.1.[20]

3.4.2   Chronoamperometry (CA)

Chronoamperometry (CA) was used to determine the electrochemical activity and selectivity at certain potentials. A fixed potential was applied to the cell and the current was monitored over time. Gas Chromatography and High-performance liquid chromatography was used to determine the selectivity (section 2.4.3 and 2.4.4 respectively).

3.4.3   Gas Chromatography (GC)

For online analysis of products in the gas phase a Global Analysis Solutions Microcompact GC 4.0 was used. The three-channeled system used two Flame ionization detector (FID) and one Thermal conductivity detector (TCD) to allow for detection of hydrocarbons (C_1 to C_3) in the first, CO and methane in the second and H_2, Ar, CO_2 in the third channel respectively. A liquid trap was installed in the front end to prevent bubbles of electrolyte from coming into the GC. Additionally, another gas filter (Veco) was used to condense the electrolyte vapour.

3.4.4 High Performance Liquid Chromatography (HPLC)

Liquid product distribution was analyzed by a Varian HPLC with a HP72C-aminorex column and 1 mMol H_2SO_4 solution as mobile phase. The detector was a Refractive Index Detector (RID). The eluent flow rate was set to 0.55 mL/min and the column temperature was 65°C. The analysis program was 40 min in length.

4. Results

4.1 Synthesis of $Cu_{2-x}S$ nanoparticles

4.1.1 Transmission Electron Microscopy (TEM)

TEM pictures were taken of all $Cu_{2-x}S$ nanoparticles after synthesis to study their size and geometry. Therefore, nanoparticles of a certain sample were loaded on either a Ni or Cu grid and images were taken at different positions to acquire a representative overview of the sample.

In Figure 11, colloidal Cu_2S and CuS nanoparticles are shown. Cu_2S formed spherical nanoparticles that arrange in close-packed aggregates due to their homogeneous size dispersion and favorable ligand-ligand interactions between particles. The blank space in between the particles arises from these DDT ligands. The nanoparticles were measured manually using ImageJ software and a Gaussian distribution was fit through the results. Consequently, the particle size distribution on the right of the Cu_2S image was constructed. The nanoparticles had a diameter of 10.2 ± 1.0 nm.

CuS on the other hand formed distinctive nanoplatelets that also aggregated but not in the same fashion as the Cu_2S nanoparticles. These nanoparticles are stabilized by the OLAM ligands following synthesis. A particle size distribution was also produced following the same method. But since the width and length of these nanoplatelets differs, two separate plots were made for both. Note that only a Gaussian distribution was fit through the results for the nanoplatelet width, because only 37 nanoplatelets were considered to be aligned in length with the cross-section of the TEM picture whereas it was easier to analyze the width of the nanoplatelets. Nevertheless, the nanoplatelets were 8.7 ± 1.4 nm in width and 20.7 ± 2.7 nm in length.

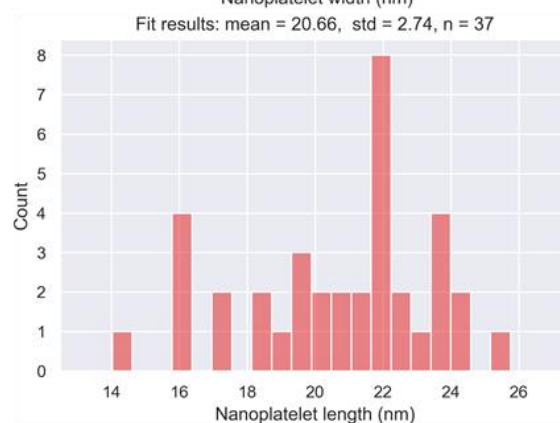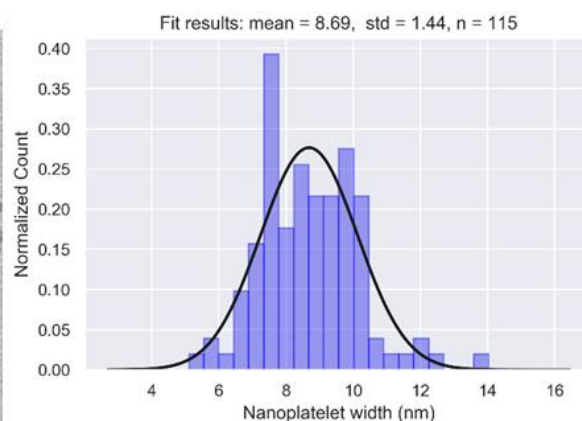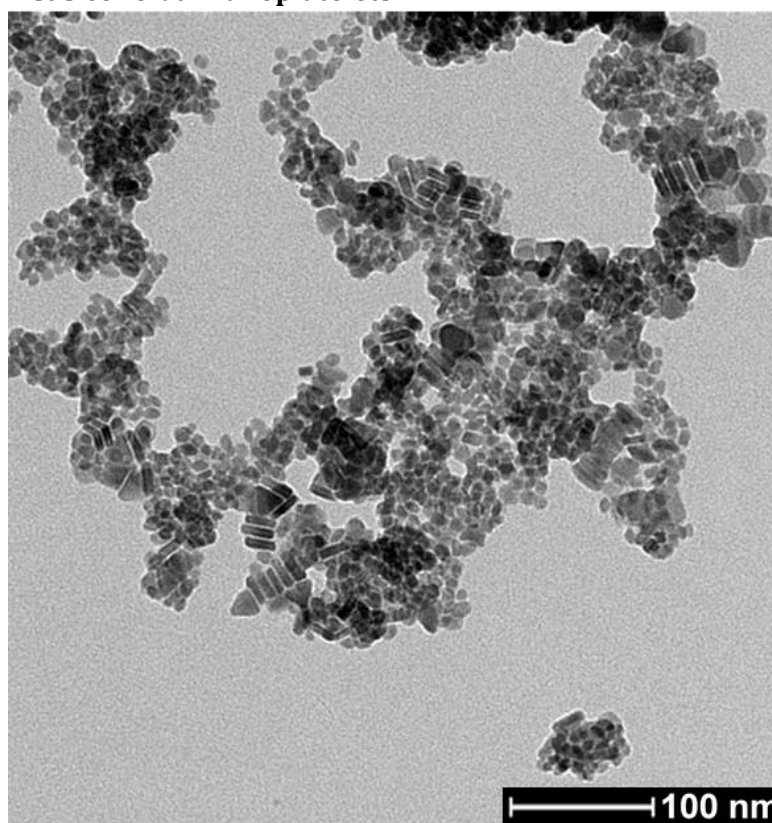# Cu$_2$S colloidal nanoparticles
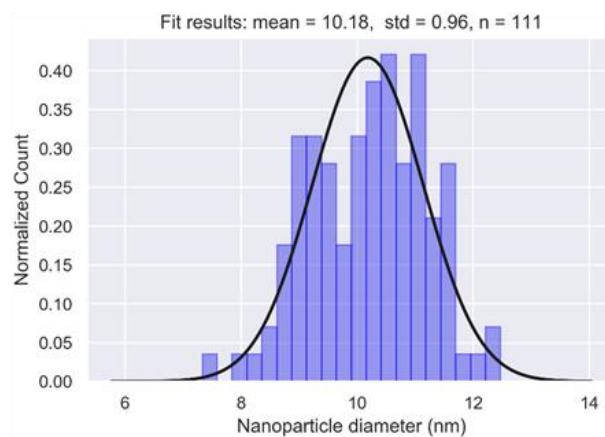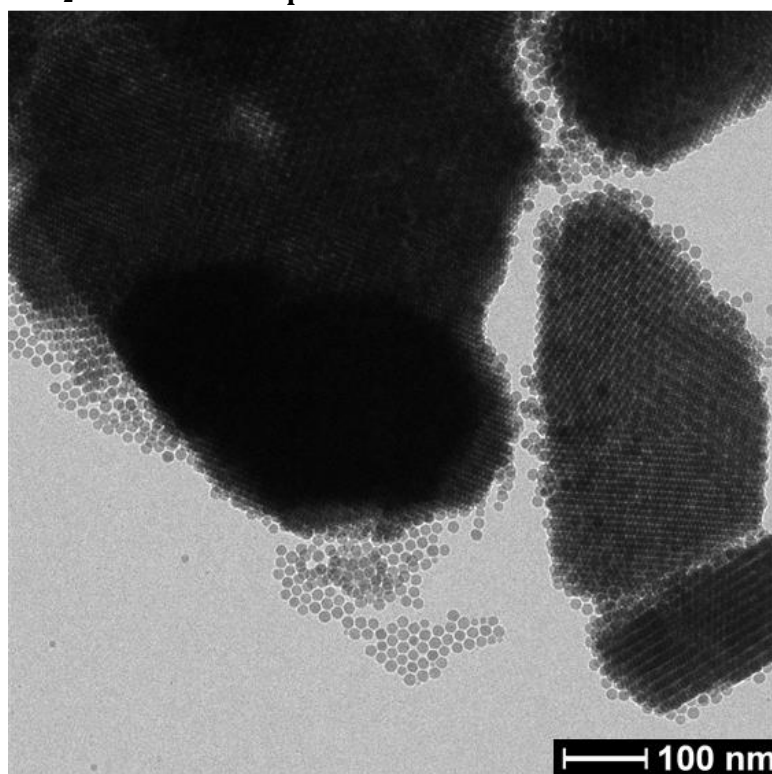
CuS colloidal nanoplatelets

Figure 11: TEM pictures of colloidal Cu$_2$S spherical nanoparticles and CuS nanoplatelets with their particle size distribution obtained from similar TEM pictures. The nanoparticles show a relatively homogeneous particle size dispersion.

TEM analysis was also conducted for the samples produced with incipient wetness impregnation. First of all, Cu_2O/GNP nanoparticles, shown in Figure 12, demonstrated a relatively heterogeneous size dispersion as compared to the colloidal samples with a mean size of 7.6 ± 2.8 nm (with a population of 244 measurements). The nanoparticles also do not exhibit a uniform shape.

Figure 13 then shows the $Cu_{2-x}S$/GNP nanoparticles after sulfidation of Cu_2O/GNP. The Cu_2S/GNP nanoparticles have a spherical shape reminiscent of the Cu_2S colloidal nanoparticles. However, the nanoparticles have a slightly larger size (14.5 ± 2.5 nm) and the particle size distribution is more heterogeneous. Presumably, these nanoparticles do not have the DDT ligands and are supported on GNP. Perhaps thermogravimetric analysis (TGA) could solidify this assumption. Although the high boiling point of DDT may present a problem with respect to combustion of the GNP support itself.

CuS/GNP TEM revealed nanoplatelets similar to the colloidal CuS nanoplatelets. However, these nanoplatelets showed a more heterogeneous size distribution. And analysis of this particles size distribution was further complicated by the geometry of the nanoparticles. Therefore, no fits were produced of the particle size distribution and only a small number of nanoparticles were measured. However, the length and width of the nanoplatelets was approximately 43.7 ± 8.9 nm and 15.2 ± 8.9 nm respectively. Therefore, these nanoplatelets were roughly two orders larger than the colloidal nanoplatelets.
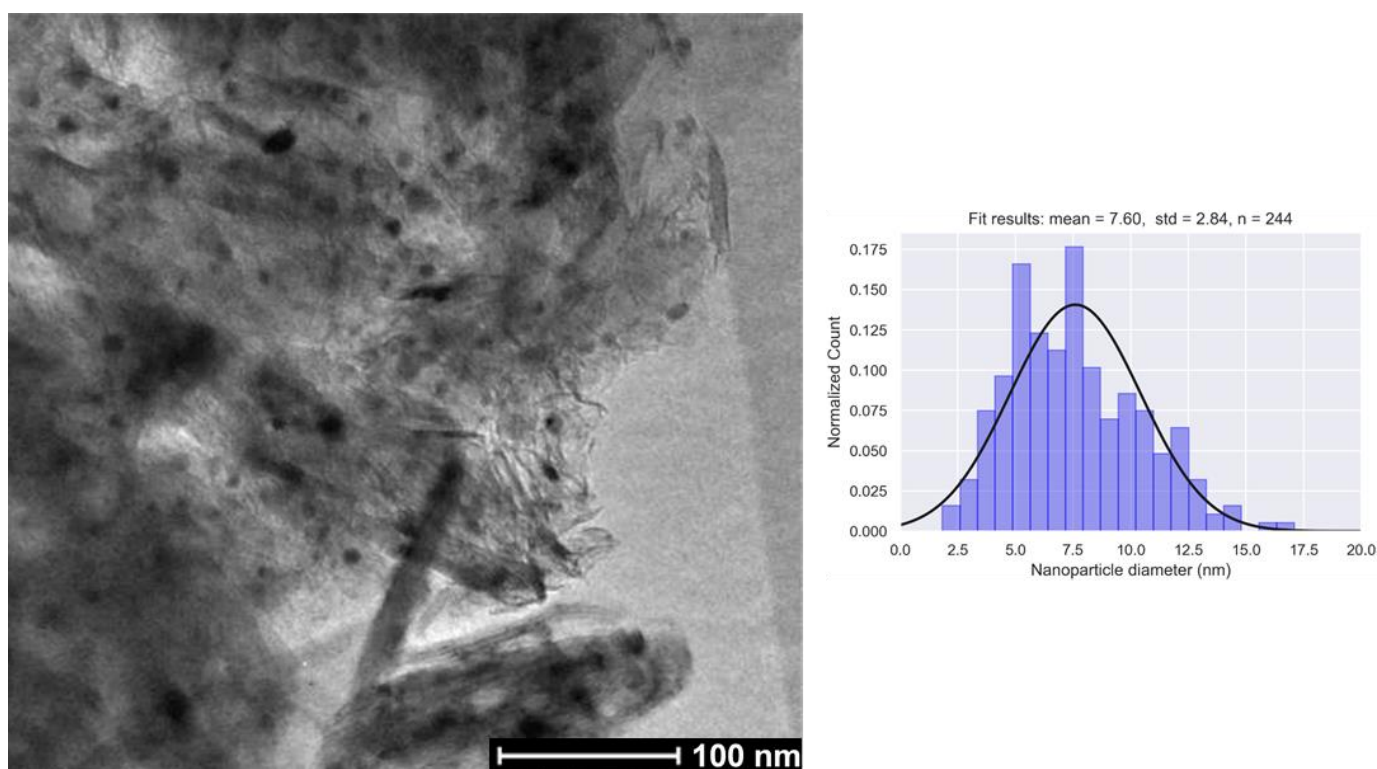
Cu_2O/GNP nanoparticles

Figure 12: TEM picture of Cu_2O/GNP nanoparticles along with their particle distribution obtained from similar pictures.

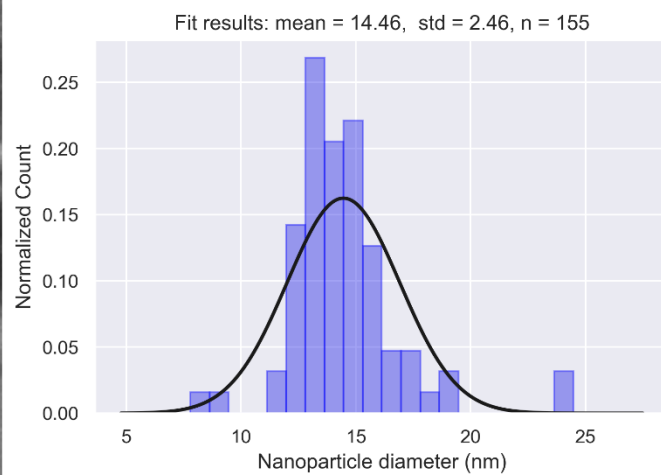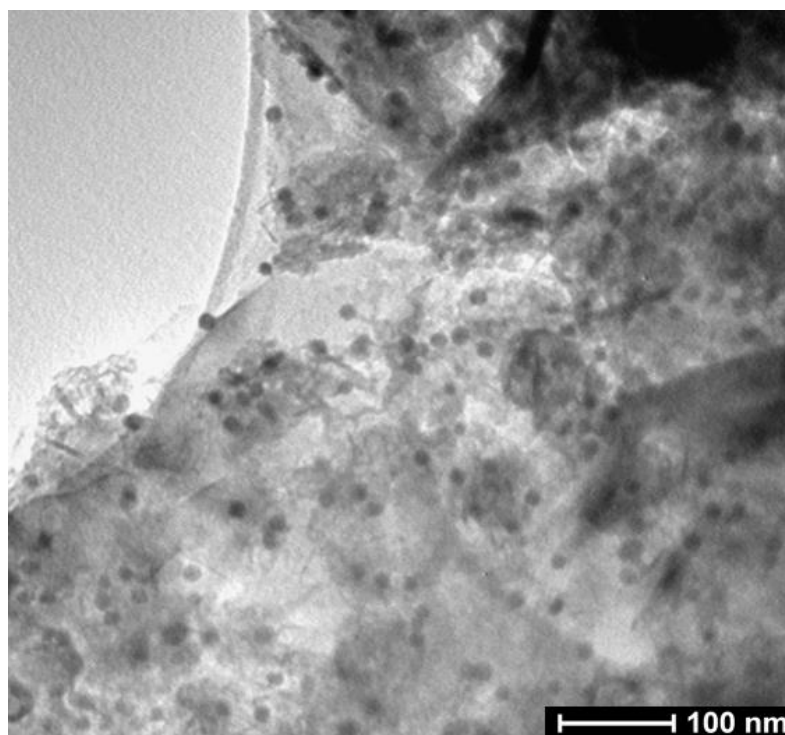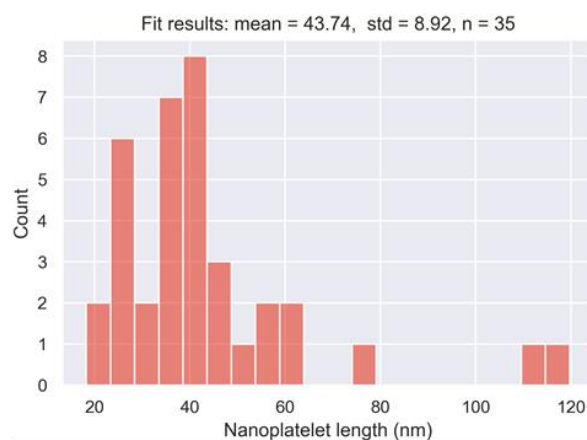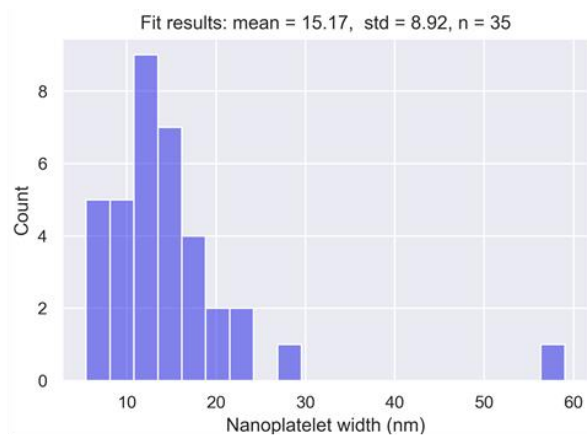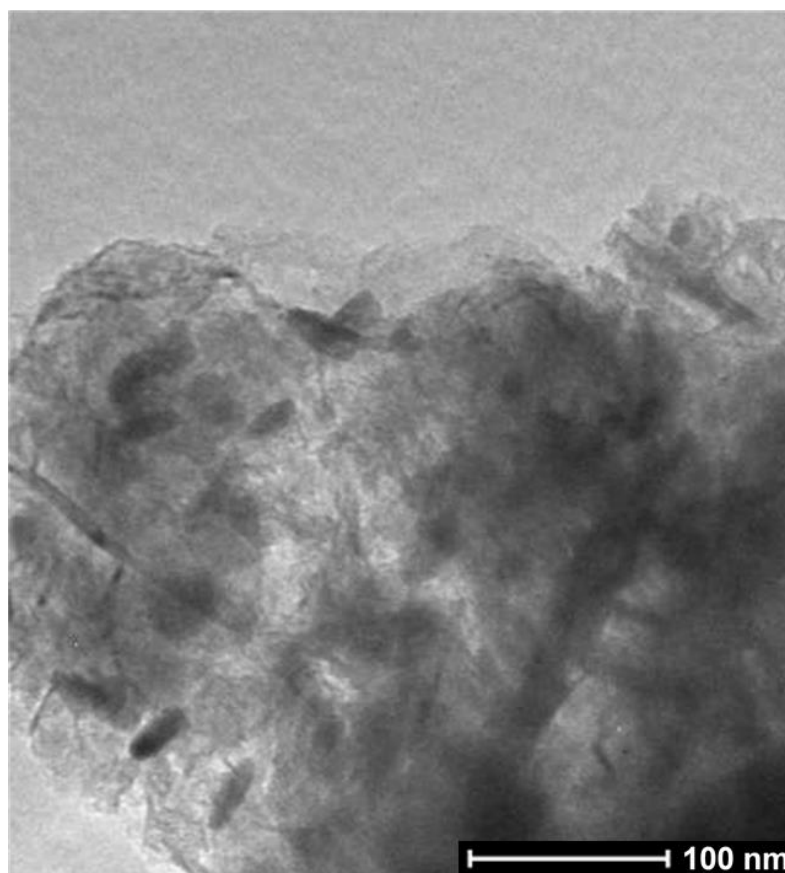## Cu$_2$S/GNP nanoparticles

CuS/GNP nanoplatelets

Figure 13: TEM images of 14.46±2.46 nm Cu$_1$S/GNP nanoparticles (top) and 15.2±8.9 nm wide;43.7±8.9 nm long CuS/GNP nanoplatelets (bottom) with their particle size distributions. These impregnated samples have a more heterogeneous particle size distribution than the colloidal nanoparticles.

4.1.2 X-ray diffraction (XRD) and Electron diffraction (ED)

The crystallinity of impregnated $Cu_{2-x}S$/GNP nanoparticles was analyzed using XRD. The diffractograms are shown in Figure 14 below. A not shown diffractogram of blank GNP powder showed peaks at 31° and between 49° and 53° angle 2θ. Therefore, these peaks were assigned to GNP.

For Cu_2O, the peaks at 42° and 64° angle 2θ match with the (200) and (220) reflections respectively as reported in literature.[39,40] Therefore it was concluded only monophasic Cu_2O was present. The CuS diffractogram matches the with the characteristic (102), (103), (100) indices peaks at 34.1°, 37.0° and 56.2° angle 2θ respectively also reported in literature.[41,42] Finally, the XRD diffractogram for Cu_2S seems most in line with the hexagonal β-chalcocite reference as presented by Sadanaga, M. et al (1965).[43]

Considering these observations, the sulfidation steps from both $Cu_2O \rightarrow CuS$ and $Cu_2O \rightarrow Cu_2S$ proved to be successful for the impregnated samples; producing monophasic Cu_2O, CuS and Cu_2S nanoparticles.
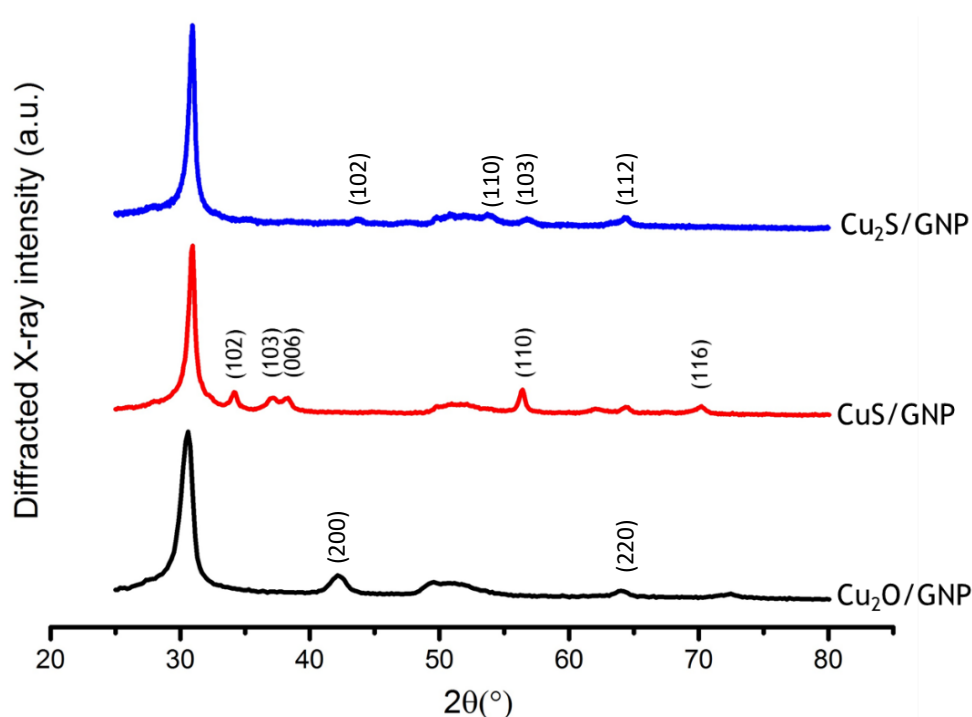

Figure 14: X-ray diffractogram of $Cu_{2-x}S$/GNP catalyst powder with its parent Cu_2O/GNP sample. Monophasic phases were observed. The peaks at 31° and 50° originate from the GNP support.

Unfortunately, XRD could not be employed to determine the crystal structure of colloidal $Cu_{2-x}S$ nanoparticles. Therefore, electron diffraction analysis was performed to establish the crystal structure of the colloidal $Cu_{2-x}S$ nanoparticles. But since the data acquisition and interpretation was not unambiguous, no further ED analysis was conducted. The data is nonetheless included in appendix 9.4.

4.2 Electrode supported Cu$_{2-x}$S characterization

After synthesis, the Cu$_{2-x}$S nanoparticles were deposited on carbon paper by either spray pyrolysis or spray drop casting. This resulted in the electrodes to test CO$_2$RR. While spray drop casting was easier to deposit the Cu$_{2-x}$S nanoparticles, spray pyrolysis offered batch production of electrodes. In turn, the reproducibility of electrode fabrication increased and the homogeneity of catalyst deposition on the electrode increased. This could be observed by naked eye as shown in Figure 15. Although the homogeneity of catalyst deposition could be improved for spray drop casting using multiple spraying steps, this complicated the determination of catalyst loading on the electrode.
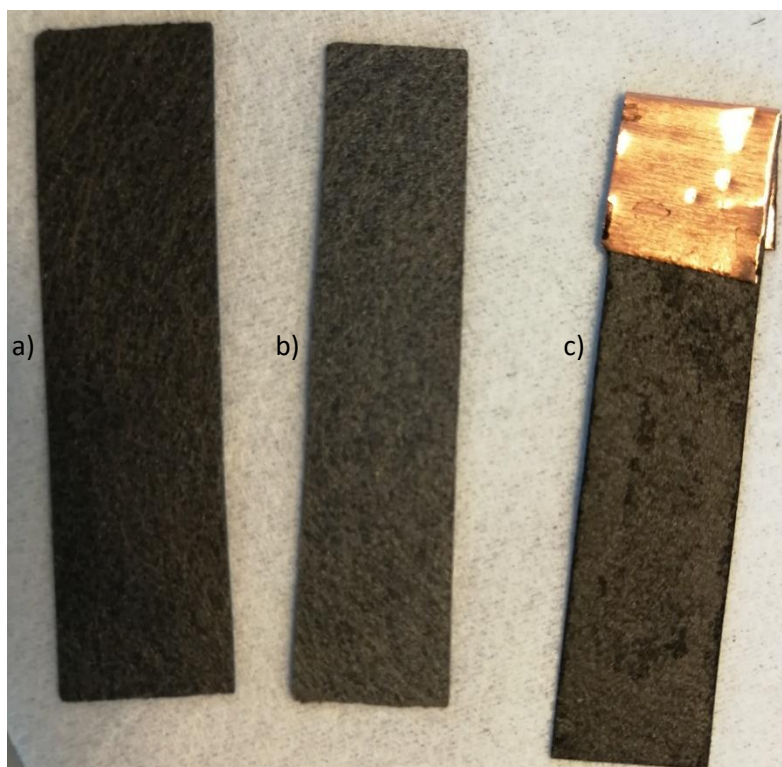

Figure 15: Picture of carbon paper electrodes with a) after spray pyrolysis with Cu$_{2-x}$S/GNP nanoparticle ink, b) a blank electrode, c) after spray drop casting with Cu$_{2-x}$S/GNP nanoparticle ink. The spray pyrolyzed sample shows homogeneous deposition of the catalyst on the electrode.

For spray drop casting the amount of ink sprayed over each electrode determined was used directly to determine the loading. For spray pyrolysis the total amount of catalyst was sprayed over an approximated 254.4 cm^2 circular area. Dividing the catalyst sprayed by this total surface area yielded the catalyst loading/cm^2.

4.2.1 Scanning electron microscopy

Scanning electron microscopy was employed to analyze the deposited Cu_2S colloidal nanoparticles using spray pyrolysis. Due to time constraints no SEM information was gathered for the other $Cu_{2-x}S(/GNP)$ samples.

In Figure 16, colloidal Cu_2S nanoparticles on a carbon paper electrode at 500x magnification are shown. The grey fibers are part of the carbon paper and the white material is the deposited Cu_2S nanoparticle agglomerates. When zooming in to 60,000x it is possible to spot individual Cu_2S nanoparticles as well. This testifies of the homogeneity of depositions that spray pyrolysis can obtain. Since half of a colloidal Cu_2S synthesis batch was used for this experiment, perhaps an even better dispersion can be achieved if a lower Cu_2S nanoparticle concentration is used.

Increasing the magnification to almost 249,000x it is possible to see the Cu_2S nanoparticles aggregate in a close packed array. Furthermore, charging of Cu_2S nanoparticles at the top of the superstructures is apparent because this area appears brighter. The charging is ascribed to imperfect conducting regions.[44] Possibly, this indicates that part of these Cu_2S nanoparticles is not
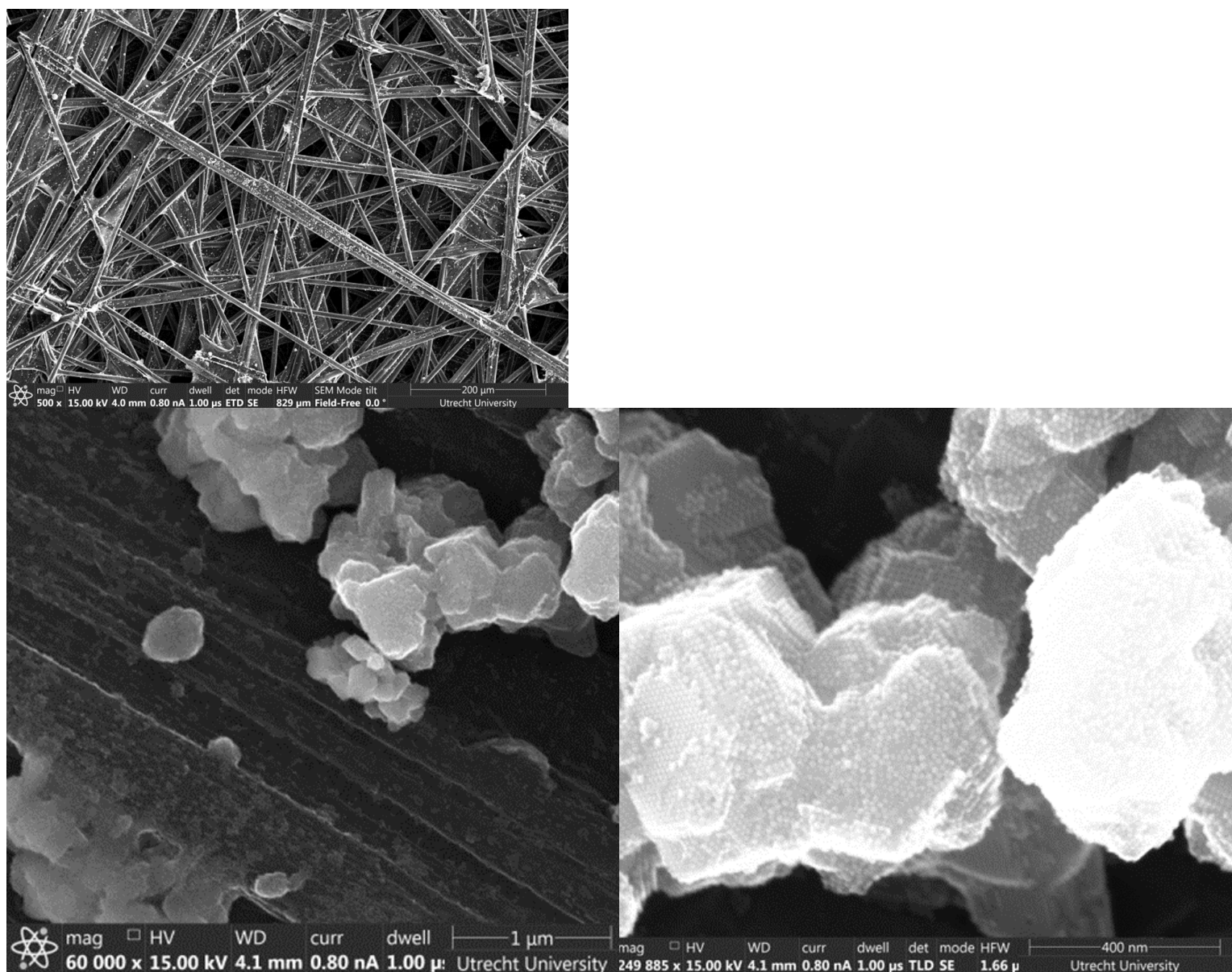

Figure 16: SEM pictures of Cu_2S colloidal nanoparticles on a carbon paper electrode. The fibers are the carbon paper and the white material are the deposited Cu_2S nanoparticles.

active for CO$_2$RR. This is not surprising considering the apolar DDT ligands that stabilize the Cu$_2$S nanoparticles. Nonetheless, this may change when a certain potential is applied.

In Figure 17, the same sample is shown but now after CO$_2$RR at -1.2V vs RHE. It seems that some crystals have grown over the super structures. These crystals probably formed during the drying of the electrodes. When looking closely at the picture with 250,000x magnification the super structures are still visible. But no individual Cu$_2$S nanoparticles can be seen from the 60,000x magnification. Perhaps the individual nanoparticles have been overgrown by the salt deposits.
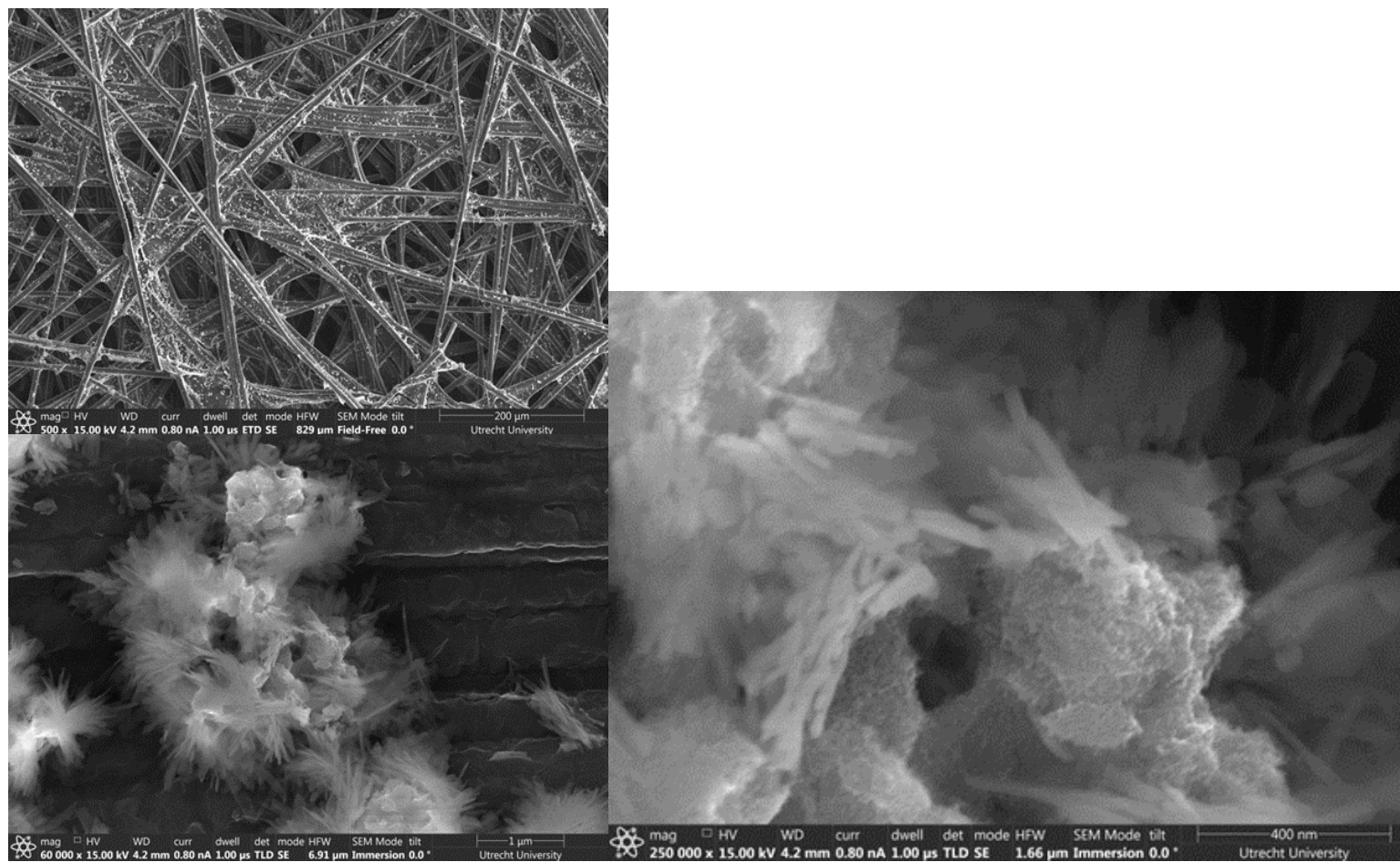

Figure 17: SEM pictures of Cu$_2$S colloidal nanoparticles after -1.2V vs RHE. The white crystal deposits (plate-like structure) are salts originating from the electrolyte upon drying of the electrode. The Cu$_{2-x}$S superstructure as shown before CO$_2$RR is still visible.

It was also possible to first support the Cu$_2$S nanoparticles on Vulcan carbon 72x in the sonication deposition as reported in section 3.1.3. The corresponding SEM image is shown in Figure 18. In
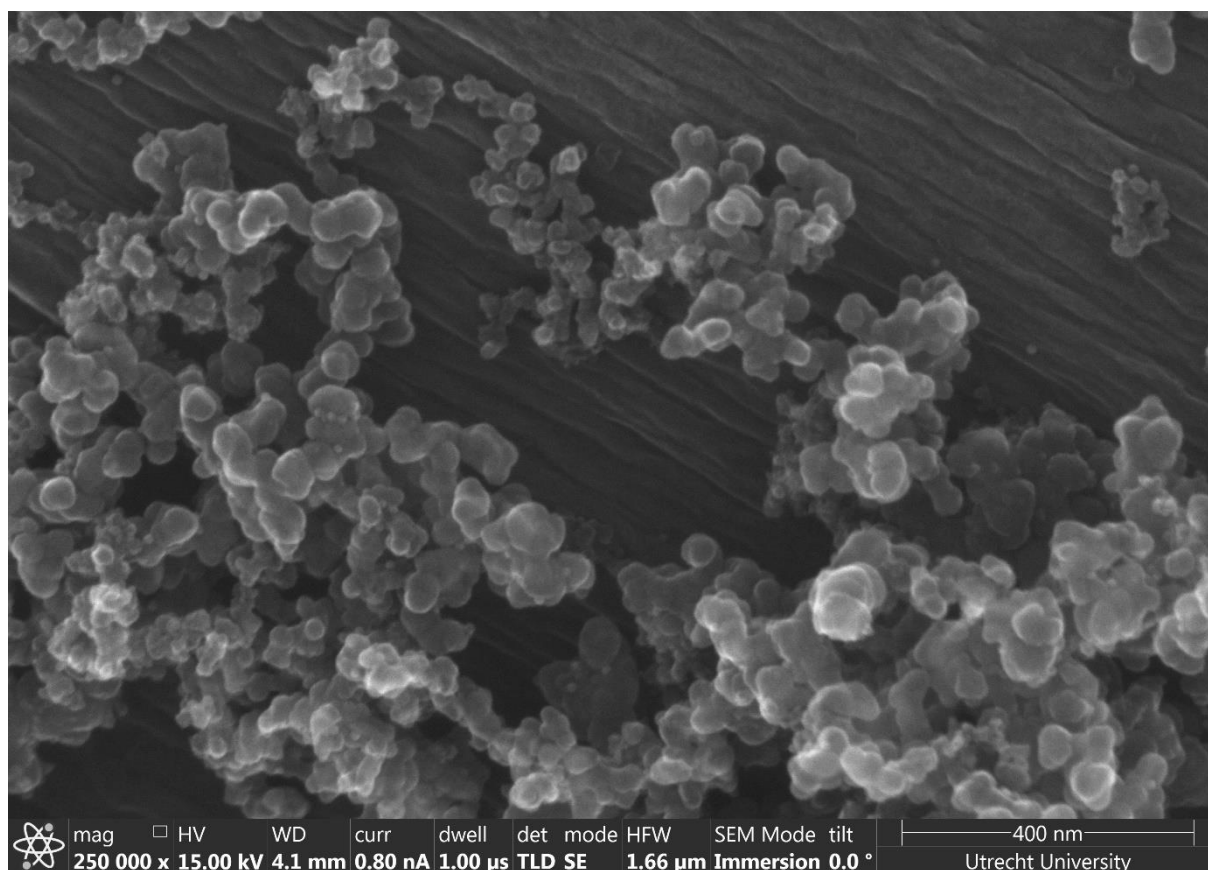

Figure 18: SEM image of Cu$_2$S colloidal nanoparticles/VC72x on a carbon paper electrode after spray pyrolysis.

the image individual Cu$_{2-x}$S nanoparticles as well supported on the Vulcan carbon can be seen. However, since it was found that the carbon support was highly active for HER. It was decided to stick with the colloidal Cu$_2$S nanoparticles directly supported on the electrode.

4.2.2 Energy Dispersive X-rays (EDX)

Energy Dispersive X-rays (EDX) analysis was performed in conjunction with the SEM experiments of section 4.2.1 to map the element distribution of the Cu_2S coll samples before (KH8A) and after CO_2RR at -1.2V vs RHE in 0.1M $KHCO_3$ (KH8B). EDX images from KH8A clearly show the white deposited material consist of Cu and S as shown in Figure 19. Oxygen and carbon EDX have not been shown for clarity. The absence of other compounds demonstrated that no significant cross-contamination occurred with spray pyrolysis electrode fabrication.
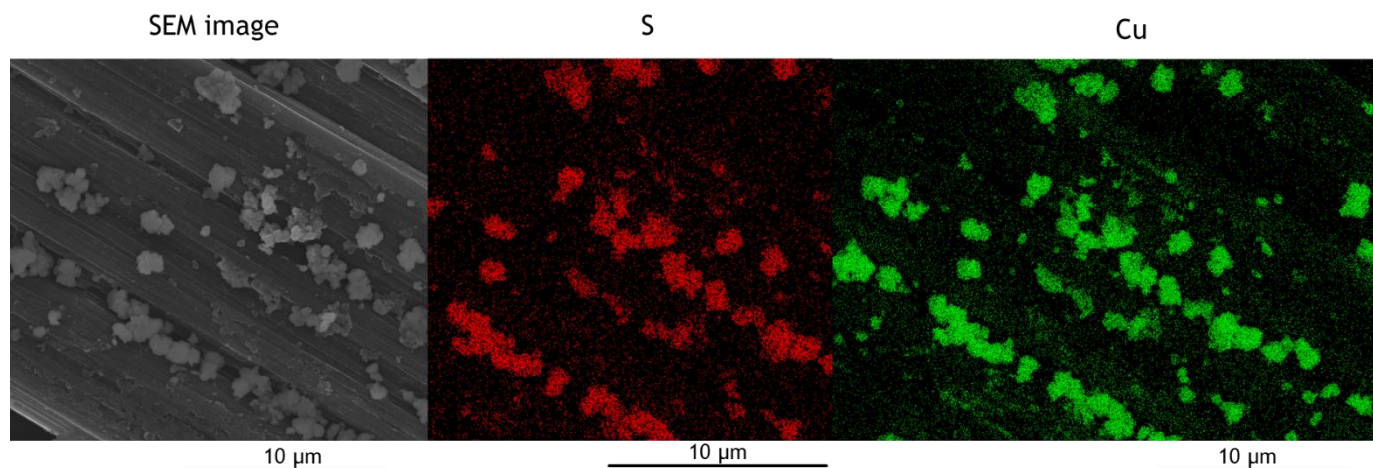

Figure 19: SEM/EDX images of Cu_2S colloidal nanoparticles on carbon paper. The Sulphur as marked in Red and the Green Cu demonstrate the white deposits to be the Cu_2S colloidal nanoparticles.

In Figure 20, the EDX elemental distribution maps for KH8B are shown. There was a clear presence of Potassium indicating the presence of K salts on the electrode. Interestingly no $KHCO_3$ is formed as the potassium deposits are present where the crystals seem especially C deficient.
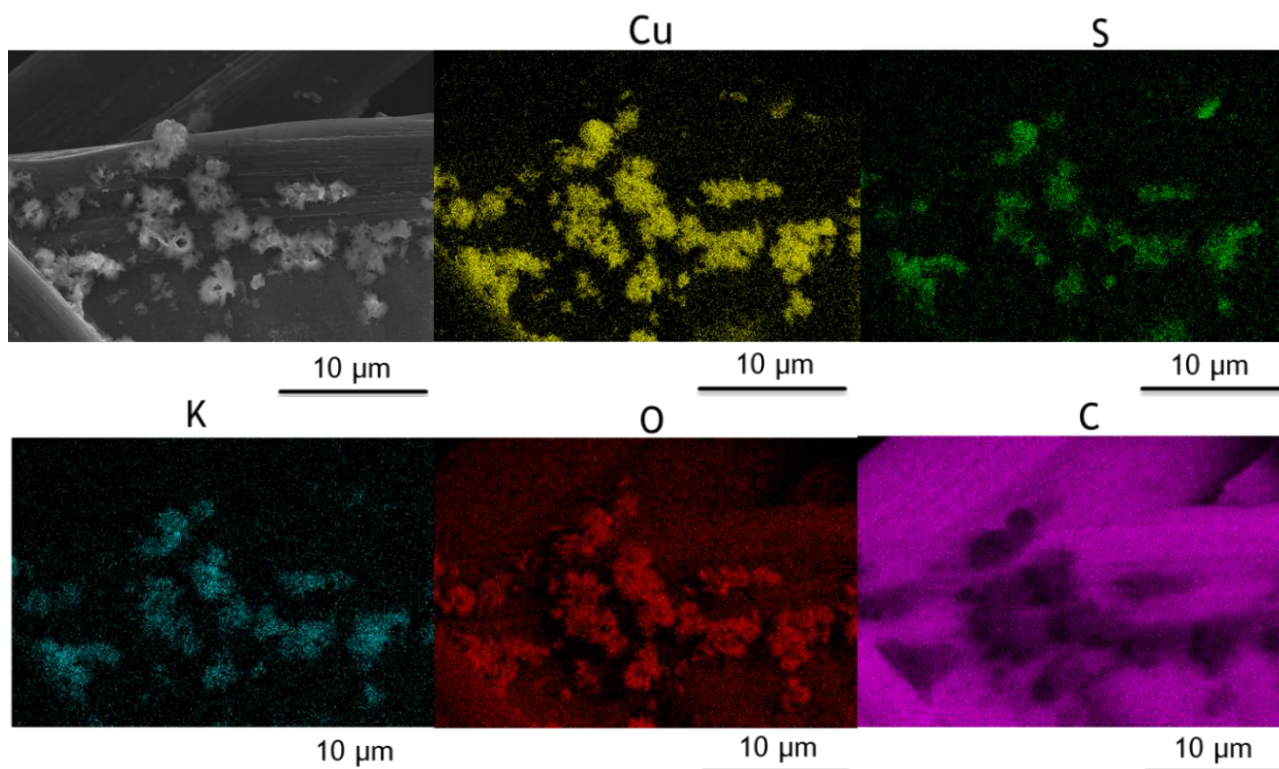

Figure 20: SEM/EDX images of Cu_2S colloidal nanoparticles on Carbon paper after -1.2V vs RHE chronoamperometry.

This could suggest the salt deposits to be KOH which is not far-fetched regarding the high local pH at the surface of the electrode. Furthermore, the intensity of the S in KH8B seems to be lower than KH8A. This may indicate that Cu_2S reduces party to metallic Cu when -1.2V vs RHE is applied. The presence of Cu_xO, that may form upon removal of the potential after the experiment, it is not likely. However, this can't be excluded.

In Figure 21, the EDX spectra are shown for KH8A and KH8B. In these spectra the differences in counts for certain elements give a more evident quantitative representation of elemental distribution changes. Also, higher O presence and occurrence of K are observable as was seen from the EDX elemental distribution images. The decrease of S indicates possible reduction of Cu_2S at -1.2V vs RHE.
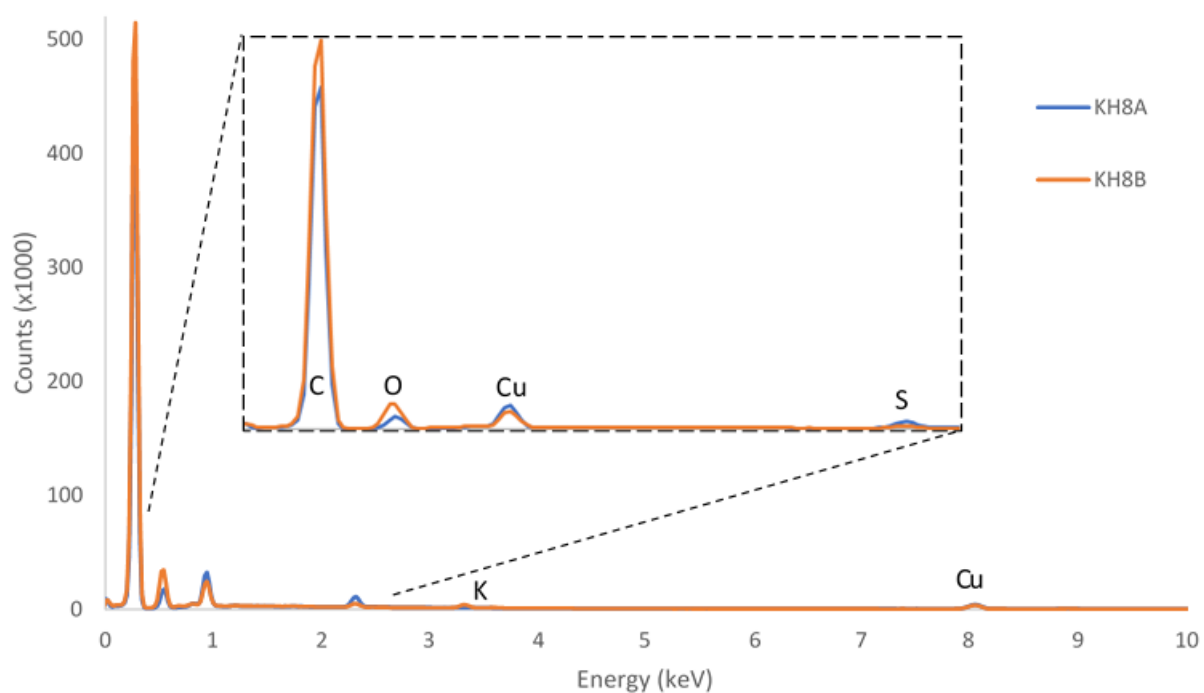

Figure 21: EDX spectra for Cu_2S colloidal nanoparticles; KH8A (after spray pyrolysis) and KH8B (after -1.2V vs RHE CO_2).

4.2.2   Electrochemical surface area (ECSA)

Normalizing current to the electrochemical surface area is important to be able to compare catalysts with literature. For nanoparticles this is even more significant because the ECSA is orders of magnitude larger than the geometric surface area.

Early attempts to determine the ECSA were made using Underpotential Deposition of Lead based on the article of Baturina et al.[45] However, the deposition and stripping of Cu_2S loaded electrodes was deemed too unreliable for determining the surface area of each catalyst. The reasons for this were that possible oxidation/reduction of $Cu_{2-x}S$ may cause for overestimation of the ECSA. Alternatively, the ligands surrounding the colloidal $Cu_{2-x}S$ nanoparticles may decrease the accuracy of the measurement. The results are nonetheless shown in appendix 9.1.

Another method that is commonly applied to determine the ECSA is the use of double layer capacitance as further explained in appendix 9.1. To determine this double layer capacitance, cyclic voltammograms were recorded in the non-faradaic region of $Cu_{2-x}S$/GNP catalysts, Cu foil and GNP to probe the double layer capacitance of the electrodes. The potential window for these scans was chosen based on earlier CV where no exponential current increase was observed associated with product formation. The results for these experiments are shown in Figure 22. For the $Cu_{2-x}S$/GNP and GNP samples a clear trend could be derived using the double layer capacitance equation presented in section 2.3. Yet the flat Cu foil sample had such low capacitance that the current could no longer be accurately measured. Hence, the corrosion current I_a and I_c where first extrapolated by plotting a trendline through the linear part of the cyclic voltammograms. Subsequently, these corrosion potentials were used to find the double layer capacitance. For all samples excluding the Cu foil, outliers were omitted from the capacitance determination. In Table 1, the capacitance results are shown relating to the catalyst loadings for Figure 22. GNP shows a significantly higher capacitance than the $Cu_{2-x}S$/GNP samples. This was attributed to the large surface area of the carbon supports. Regarding that the $Cu_{2-x}S$/GNP samples also have a large amount of GNP, one would expect the capacitance to be higher. Perhaps the reason for this could be that the $Cu_{2-x}S$ nanoparticles inhibit the underlying GNP surface from contributing to the overall capacitance of the sample. Whilst this is an interesting observation, no clear ECSA can be determined.
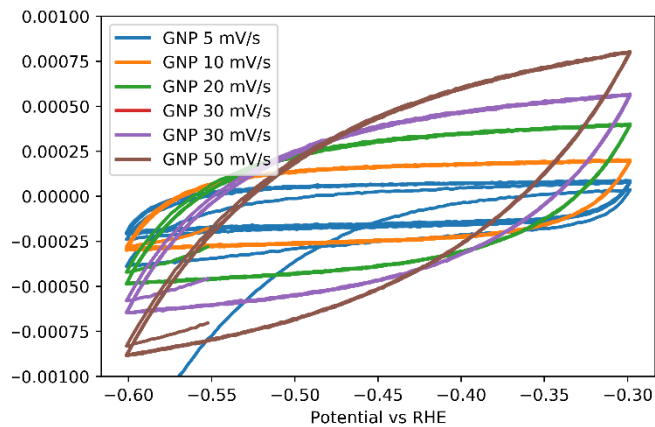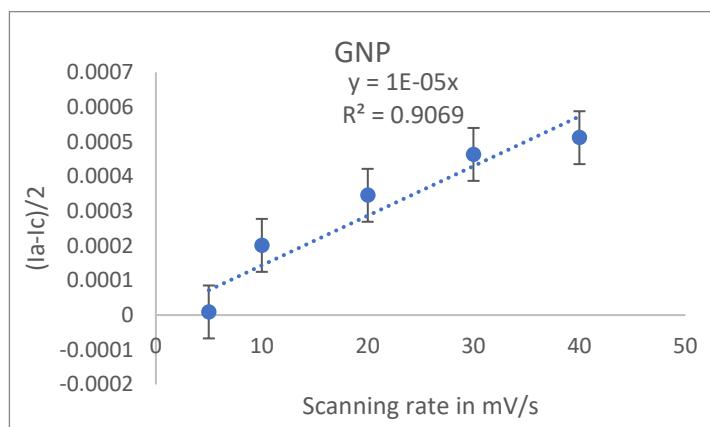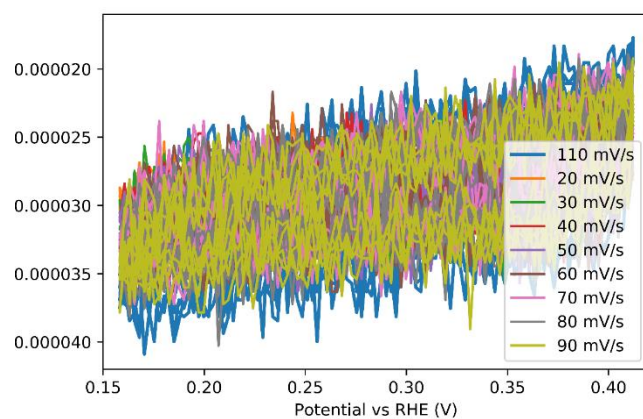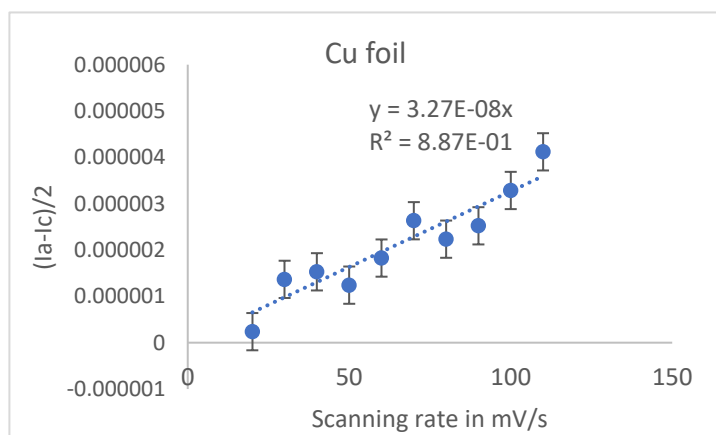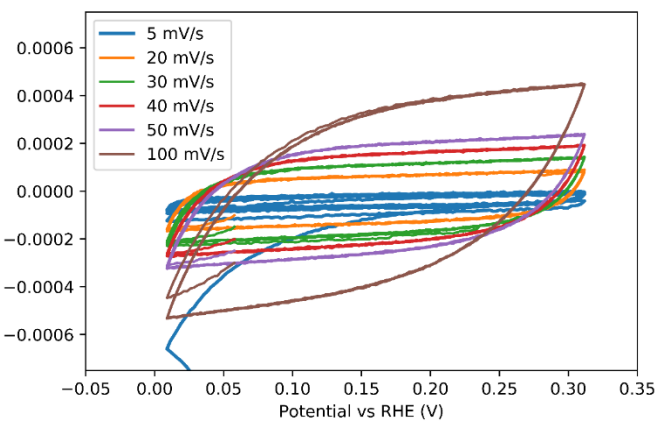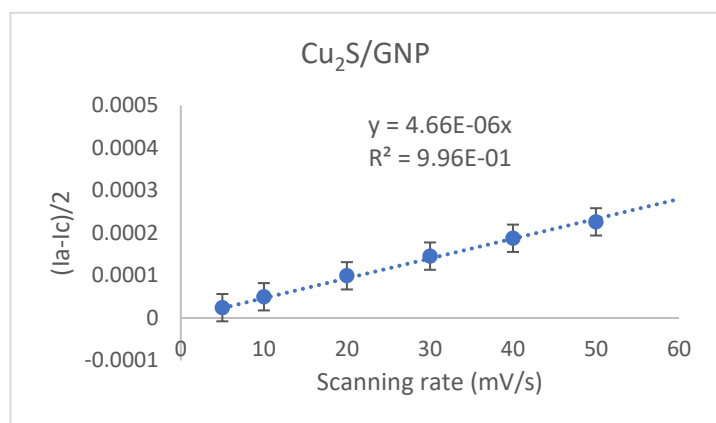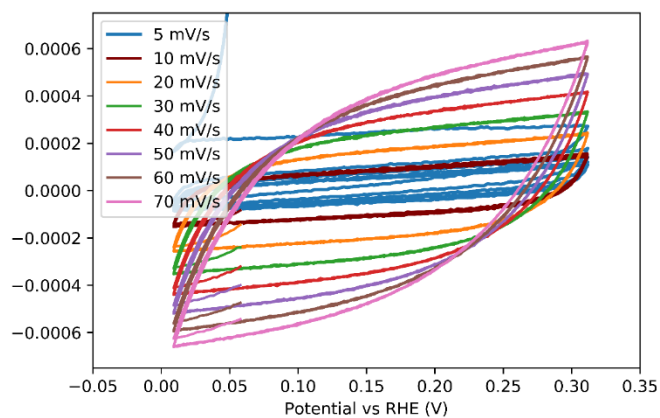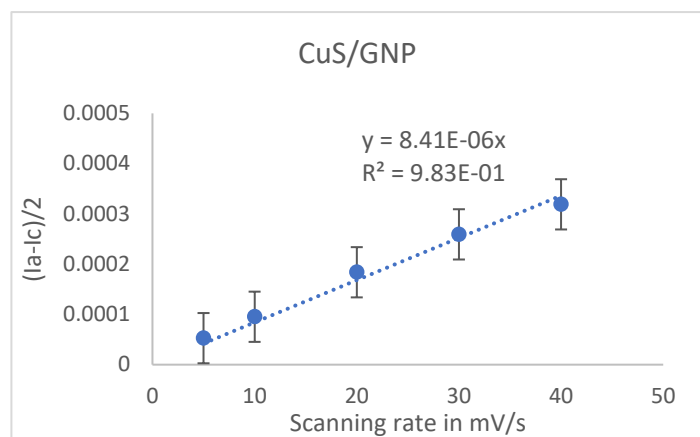
Figure 22: Overview double layer capacitance experiments. On the left the calibration plots are shown and, on the right, the corresponding cyclic voltammograms.

Catalyst	Cu foil	Cu_2S/GNP	CuS/GNP	GNP
Capacitance (μF)	32.7	4660	8410	14300
R_f	1	121	213	355
$Cu_{2-x}S$/GNP loading (mg/cm^2)	-	0.47	0.63	0.63
Cu loading (mg/cm^2)	-	0.09	0.13	-

Table 1: Double layer capacitance results for $Cu_{2-x}S$ catalysts as opposed to Cu foil and GNP references. No ECSA could be attributed due to the higher capacitance of GNP.

Thus, it was decided to use the shape and size from the TEM results with the calculated loadings to determine the electrochemical surface area for a given sample. These ECSA values are shown in Table 2 for a typical experiment involving spray drop casting. For simplicity the ECSA of Cu_2S was approximated assuming the volume and surface of a sphere. For the same reason the ECSA of CuS was approximated assuming a cylindrical volume and surface.

Catalyst	Cu_2S/GNP	CuS/GNP
Loading catalyst on electrode (mg/cm^2)	0.63	0.63
Electrode size (cm^2)	4.9	4.9
Cu loading (mg/cm^2)	0.13	0.13
Average size (nm)	14.5	Width: 13.9, Length: 39.5
Density $Cu_{2-x}S$ (g/cm^3)	5.65[46]	4.68[47]
Molar mass (g/mol)	159.16[46]	95.61[47]
Maximum ECSA (cm^2)	Spherical particles: 1132	Nanoplatelets particles: 878

Table 2: ECSA values for Cu_2S/GNP and CuS/GNP loaded electrodes assuming spray drop casting as electrode fabrication method assuming spherical Cu_2S and cylindrical CuS nanoparticles.

However, due to the complex nature of determining the ECSA for all samples, it was chosen to simply normalize the current to the geometric surface area of the electrode. The catalyst loading can however be referred to when comparing the catalysts to other $Cu_{2-x}S$ materials in literature.

4.3 Electrocatalytic reduction of CO_2

4.3.1 Electrocatalytic reduction of CO_2 with $Cu_{2-x}S$ catalysts

CuS/GNP showed distinct and reproducible reduction peaks during cyclic voltammetry from 0V to -1.6V vs RHE, see Figure 23**Error! Reference source not found.**. This could indicate the reduction of the CuS phase to either another $Cu_{2-x}S$ phase or Cu(s). For Cu_2S/GNP no such feature was observed. However, the linear relationship between current and potential indicated the occurrence of electrolyte resistance (Ohm's law). In view of this, the electrolyte $KHCO_3$ concentration was only 0.1M and there was no other salt added to facilitate electrical conductance.
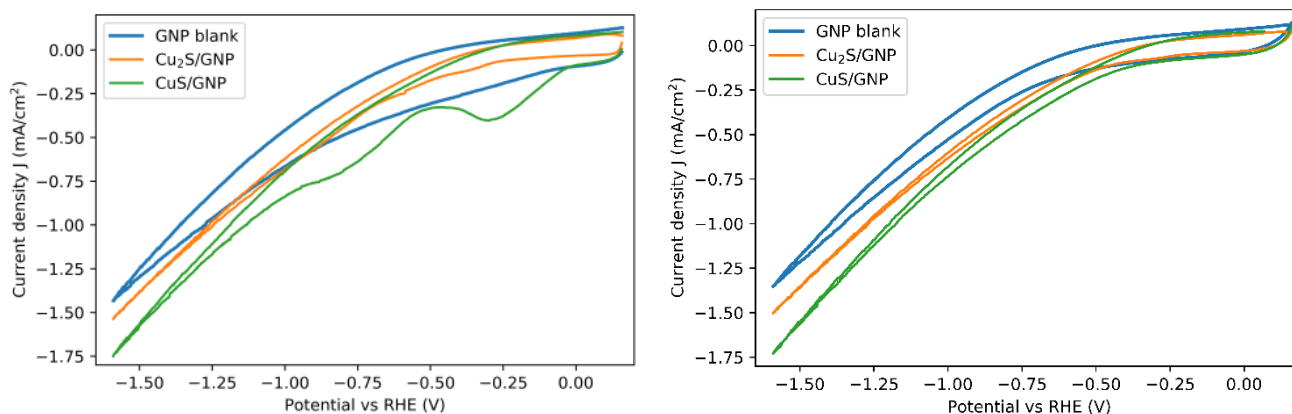

Figure 23: First (left) and second (right) cycles of CuS/GNP and Cu_2S/GNP catalysts in 0.1M $KHCO_3$ with cyclic voltammetry. Clearly reduction onset potentials are visible for CuS/GNP. The linear relationship between the current and potential indicates electrolyte resistance dominating the current flow through the cell.

Thus, internal resistance may have dominated the current flow in the cell. Therefore, it was decided to increase the concentration of the $KHCO_3$ electrolyte to 0.5M and focus more on the potential range of the first reduction peak. This yielded the results shown in Figure 24**Error! Reference source not found.**. The experiments were somewhat inaccurate due to the fluctuations in the voltammograms. But a clear reduction peak for CuS/GNP is observed in the first cycle. For Cu_2S/GNP this is not visible in the same extent. However, in both cases $H_2S(g)$ could be smelled when opening the reactor after the experiment. The following reaction pathways are thus speculated:

A) $CuS + H^+ \rightarrow Cu_{2-x}S + HS^-$ after which $HS^- + H^+ \rightarrow H_2S(g)$

B) $Cu_2S + H^+ \rightarrow Cu(s) + HS^-$ after which $HS^- + H^+ \rightarrow H_2S(g)$
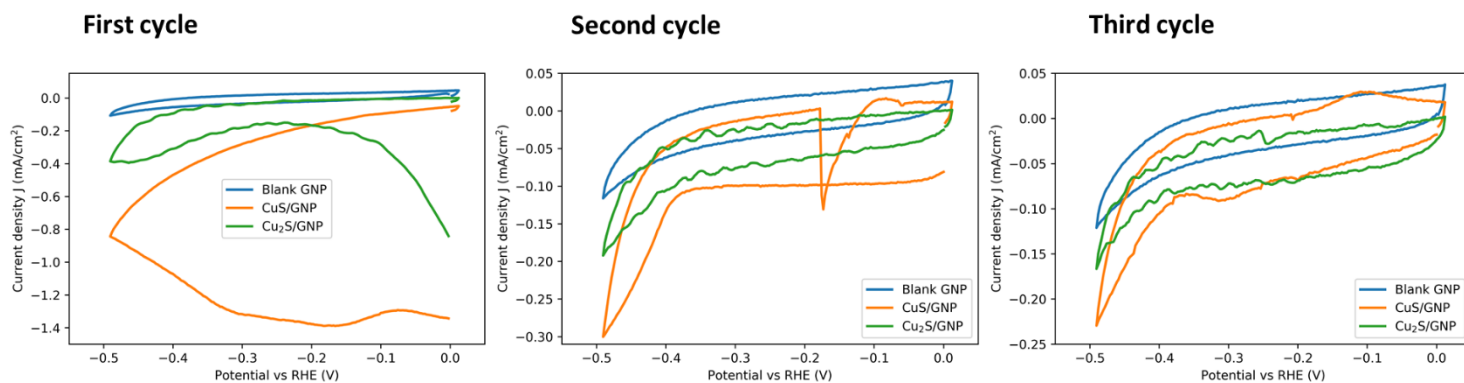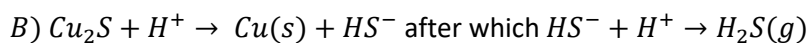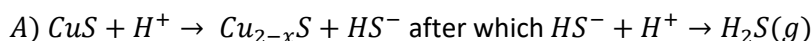

Figure 24: Cyclic voltammogram cycles for CuS/GNP, Cu_2S/GNP and a GNP-HT blank.

Therefore, further cyclic voltammetry focused on understanding the influence of the feed gas. For this purpose, CuS/GNP and Cu$_2$S/GNP loaded electrodes were probed by cyclic voltammetry in a smaller potential window (from 0 to -0.5V vs RHE) in 0.25M K$_2$HPO$_3$/KH$_2$PO$_3$ – see Figure 25. The feeding gas was then either 10 mL/min CO$_2$(g) or Ar(g). Typical for these experiments was a large reduction peak would be observed in the first scan (starting from 0V to -0.6V and back). This peak matches the first reduction peak in **Error! Reference source not found.** where it also disappears after the first cycle. Given with the fact that again H$_2$S(g) could be smelled after the experiments when opening the reactor, this indicates that sulfide is leaching from the electrode.
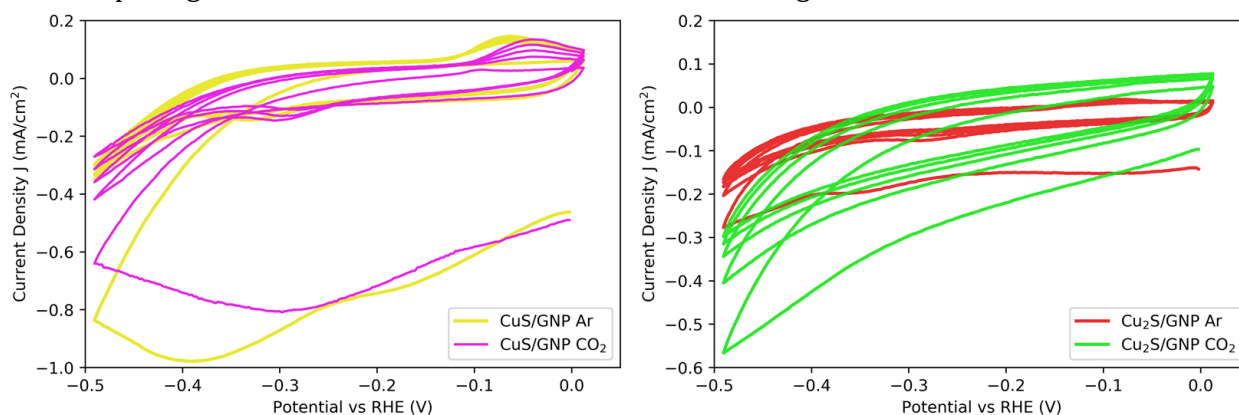

Figure 25: Cyclic voltammograms of CuS/GNP and Cu$_2$S/GNP catalysts with either Ar or CO$_2$ feed in 0.25M K$_2$HPO$_3$/KH$_2$PO$_3$ electrolyte. Using CO$_2$ as feed shows more distinct decrease in current density with each cycle which is probably related to depletion of reducible species near the electrode surface. For both Cu$_2$S/GNP and CuS/GNP the Cu loading was 0.13 mg/cm^2.

Furthermore, no distinct differences for between CO$_2$ and Ar feeding gas were identified apart from the decreasing current density with each cycle for the CO$_2$ experiment and the different position of the oxidation and reduction peak at -0.05V and -0.3V vs RHE respectively. The decreasing current density could be attributed to competition of dissolved CO$_2$ species and H$_2$O to adsorb to the surface, thus decreasing activity of HER. The aforementioned potential differences in oxidation and reduction peaks are probably caused by the acidification of dissolving CO$_2$ which does not happen with Ar. However, the question then remains what the origin of this oxidation and reduction peak are.
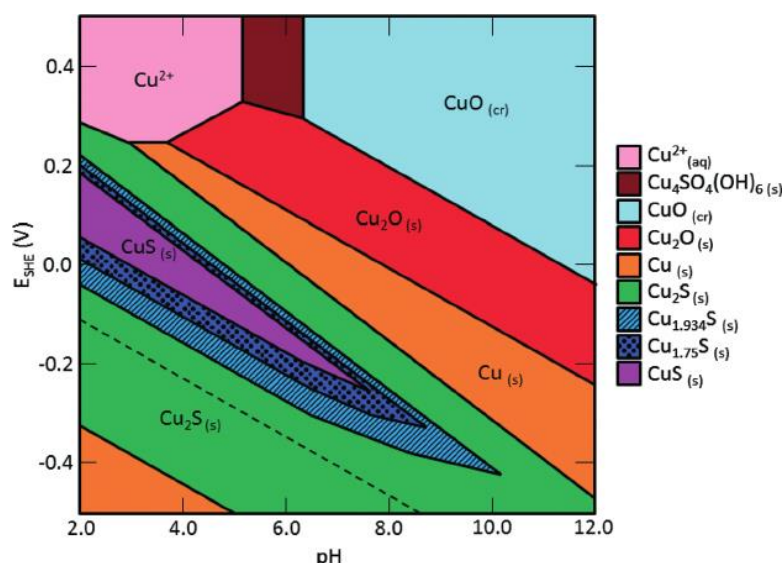

Figure 26: Pourbaix diagram of stable Cu species as function of pH and potential vs the standard Hydrogen electrode.

In Figure 26 a Pourbaix diagram is shown of theoretical stable species of $Cu_{2-x}S$, Cu_xO and $Cu(s)$. It should be taken into account that the pH of the electrolyte is unambiguous. With the bulk pH of the solution being 7, The local pH of the electrode in the double layer may well be 8.[31] Also the E_{SHE} differs from the experimental E_{RHE} peaks. Nonetheless, it may be that reduction of CuS → Cu_2S occurs in the first half of the first cycle. Consequently, the oxidation peak at -0.05V vs RHE could constitute the oxidation of Cu_2S → $Cu_{1.94}S$. The reduction peak at -0.3V vs RHE, of equal magnitude, could then be the reverse process. The reason for this is that the djurleite ($Cu_{1.94}S$) phase is rather stable and the oxidation peak is only 0.226 C. [source]

Regarding the possibility that the oxidation peak could originate from the formation of a Cu_xO species, also cyclic voltammetry was performed with a metallic Cu foil sample as shown in Figure 27. Expected Cu species are presented in the regions expected based on Giri S.D. and Sarkar A.[48] The oxidation of Cu from this experiment seems to take place only at increasingly positive potentials than used in cyclic voltammetry with the $Cu_{2-x}S$ samples. Therefore, the oxidation peaks were concluded to originate from a $Cu_{2-x}S$ species.
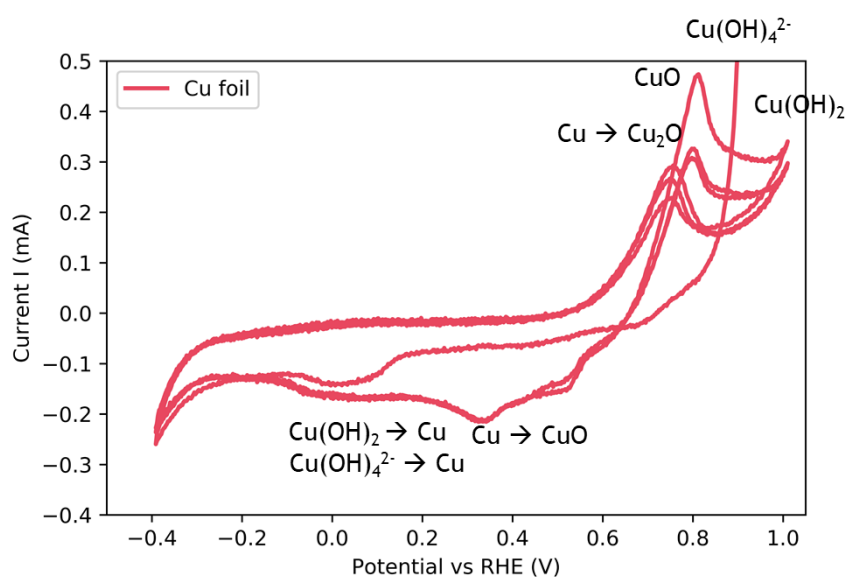

Figure 27: Cyclic voltammetry of Cu(s) foil in 0.1M KHCO$_3$ with expected potentials Cu species present.

Cyclic voltammetry was also performed with the colloidal $Cu_{2-x}S$ nanoparticles in 0.5M KHCO$_3$. In Figure 28, CV scans show remarkable differences. Although a similar weight loading of Cu was aimed for in the preparation of the electrodes, the experiments are not quantitative. The reason for this is that deposition of 0.05 mL catalyst ink is not reliable with spray drop casting and the loading for the Cu_2S Na$_2$S ligand exchanged nanoparticles was approximately 10x smaller (see appendix 9.3). But, the distinct oxidation and reduction features do allow for a simple qualitative comparison. It is clear-cut from the figure that all colloidal samples have a higher current than the blank carbon paper electrode. This also indicates that the ligands surrounding the $Cu_{2-x}S$ nanoparticles are not completely isolating them. But the evident decrease of current with each cycle for Cu_2S DDT and CuS indicates that reduction of $Cu_{2-x}S$ phases or their ligands may take place. The Cu_2S Na$_2$S sample, where the ligands have been exchanged for S^{2-} exhibited an increasing current with each cycle. This was also observed when using a broader potential range as shown in Figure 29. Therefore, it would be interesting to further see the selectivity for these $Cu_{2-x}S$ Na$_2$S ligand exchanged nanoparticles. This sample does however originate from JW4 see appendix 9.3. So, the Cu_2S nanoparticles have been prepared through a different synthesis route and were 8.1 nm in diameter instead of the 10.2 nm Cu_2S coll DDT nanoparticles. Which could explain its higher activity due to its larger surface area.
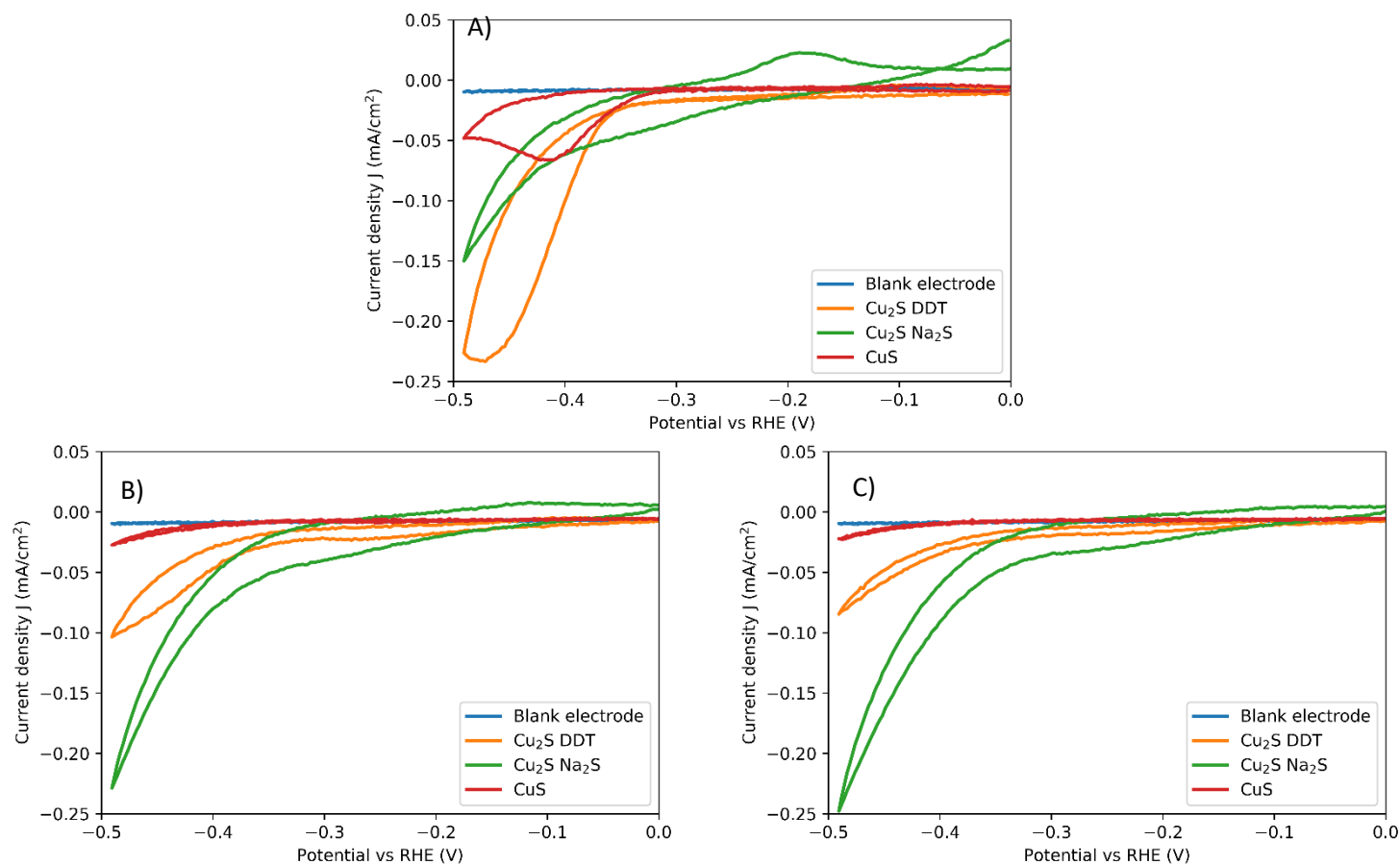
Figure 29: A) first cycle B) second cycle C) third cycle of Cu$_{2-x}$S colloidal nanoparticles in 0.5M KHCO$_3$. The larger current for each cycle as opposed to the blank electrode indicates higher electrochemical activity than the blank.
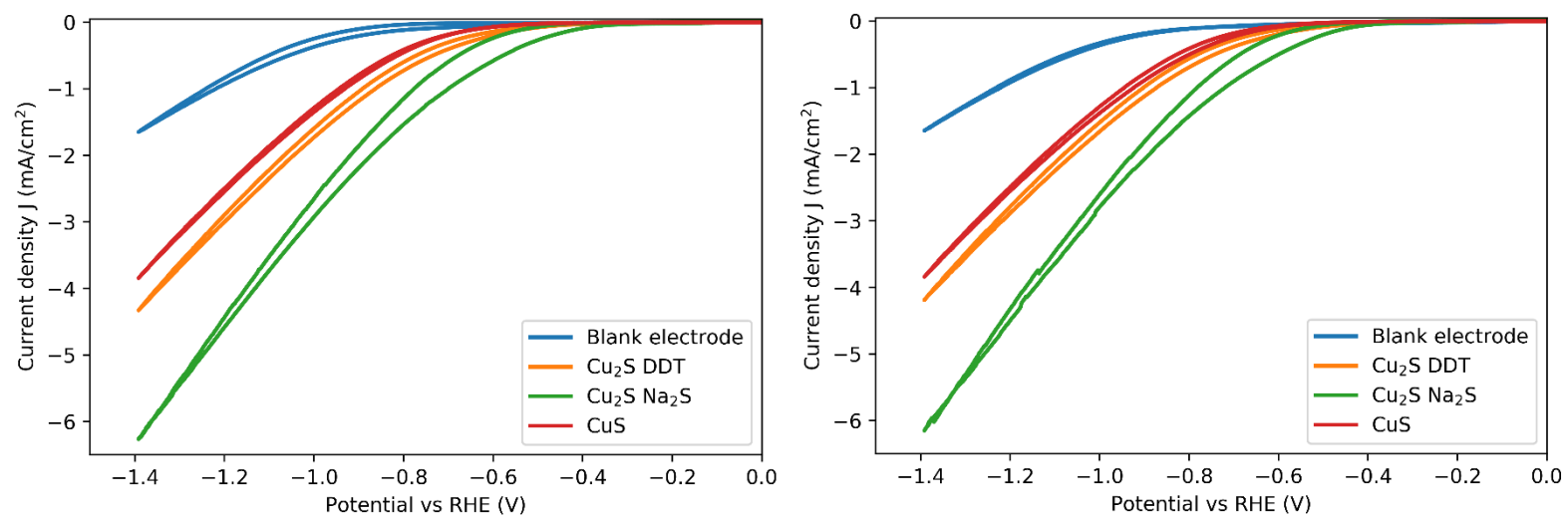

Figure 28: A) First cycle and B) second cycle of Cu$_{2-x}$S colloidal samples in 0.5M KHCO$_3$.

4.3.2 In-situ X-ray absorption Spectroscopy experiments (XAFS)

After an electrochemistry experiment, the removal of the applied reducing current/potential potentially induces re-oxidation of catalyst species. Therefore, ex-situ experiments before and after catalysis to characterize the active catalyst phase could result in the wrong conclusions about what happens under reaction conditions. Hence, the use of in-situ analysis techniques is preferred to pre and post ex-situ analysis. To study the active $Cu_{2-x}S$ catalyst phase, in-situ XAFS experiments were performed. For these experiments Cu_2S/GNP, CuS/GNP and Cu_2S colloidal nanoparticles were deposited on gas diffusion electrodes. Of these samples, ex-situ and in-situ samples along with a Cu foil sample were analyzed to gain more understanding of the $Cu/Cu_{2-x}S$ phases present during CO_2RR.

The results for the ex-situ samples as compared to their references in literature are shown in Figure 30a). The ex-situ samples are well in line with literature except for the CuS/GNP ex-situ sample.[49] XRD analysis on the same sample of CuS/GNP after the XAFS experiments revealed still the same CuS phase as measured before. In Figure 30b) XAFS spectra from Prashant K. et al (2013) are shown. The blue line originating from Cu^{2+} matches well with the CuS_ex-situ reference sample. It seems for this reason, that the ex_situ CuS/GNP sample contains Cu^{2+}.

Furthermore, the spectra measured seem somewhat shifted to the left in terms of Energy (eV). Perhaps this could be because the reference spectra were obtained at the Stanford Synchrotron radiation Lightsource (SSRL).
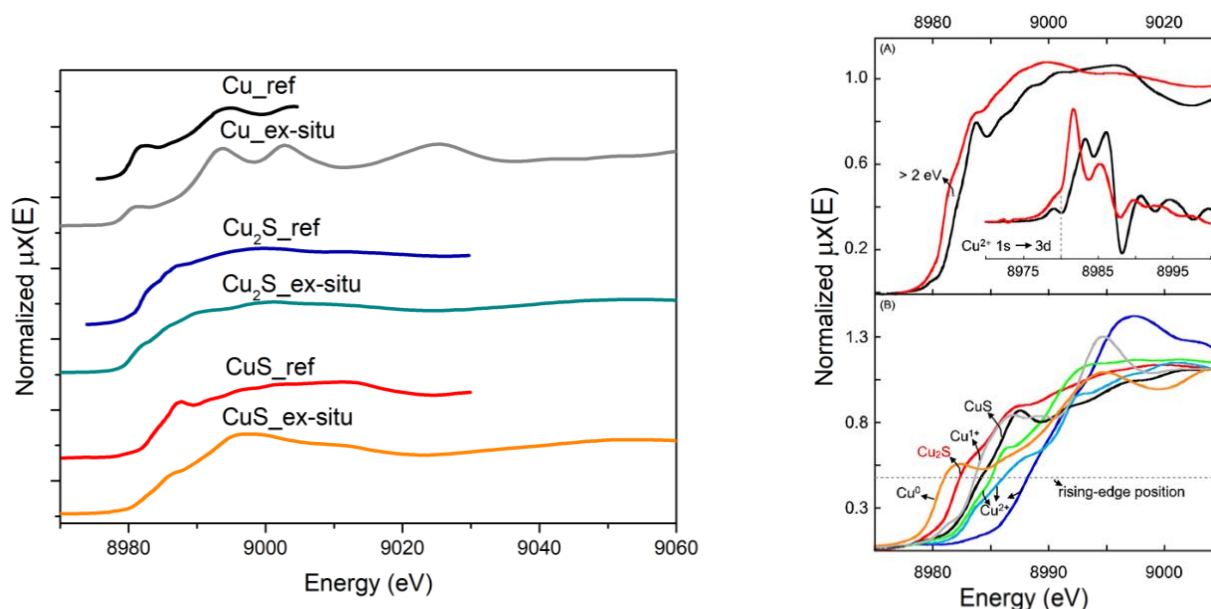

Figure 30:A) Metallic Cu and Cu2-xS/GNP ex-situ XAFS spectra of the Cu K edge as compared to their references in literature. The ex-situ samples resemble the references well apart from CuS_ex-situ. B) Reference spectra for $Cu_{2-x}S$ species as adapted from K. Prashkant et al. (2013)

The ex-situ samples were then used as references for the in-situ XAFS results. The set-up for the in-situ experiments is shown in Figure 31. Unlike previously mentioned electrochemistry experiments, CO_2 saturated electrolyte was pumped through an electrochemical cell. Also, a Sustainion anionic exchange membrane was used instead of the usual nafion proton exchange membrane. The use of different cells and materials for experiments therefore limit the viability of comparisons between the in-situ XAFS results and the electrochemistry results reported in section 4.3.1.
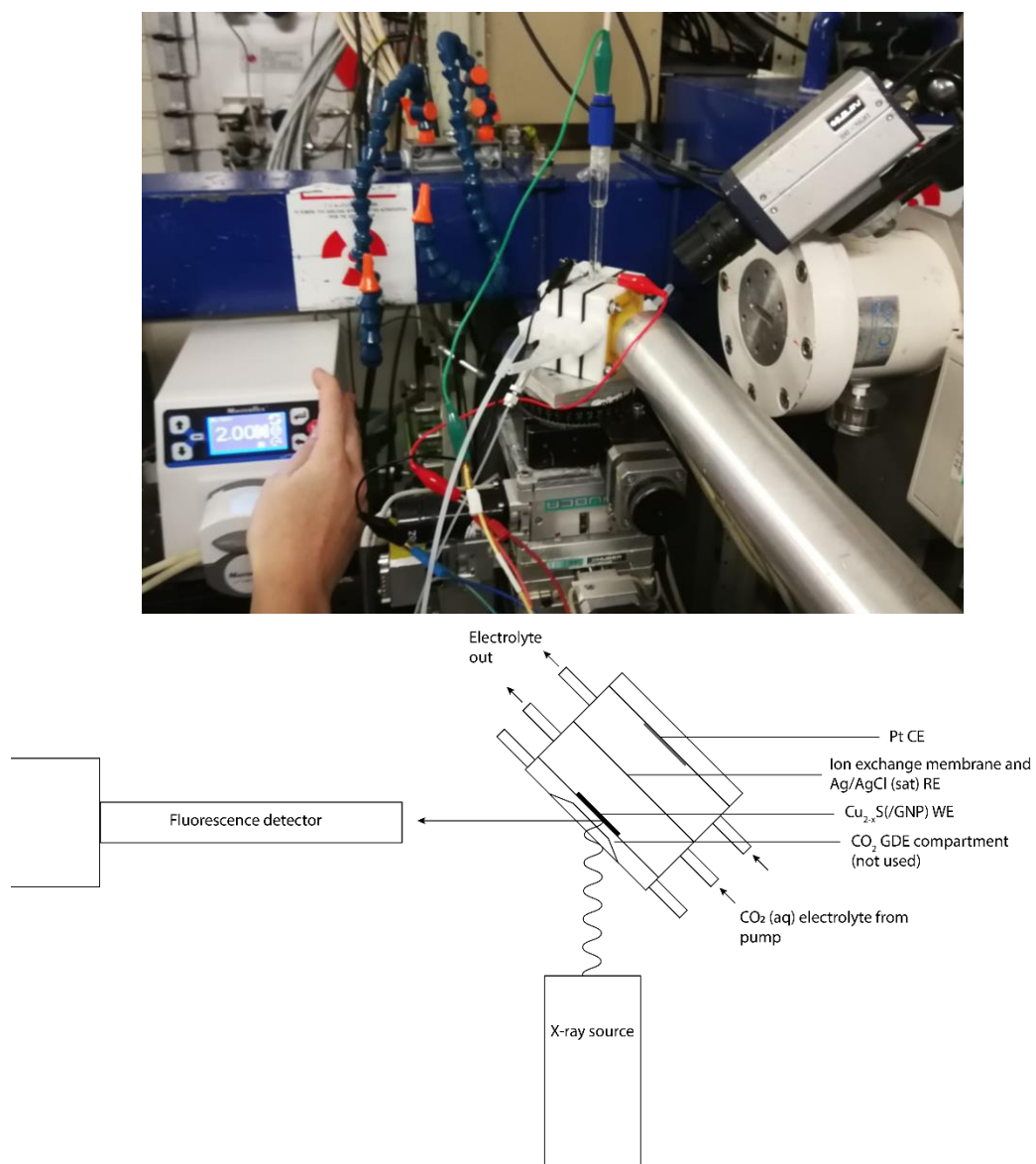
Figure 31: In-situ XAFS set up overview. The sample was placed under a 45° angle with respect to the X-ray source and fluorescence detector to optimize fluorescence yield and signal-noise ratio.

As shown in Figure 32a) the in-situ CuS with no potential applied (NP) sample resembles the CuS ex-situ sample. Hence, these samples must have the same crystal structure. However, CuS seems to reduce to Cu_2S towards -2.2V vs Ag/AgCl (3M) ($\approx$ 1.6V vs RHE) due to a greater resemblance of the edge structure to the Cu_2S ex-situ sample. But when comparing the CuS/GNP -2.2V in-situ sample to the Cu foil reference as shown in Figure 32 b), it seems there is also metallic Cu present. The reason for this is because there is no distinct undulation at 9022 eV in the edge structure as is shown for the Cu_2S and CuS references. But the Cu foil reference has a clear peak at that energy. All things considered it may be that the CuS/GNP sample was not a pure phase due to the resemblance of its ex-situ reference to CuO. Since CuO reduces at lower potentials than a $Cu_{2-x}S$ phase, it is quite likely that a Cu(s) phase is present at such reducing potentials. [50]
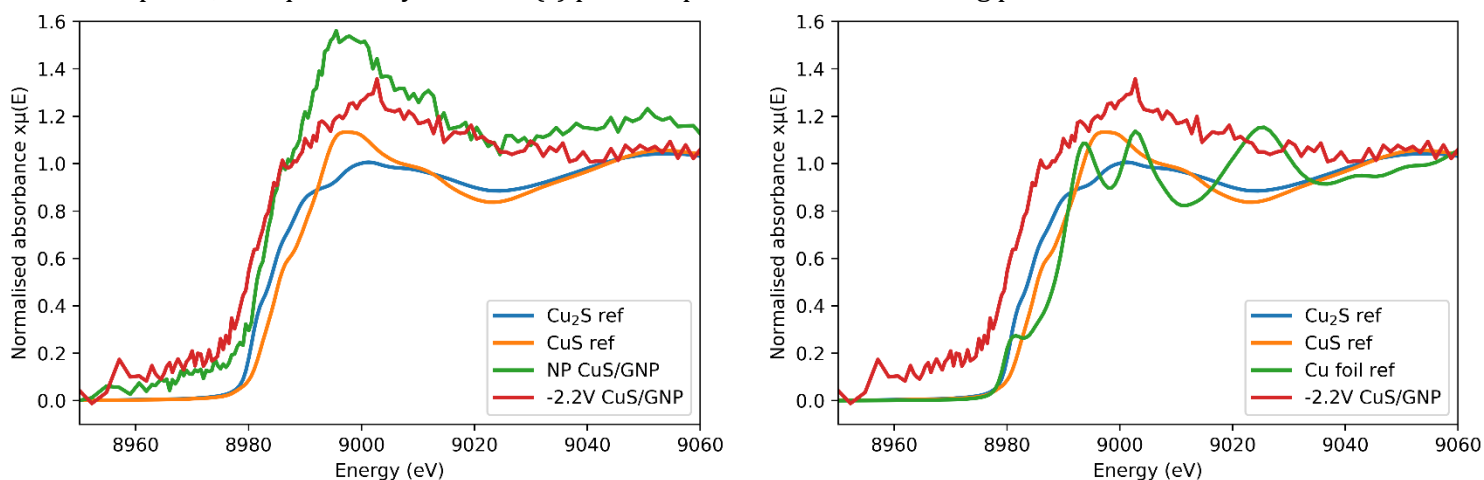

Figure 32: a) In-situ CuS/GNP with no potential (NP) and CuS/GNP with -2.2V XAFS spectra and ex-situ references. b) The same as the first but then with the Cu foil reference. From figure a it seems CuS reduces to Cu_2S, but the dip in intensity at 9022 eV and shift of edge energy indicates the presence of Cu(s).

Earlier research to Cu_2S nanoparticles showed reduction at the surface of Cu_2S to metallic Cu at -1V vs RHE.[20] Considering XAFS is a bulk analysis technique it could be that the CuS reduces to Cu_2S at the surface without an evident Cu_2S edge structure. Because then the signal of the surface $Cu_{2-x}S$ structure would be less than the bulk signal. The same could apply for Cu(s) in this case.
Evaluating the Cu_2S/GNP in-situ sample shown in Figure 33, shows that the crystal structure is Cu_2S when no potential is applied. However, the spectrum at -2.2V vs Ag/AgCl (3M) shows the emergence of a peak at 8981 eV in the pre-edge that is reminiscent of the Cu foil reference pre-edge. Moreover, the rise in absorbance at 9022 eV could also originate from the presence of Cu(s) at the interface where electrochemistry occurs. All in all, the in-situ results of both $Cu_{2-x}S$/GNP samples suggest the presence of a Cu(s) phase and a significant amount of Cu_2S. Thus, only partial reduction of Cu_2S to Cu(s) is apparent. The question then remains whether this could be due to formation of Cu shell – Cu_2S – core nanoparticles or if the a major part of Cu_2S is inactive or unable to contribute for CO_2RR.
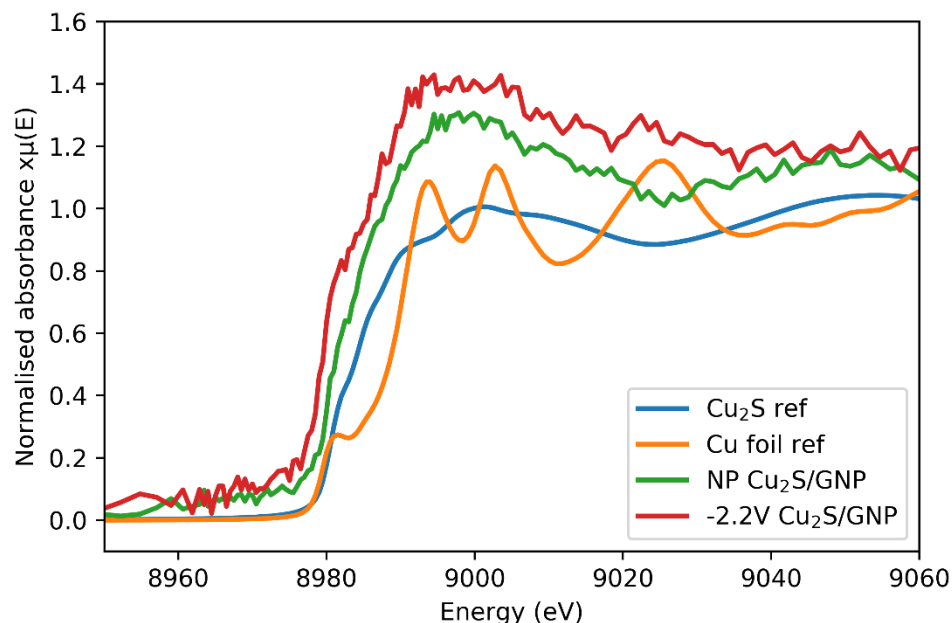
Figure 33: In-situ Cu$_2$S/GNP with no potential (NP) and Cu$_2$S/GNP with -2.2V XAFS spectra with the identified references. The pre-edge structure and higher absorbance at 9022 eV indicates the presence of Cu(s).

On the other hand, the colloidal Cu$_2$S XAFS structure is not as clear cut as the supported Cu$_{2-x}$S samples; there seems to be no shift in the absorption edge and the difference at 9022 eV is rather small from the Cu$_2$S/GNP reference. A possible explanation for this is the presence of the DDT ligands surrounding the colloidal particles. If these ligands shield the Cu$_2$S nanoparticles, this raises the question whether they are inactive for CO$_2$RR as well. But when analyzing the fluorescence signal drop at 9048 eV, it was found that this coincides with a drop in current flow through the cell. This is believed to be the formation of gaseous products that occupy the electrode's surface. When a bubble occupies part of the electrode surface, it renders the covered surface unable for electrochemical activity. When the bubble displaces a certain amount of
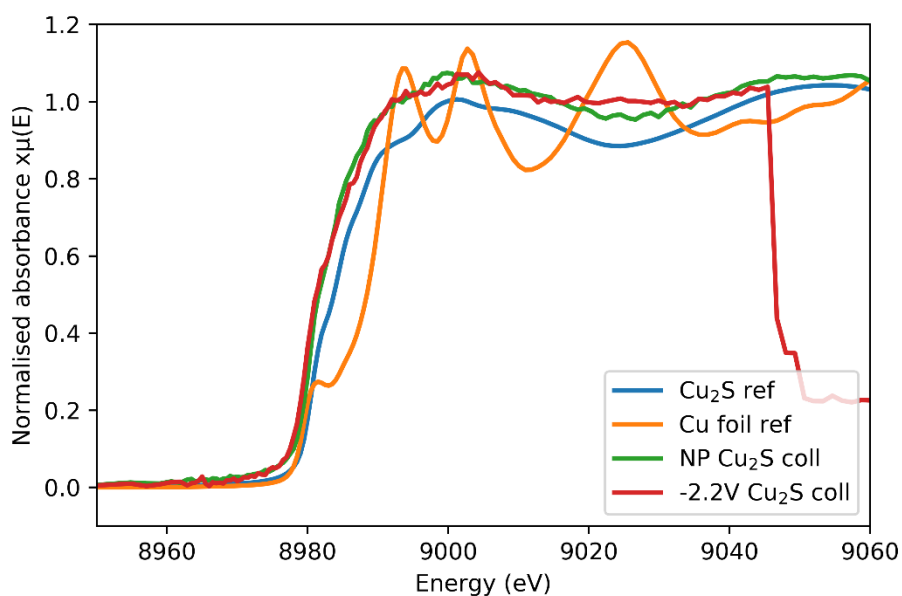
Figure 34: XANES plot of in-situ Cu$_2$S colloidal nanoparticles with no potential and with -2.2V vs Ag/AgCl (3M) applied. No clear reduction of the Cu$_2$S phase is observed. However, a drop in intensity indicates bubble formation at the electrode.

electrolyte, it surfaces due to the lower density of the gas than water. This increases the current again. Apparently, this bubble formation also affects the signal detected. Perhaps the scattering of bubble formation could explain the decrease of signal intensity. Even though this phenomenon is interesting to further research, it is outside the scope of this work. Nonetheless, the bubble formation could attest to the formation of gaseous products. Of which hydrogen is believed to be a major part.

4.3.3 Chronoamperometry experiments

Chronoamperometry (CA) data was also recorded while measuring the in-situ XAFS. In Figure 35 the data for these CA experiments is shown with each point the current after 200 seconds of the corresponding potential. The lines plotted through the data points strictly serve as a guide to the eye. The exponential relation between the potential and the current indicates that the onset potential has been reached; presumably the formation of $H_2(g)$. It is impossible to define an accurate onset potential for each of the catalysts due to the limited data available. However, the onset potential for H_2 with the CuS/GNP sample lies around -0.5V vs RHE.
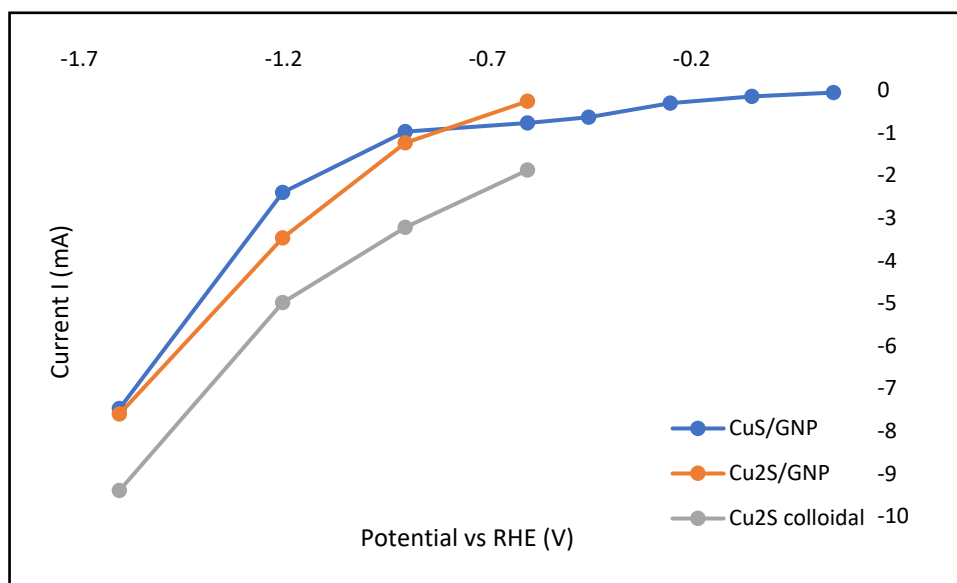

Figure 35: Chronoamperometry results for in-situ XAFS experiments after 200 sec of applying the corresponding potential. The lines plotted through the data points strictly serve as a guide to the eye.

CA was also used to analyse the selectivity of products at certain potentials. An online gas chromatograph analyzed the gas phase during CA. A high-performance liquid chromatograph analyzed the liquid phase after CA. The current flow through the cell was found to be stable within the time frame of the measurement. This suggests that after the reaching the equilibrium current at a certain potential, no degradation of activity was observed. This suggests the stable production of products at the potentials for CA investigation. In Figure 37 a chronoamperometry plot is shown for Cu_2S/GNP and CuS/GNP catalysts. The current flow through the cell was found to be stable up to 8 hours, but because of data loss only the first 4 hours are shown. For this chronoamperometry

experiment at -0.9V vs RHE, formate production was observed for both CuS/GNP and Cu_2S/GNP using HPLC – see Figure 36.
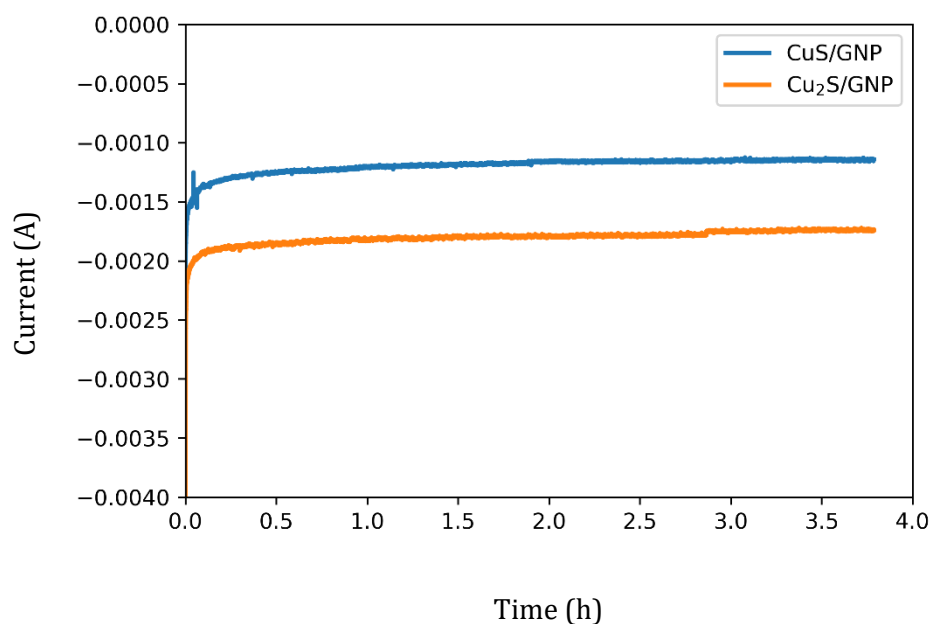
Figure 37: A chronoamperometry plot of Cu_2S/GNP and CuS/GNP catalysts at -0.9V vs RHE. The current flow through the cell was found to be stable for 8h.
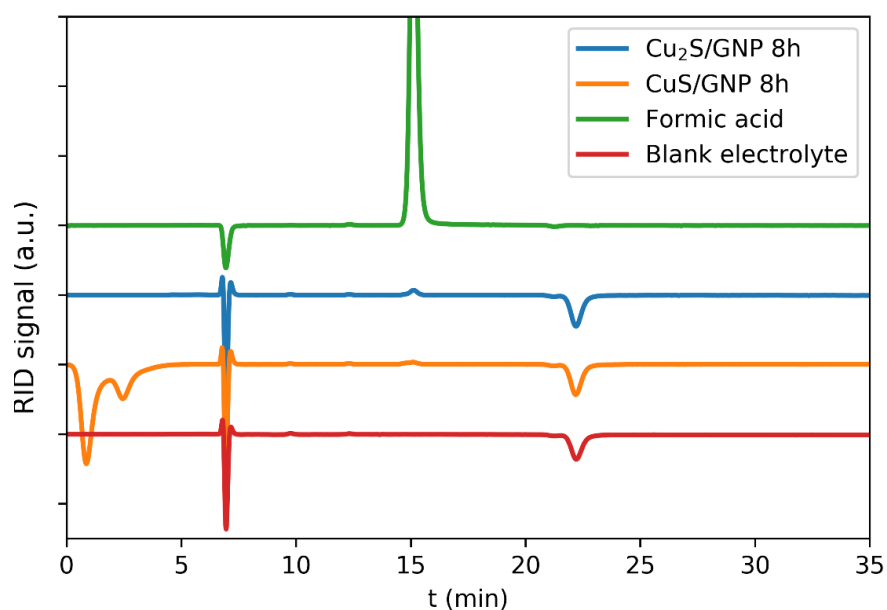

Figure 36: HPLC chromatogram of the impregnated $Cu_{2-x}S$/GNP catalysts after 8h of chronoamperometry at -0.9V vs RHE. Formate production is rather low. The peak at 7 min corresponds to water and the peak at 22 min belongs to the salt-out effect associated with the 0.1M $KHCO_3$ electrolyte.

GC analysis showed no detectable CO_2RR products. But a relatively large amount of H_2 was detected. Unfortunately, the H_2 production was not quantifiable because the GNP support, carbon paper and glassy carbon back end were all active for the HER.

The selectivity for formate production was determined by using the faradaic efficiency. This is the efficiency of how much of charge goes to the production of a certain product with respect to the total charge observed in the cell. This faradaic efficiency was defined as follows;
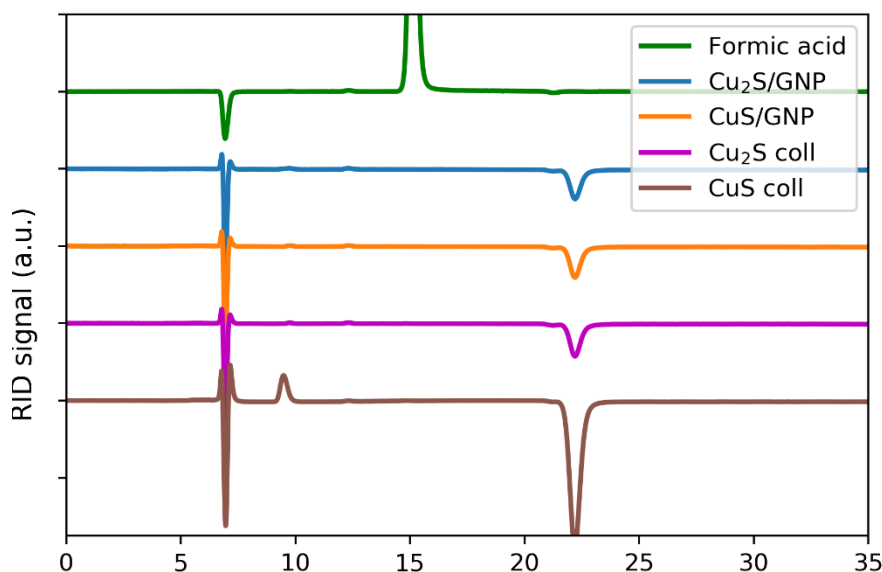
$$FE_x(\%) = \frac{nFQ}{Q_{total}} x\ 100$$

Figure 38: HPLC chromatogram showing electrolyte of CuS colloidal nanoparticles after 2h at -0.5V vs RHE in 0.5M KHCO3 chronoamperometry. No formate forms at this potential. The peak at 10 min and 22 min originate from the salt-out effect of KHCO3 from the electrolyte.

Where Q_{total} determined by integrating the current over time and n the moles of electrons required for producing compound x. Whilst this method calculates lower faradaic efficiencies than using the total amount of products detected instead of Q_{total}, it is a more representative method. For example, faradaic losses are also included. Moreover, the faradaic efficiency is not the best method to report selectivities because of mass transfer limitations that are induced by high potential gradients at the surface of the electrode.[31]

For reduction of one CO_2 molecule to formate, two electrons are required. In Table 3, the faradaic efficiencies are reported corresponding to the chronoamperometry experiments of Figure 37 and the HPLC experiments of Figure 36. These faradaic efficiencies for formate production, 12.1 and 13.1% are rather low as compared to literature where often 80% FE is mentioned at -0.9V vs RHE. [18,19,51,52] But the reason for this is the aforementioned H_2 production by carbon present nearby the electrode. In figure 38, HPLC results are shown for both impregnated and colloidal $Cu_{2-x}S$ catalysts after 2h of CO_2RR at -0.5V vs RHE. However, no formate production is observed in these experiments. Thus, the onset potential of formate production should lie somewhere in the range of -0.5 V vs RHE to -0.9V vs RHE.

Catalyst	Formate production (μmol/h)	Q_{total} (C)	FE$_{HCOO^-}$ (%)	FE$_{H_2}$ (%)	Cu$_{2-x}$S loading (mg/cm²)
Cu$_2$S/GNP 8h	4.28	50.4	13.1	86.9	0.081
CuS/GNP 8h	2.72	34.6	12.1	87.9	0.081

Table 3: An overview of selectivity data for Cu$_2$S/GNP and CuS/GNP as determined with HPLC and Chronoamperometry.

Regarding the colloidal samples, H$_2$ production was also observed. But this was significantly lower than the CuS/GNP sample, see Figure 39. Unfortunately, no HPLC could be performed on the colloidal samples at -0.9V vs RHE due to time constraints. If this was possible then perhaps the high selectivity to formate from Cu$_{2-x}$S nanoparticles could be proven and compared with literature.
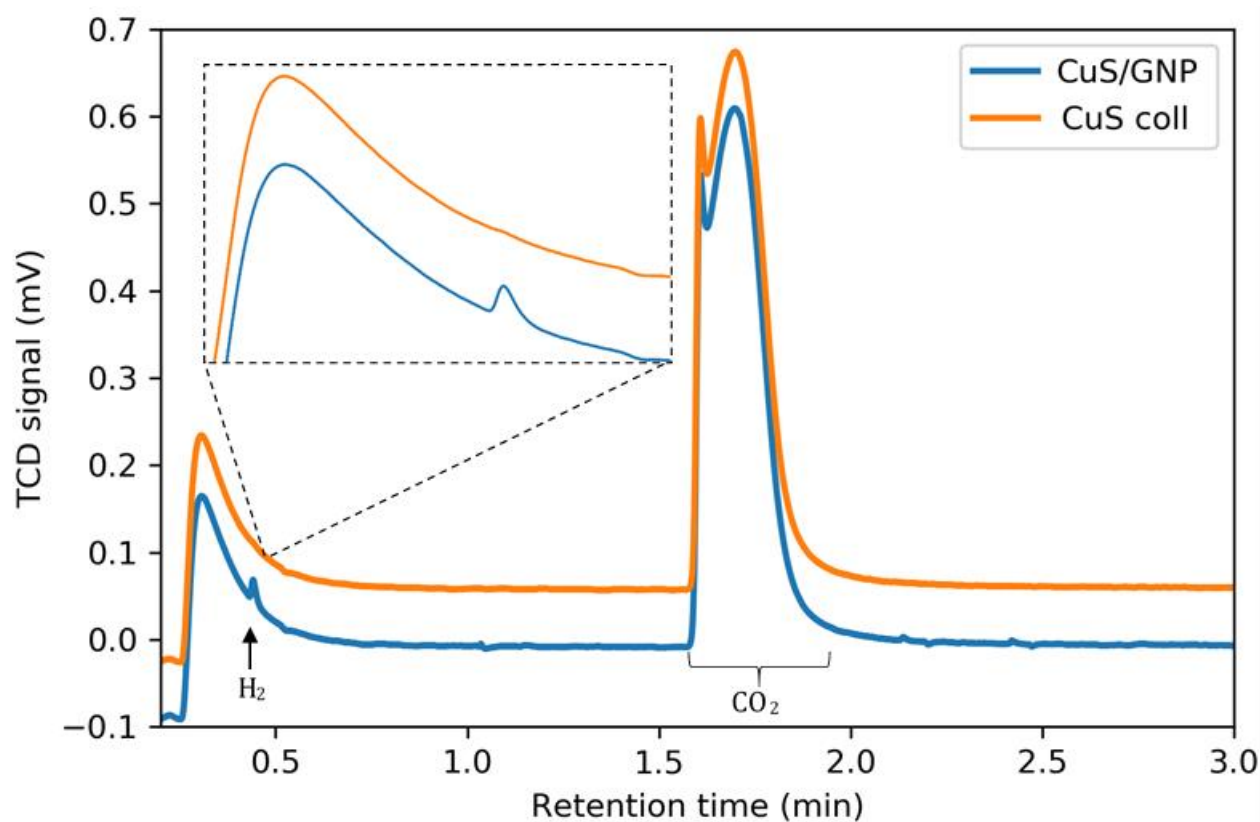

Figure 39: GC chromatogram of CuS/GNP and CuS colloidal nanoparticles at -0.5V vs RHE.

5. Conclusion

To summarize, both Cu_2S and CuS nanoparticles in were synthesized using colloidal and incipient wetness impregnation. With colloidal synthesis, the Cu_2S nanoparticles formed spherical particles with a diameter of 10.2 ± 1.0 nm. CuS favored the formation of nanoplatelets with 8.7 ± 1.4 nm in width and 20.7 ± 2.7 nm in length. The Cu_2S nanoparticles prepared by incipient wetness impregnation on a GNP support were larger than their colloidally prepared analogues (14.5 ± 2.5 nm). CuS/GNP nanoplatelets prepared by incipient wetness impregnation were 15.2 ± 8.9nm wide and 43.7 ± 8.9 nm long respectively. Both CuS and Cu_2S nanoparticles prepared by incipient wetness impregnation demonstrated a more heterogeneous particle size distribution than their colloidal counterparts. XRD analysis affirmed the presence of monophasic Cu_2S/GNP and CuS/GNP nanoparticles.

Subsequent spray pyrolysis and spray drop casting allowed for deposition of the $Cu_{2-x}S$(/GNP) nanoparticles over a carbon paper substrate. This yielded catalyst loaded electrodes for electrochemical evaluation. Analyzing the electrodes with SEM and EDX showed successful and homogeneous deposition of the $Cu_{2-x}S$(/GNP) nanoparticles.

Subsequent cyclic voltammetry revealed the immediate reduction of CuS/GNP nanoparticles when reducing potentials were applied. This was supported by the smell of H_2S(g). However, in-situ XAFS experiments only suggested the reduction of CuS to Cu_2S at approximately -1.2V vs RHE with a minor presence of Cu(s). For Cu_2S reduction was less clear-cut. However, a minor Cu phase seemed to be present according to the XAFS spectra at -1.6V vs RHE.

Once current had stabilized the activity of CO_2RR remained stable for at least 8h. This indicated the stable production of products over time. Selectivity-wise, both Cu_2S/GNP and CuS/GNP produced formate at -0.9V vs RHE with 12% FE. The remainder FE was attributed to HER. With GNP being highly active for HER, the FE for formate production presumably lies significantly higher. The production rate at -0.9V vs RHE for Cu_2S/GNP and CuS/GNP was determined to be 4.28 μmol/h and 2.72 μmol/h respectively. Regarding the colloidal nanoparticles, both $Cu_{2-x}S$ catalysts showed minor HER activity. HPLC was also performed at -0.5V vs RHE for both the colloidal and impregnated $Cu_{2-x}S$ nanoparticles at which no formate production was observed.

6. Outlook

The complex nature of CO_2RR that is inherent to electrochemistry, complicates the characterization of the catalytically active phase of the electrocatalyst. One possible strategy is to use multiple ex-situ analysis techniques to characterize the catalyst both before and after CO_2RR. This was attempted with both XRD and ED. With XRD, the loadings of catalyst on the carbon paper electrode proved to be too low for successful characterization of the crystal phases present. Perhaps, another attempt may be tried to characterize $Cu_{2-x}S$ phases using substantially higher loadings and longer scans to increase the signal-to-noise ratio. Renewed attempts of using ED may also proof fruitful to see if the $Cu_{2-x}S$ phase changed upon CO_2RR for clusters of $Cu_{2-x}S$ colloidal nanoparticles.

Since the catalytically active part of electrocatalysts is the surface, surface probing techniques may be even more effective. A particularly technique of interest is the use of X-ray Photoelectron spectroscopy (XPS). This would be useful in seeing whether there is still sulfide on the surface of the catalyst after CO_2RR, or whether it was reduced and Cu_xO formed upon removing the applied negative potential.

However, structural information of the active phase is best acquired using in-situ characterization techniques. This enables the analysis of the active catalyst before oxidation of catalyst and surface bound species can take effect. Therefore, it would be interesting to further explore in-situ XAFS. A more in-depth study of the reductive behavior of $Cu_{2-x}S$ could be pursued with both the in-situ XAFS and cyclic voltammetry analysis of the catalyst in the same cell.

Another in-situ characterization technique that may be worthwhile to explore is in-situ Surface Enhanced Infrared Absorption Spectroscopy (SEIRAS). Herein, the infrared absorbance of surface bound reaction species can be probed. This yields information about the active phase, reaction intermediates and even the local pH that is paramount for the development of CO_2RR can be determined.[20]

Another important aspect is to make sure that electrochemical analysis is not performed under limitations. The use of electrical impedance spectroscopy (EIS) for example could be used to probe the resistance of the cell used and determine the ECSA as well using double layer capacitance determination. Once a better understanding of electrochemical behavior of the catalysts is established experimenting with different cell designs may benefit activity. The carbon paper substrates as used in the set-ups now for example are designed for a gas diffusion electrode (GDE) role. Nonetheless the electrodes were employed in a H-type cell fashion. Using the flow-cell design allows for better diffusion of CO_2 from one side of the GDE, to the electrolyte side of the GDE. Thus, the low solubility of CO_2 in the high local pH near the electrode surface can be overcome to some extent.[53]

With respect to $Cu_{2-x}S$ as electrocatalyst, there is still a lot of work to be done. Due to time constraints no significant size/composition to function relationships could be established. Also more data on $HCOO^-$ selectivity, activity – using LSV's to construct Tafel plot and stability is preferred to judge $Cu_{2-x}S$ as electrocatalyst. Further investigation of electrolyte specifically regarding pH may also be interesting to suppress HER while optimizing CO_2RR selectivity and activity.

Additionally, with carbon being an excellent support material for fundamental nanoparticle studies, it is hard to find a replacement that does not sacrifice surface area and conductivity for decreased H_2 production. For fundamental study, maybe using Fluorine-doped titanium oxide (FTO) substrates could present more representative FE's for the $Cu_{2-x}S$ nanoparticles. This substrate material is also well suited for spray pyrolysis applications for example.

Finally, even though research to electrocatalysts is rapidly advancing there are still many different interesting materials to evaluate for CO_2RR. For example, bimetallic alloys may be tuned to possess adsorption energies favoring selectivity to certain products whilst retaining stability under reducing conditions. This becomes especially relevant when assessing catalysts for industrial scale where commercially relevant catalysts are supposed to function at ~200 mA/cm^2.[54]

7. Bibliography

(1)   Chorkendorff, I.; Niemandsverdriet, J. W. *Concepts of Modern catalysis and Kinetics*, Second, Re.; Wiley-VCH, 2007.

(2)   Azapagic, A.; Cue, R. M. *J. CO2 Util.* **2015**, *9*, 82–102.

(3)   Von der Assen, N.; Jung, J.; Bardow, A. *Energy Environ. Sci.* **2013**, *6*, 2721–2734.

(4)   Shao, P.; Ci, S.; Yi, L.; Cai, P.; Huang, P.; Cao, C.; Wen, Z. *ChemElectroChem* **2017**, *4* (10), 2593–2598.

(5)   J, Q.; Y, L.; F, H.; J, Z. *Chem Soc Rev* **2014**, *43*, 631–675.

(6)   Hori, Y.; Murata, A.; Takahashi, R. *J. Chem. Soc. Faraday Trans. 1 Phys. Chem. Condens. Phases* **1989**, *85* (8), 2309.

(7)   Hori, Y.,*Kikuchi, k., and Suzuki, S. *Chem. Lett.* **1985**, *14* (11), 1695–1698.

(8)   Hori, Y.; Wakebe, H.; Tsukamoto, T.; Koga, O. *Electrochim. Acta* **1994**, *39* (11–12), 1833–1839.

(9)   Peterson, A. A.; Abild-Pedersen, F.; Studt, F.; Rossmeisl, J.; Nørskov, J. K. *Energy Environ. Sci.* **2010**, *3* (9), 1311.

(10)   Nie, X.; Esopi, M. R.; Janik, M. J.; Asthagiri, A. *Angew. Chemie - Int. Ed.* **2013**, *52* (9), 2459–2462.

(11)   Calle-Vallejo, F.; Koper, M. T. M. *Angew. Chemie - Int. Ed.* **2013**, *52* (28), 7282–7285.

(12)   Gattrell, M.; Gupta, N.; Co, A. *Energy Convers. Manag.* **2007**, *48* (4), 1255–1265.

(13)   Whipple, D. T.; Kenis, P. J. A. *J. Phys. Chem. Lett.* **2010**, *1* (24), 3451–3458.

(14)   Van Der Stam, W.; Berends, A. C.; De Mello Donega, C. *ChemPhysChem* **2016**, *17* (5), 559–581.

(15)   Liu, X.; Wang, X.; Zhou, B.; Law, W.-C.; Cartwright, A. N.; Swihart, M. T. *Adv. Funct. Mater.* **2015**, *23*, 1256–1264.

(16)   Lin, M.-C.; Lee, M. *Electrochem. commun.* **2011**, *13* (12), 1376–1378.

(17)   Mou, J.; Liu, C.; Xu, H.; Song, L.; Wang, J.; Zhang, K.; Chen, Y.; Shi, J.; Chen, H. *Small* **2015**, *11*, 2275–2283.

(18)   Deng, Y.; Huang, Y.; Ren, D.; Handoko, A. D.; Seh, Z. W.; Hirunsit, P.; Yeo, B. S. *ACS Appl. Mater. Interfaces* **2018**, *10*, 28572–28581.

(19)   Zhang, Q.; Zhao, Q.; Liang, X.; Wang, X. *Int. J. Hydrogen Energy* **2018**, *43* (21), 9935–9942.

(20)   Zhuang, T.; Liang, Z.; Seifitokaldani, A.; Li, Y.; Luna, P. De; Burdyny, T.; Che, F.; Meng, F.; Min, Y.; Quintero-bermudez, R.; Dinh, C. T.; Pang, Y.; Zhong, M.; Zhang, B.; Li, J.; Chen, P.; Zheng, X.; Liang, H.; Ge, W.; Ye, B.; Sinton, D.; Yu, S.; Sargent, E. H. **2018**.

(21)   Reske, R.; Mistry, H.; Behafarid, F.; Roldan Cuenya, B.; Strasser, P. *J. Am. Chem. Soc.* **2014**, *136* (19), 6978–6986.

(22)   Ball, D. W. *Physical Chemistry*, 1st ed.; 2003.

(23) Zhibao Huo, Y. L.; Song, Z.; Ren, D. *Thermodynamics of CO2 Electroreduction, in Electrochemical Reduction of Carbon Dioxide Fundamentals and Technologies, 2016, pp. 155–180*; 2016.

(24) Ramette, R. W. *J. Chem. Educ.* **1987**, *64* (10), 885.

(25) Bates, R. G.; Macaskill, J. B. *Pure Appi. Chem.,* **1978**, *50*, 1701—1706.

(26) Eilert, A.; Cavalca, F.; Roberts, F. S.; Osterwalder, J.; Liu, C.; Favaro, M.; Crumlin, E. J.; Ogasawara, H.; Friebel, D.; Pettersson, L. G. M.; Nilsson, A. **2017**, 6–11.

(27) Bard, A. J.; Faulkner, L. R.; Swain, E.; Robey, C. *Fundamentals and Applications*, 2nd ed.; Harris, D., Swain, E., Robey, C., Aiello, E., Eds.; John Wiley & Sons, 2001.

(28) Kortlever, R.; Shen, J.; Schouten, K. J. P.; Calle-Vallejo, F.; Koper, M. T. M. *J. Phys. Chem. Lett.* **2015**, *6* (20), 4073–4082.

(29) Nie, X.; Luo, W.; Janik, M. J.; Asthagiri, A. *J. Catal.* **2014**, *312*, 108–122.

(30) Y, H. *J. Electrochem. soc.* **1983**, *130* (12), 2387–2390.

(31) Yang, K.; Kas, R.; Smith, W. A. **2019**, 1–26.

(32) Xie, H.; Wang, T.; Liang, J.; Li, Q.; Sun, S. *Nano Today* **2018**, *21*, 41–54.

(33) Erdey-Gruz, T.; Volmer, M. *Z. Phys. Chem.* **1930**, *150A*, 203.

(34) Volmer, J. A. V. *Trans. Faraday Soc* **1924**, *19* (729), 734.

(35) Tafel, J. *Phys. Chem.* **1905**, *50A*, 641.

(36) Burstein, G. T. *Corros. Sci.* **2005**, *47* (12), 2858–2870.

(37) Jongh, P. E. De; Donega, C. D. M. *Chem. Mater.* **2018**, *31*, 541–552.

(38) Tu, R.; Pellegrino, T.; Manna, L. *Chem. Mater.* **2015**, *27*, 7531–7537.

(39) Fan, X.; Hua, N.; Xu, J.; Wang, Z.; Jia, H.; Wang, C. *RSC adv.* **2014**, *4*, 16524–16527.

(40) Neuburger, M. C. *Z. Phys.* **1930**, *67*, 845–850.

(41) Kalbskopf, R.; Zemann, F. P. J. *Tsehermaks Min. Petr. Mitt.* **1975**, *22*, 242–249.

(42) Nafees, M.; Ali, S. *J. Nanomater. Biostructures* **2015**, *10* (2), 635–641.

(43) Sadanaga, R.; Ohmasa, M.; Morimoto, N. *Mineral. J.* **1965**, *4* (4), 275–290.

(44) Goldstein, J. I.; Newbury, D. E.; Michael, J. R.; Ritchie, N. W. M.; Scott, J. H. J.; Joy, D. C. *Scanning electron Microscopy and x-ray microanalysis*, 4th ed.; 2003.

(45) Baturina, O. A.; Lu, Q.; Padilla, M. A.; Xin, L.; Li, W.; Serov, A.; Artyushkova, K.; Atanassov, P.; Xu, F.; Epshteyn, A.; Brintlinger, T.; Schuette, M.; Collins, G. E. **2014**.

(46) Web mineral chalcocite http://webmineral.com/data/Chalcocite.shtml#.XKHrQZgzZPY.

(47) Web mineral http://webmineral.com/data/Covellite.shtml#.XKHqRpgzZPY.

(48) Giri, S. D.; Sarkar, A. *J. Electrochem. Soc.* **2016**, *163* (3), 252–259.

(49) Kumar, P.; Nagarajan, R.; Sarangi, R. *J. Mater. Chem.* **2013**, *1*, 2448–2454.

(50)   Stegemeier, J.; Ma, R.; Stegemeier, J.; Levard, C.; Dale, J. G.; Noack, C. W.; Yang, T.; Brownjr, E.; Lowry, G. V. **2014**, No. June.

(51)   Martin, A. J.; Krumeich, F.; Shinagawa, T. *ACS Catal.* **2018**, *8*, 837–844.

(52)   Huang, Y.; Deng, Y.; Handoko, A. D.; Goh, G. K. L. **2018**, No. 110, 320–326.

(53)   Kuhl, K.; Berkeley, L.; Cave, E. *Energy Environ. Sci.* **2012**, *5* (2012), 7050.

(54)   Burdyny, T.; Smith, W. A. *Energy Environ. Sci.* **2018**, *Advance ar*ticle

(55)   Li, C. W.; Ciston, J.; Kanan, M. W. *Nature* **2014**, *508* (7497), 504–507.

(56)   Measurements of the double layer capacitance https://www.bio-logic.net/wp-content/uploads/20101209-Application-note-21.pdf.

(57)   Hjorth, I. Catalysts for electrochemical conversion of CO2 in aqueous solutions, 2017.

8. Acknowledgements

9. Appendices

9.1 Electrochemical surface area determination

Double layer Capacitance

In order to normalize the current I(A) as result of the potential applied to its current density J(mA/cm²). Double layer capacitance was employed. For this a method was adapted to the one reported by Li, C.W. et al.[55]

Assuming the system has a real capacitance and a resistance in parallel, the double layer capacitance is given by the following equation:

$$C_{dl} \frac{dE}{dt} = \frac{I_a - I_c}{2}$$

Where C_{dl} is the capacitance of the electrical double layer,
$\frac{dE}{dt}$ is the scanning rate with which the cyclic voltammogram is recorded in V/s and
I_a and I_c are the corrosion parts of the anodic and cathodic current.

$\frac{dE}{dt}$, I_a and I_c can be determined by cyclic voltammetry near the corrosion potential that is equal to E_{oc}.[56] The contribution of the GNP supports to the C_{dl} is taken care of by subtracting the experimental value for GNP sulfidized blank from the one with catalyst. The resulting value for $C_{dl,Cu}$ then yields an approximation for the exposed Cu surface. Subsequent comparison of the latter value with the C_{dl} of a flat Cu foil with surface area S then allows for approximation of the ECSA A_{ECSA} by the following equation:

$$A_{ECSA} = \frac{C_{dl,Cu}}{C_{dl,Cu\ foil}} \ x\ S$$

In which R_f is the roughness factor where;

$$R_f = \frac{C_{dl,Cu}}{C_{dl,Cu\ foil}}$$

The roughness factors of the catalysts were compared to electrochemically polished Cu foil of which the Capacitance is defined as 1.

Cyclic voltammograms were recorded in the non-faradaic region (no contribution of product formation to current flow in the cell). This is however for each catalyst different. But allows for probing of the capacitance of the electrical double layer on the surface of the active phase. Contributions to this capacitance are not strictly limited to the copper but may well be the result of the high surface area GNP. Thus, the probed capacitance of Cu_xS/GNP and blanc GNP experiment were compared.

Underpotential deposition of Lead

Below the cyclic voltammograms are shown for the underpotential deposition of lead on a colloidal Cu_2S nanoparticle electrode. The figure on the left shows the current vs time for CV scans without $Cu_{2-x}S$ (only the carbon paper substrate). The figure on the right shows the UPD experiment with $Cu_{2-x}S$ nanoparticles. Blue represents the background scan, Orange represents the experiment with lead underpotential deposition. And Green represents the underpotential deposition experiment after subtraction of the background scan → Yielding the net reduction and oxidation of presumably only Pb.

However, since the system was rather complicated (Cu_2S colloidal nanoparticles on carbon paper substrate) it was decided to abandon the experiments. Integration of the Green oxidation peak in the right figure yielded a 0.00241724 C area. Using a 310 μC cm^{-2} conversion factor for monolayer adsorption of Pb atoms on the Cu surface yielded an electrochemical surface area of 7.798 cm^2. This value seems rather low. But the loading of Cu on the electrode was only 0.101 mg/cm^2.
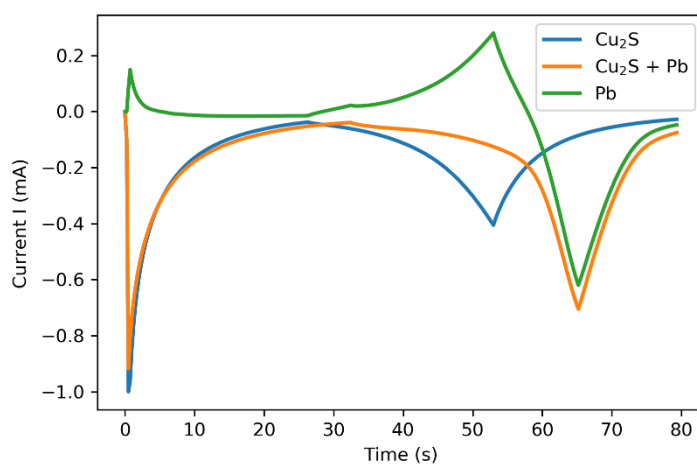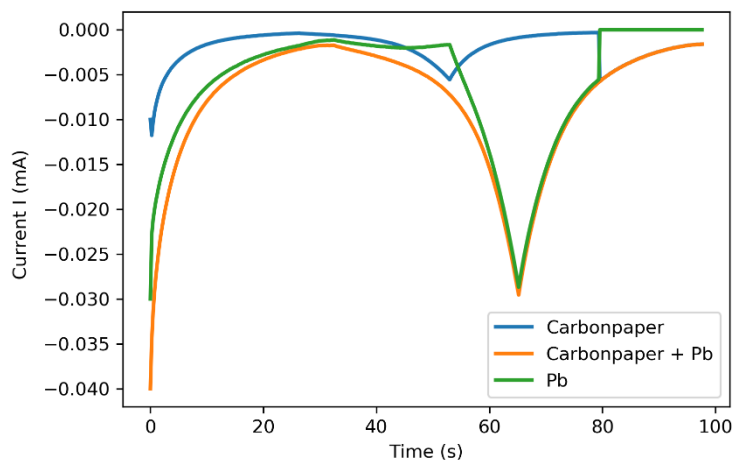
9.2 Gas Chromatography set-up

Concerning the use of aqueous electrolyte for CO_2RR, water vapour commonly posed a problem for selectivity analysis. This water pollution was tackled in two ways:

    1) Installation of filters between reactor and GC
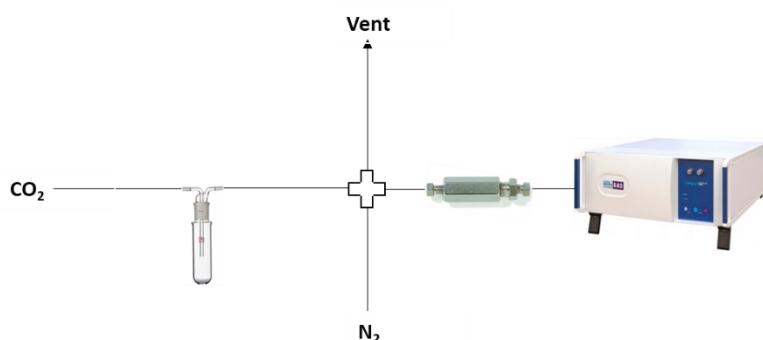
    2) Baking-out of columns and sample loops

The baking out proceeded setting the temperatures of all column and sample loop ovens to 100°C over a weekend. Prior to an ensuing measurement, the system was cooled down to operating temperature by running an analysis method.

Nonetheless water vapour entering the GC remains a problem for longer chronoamperometry experiments. A potential solution is to use a counter-flowing N_2 gas membrane that dries the product stream from reactor to GC.

9.3 Sample overview

In table 4 an overview is included of the samples that have been synthesized and analyzed. In table 5 a more detailed description of the key experiments performed is included.

Code	Sample	Preparation	Analysis performed/Remarks
KH-4	Cu_2S coll/GNP	Sonication, SP	TEM
KH-5	Cu_2S coll/HSAG	Sonication, N.A.*	TEM
KH-6	Cu_2S coll/VC72x	Sonication, N.A.*	SEM/EDX, TEM
KH-7	Cu_2S coll/CNT	Sonication, N.A.*	none
KH-8	Cu_2S coll	SP	SEM/EDX before and after CO_2RR @-1.2V vs RHE, CA, UPD
KH-9	Cu_2S coll	SP	CV
KH-10	Cu_2S coll	SP	CV
KH-11	Cu_2S coll	SP	CV
KH-12	Cu_2S coll	SP/S	CV, CA**, HPLC (-0.5V vs RHE 2h), XAFS, TEM
KH-13	CuS/GNP	SP/S	CV, CA, HPLC (-0.5V vs RHE 2h/-0.9V vs RHE 8h), XAFS, XRD, TEM
KH-14	Cu_2S/GNP	SP/S	CV, CA, HPLC (-0.5V vs RHE 2h/-0.9V vs RHE 8h), XAFS, XRD, TEM
-	Cu_2O/GNP	N.A.	Parent Cu_2S/GNP and CuS/GNP, TEM
-	CuS coll	S	CV, CA, HPLC (-0.5V vs RHE 2h), TEM
-	Cu_2S Na_2S coll	S	CV, CA
-	GNP DDT	S	Heat treated 5.5% NO/N_2(&Ar) @ 350°C and Sulfidized DDT, CA
-	GNP TAA	S	Heat treated 5.5% $NO/N2$(&Ar) @ 350°C and Sulfidized TAA, CV
-	GNP HT	S	Heat treated 5.5% $NO/N2$(&Ar) @ 350°C , **not sulfidized**, CV, CA
-	Carbon paper	N.A.	CV, for comparison to colloidal samples
JW4	Cu_2S coll DDT 8.1 nm	Coll/LE	0.250 g Cu(I)acetate, TOPO 3.702 g, ODE 20 mL, 5 mL DDT, 45 min

Impregnated samples ($Cu_{2-x}S$/GNP – 21 wt% Cu)				
Experiment	**Sample**	**Catalyst used for ink ($Cu_{2-x}S$/GNP)**	**Catalyst loading ($Cu_{2-x}S$/GNP)**	**prep**
CV 0.1M $KHCO_3$	Cu_2S/GNP; CuS/GNP	21.21 mg 20.02 mg	3.26 mg/electrode 3.08 mg/electrode	S
CV 0.5M $KHCO_3$	Cu_2S/GNP; CuS/GNP; GNP HT	20.63 mg 11.57 mg 19.89 mg	3.2 mg/ electrode 0.89 mg/ electrode 1.53 mg/ electrode	S
CV Ar/CO_2 0.25M H_3PO_4	CuS/GNP	20.02 mg	3.08 mg/ electrode	S
CV Ar/CO_2 0.25M H_3PO_4	Cu_2S/GNP Ar Cu_2S/GNP CO_2	20.34 mg 19.55 mg	3.13 mg/ electrode 3.00 mg/ electrode	S
HPLC	Cu_2S/GNP 8h CuS/GNP 8h	20 mg 20 mg	0.081 mg/cm^2 0.081 mg/cm^2	SP
Colloidal samples ($Cu_{2-x}S$ NP's)				
Experiment	**Sample**	**Catalyst used for ink ($Cu_{2-x}S$)**	**Catalyst loading (Cu)**	
SEM -1.2V vs RHE	Cu_2S coll	½ synthesis batch (203 mg $Cu(SO_4)*5H_2O$)		SP
CV 0.5M $KHCO_3$	Cu_2S DDT coll	50 μL	0.21 mg/cm^2	S

	CuS coll	50 µL	0.22 mg/cm^2	
	Cu$_2$S Na$_2$S coll	50 µL	0.027 mg/cm^2	
HPLC	Cu$_2$S coll 2h	50 µL	0.21 mg/cm^2	S
	CuS coll 2h	50 µL	0.22 mg/cm^2	
S abbreviates spray drop casting and SP abbreviates spray pyrolysis				

Loading calculations:

1) Spray drop casting (see section 3.2.1)

For **impregnated catalyst**:

20 mg Cu$_{2-x}$S/GNP x (1/6.5) = 3.08 mg/electrode

$$\xrightarrow{\text{Dividing by 4.9 cm}^2 \text{ surface area electrode}} 0.63 \text{ mg/cm}^2 \text{ Cu}_{2-x}\text{S/GNP}$$

For **colloidal catalyst**:

0.05 mL of synthesis batch per electrode;
- 0.21 mg/cm^2 Cu for Cu$_2$S coll
- 0.22 mg/cm^2 Cu for CuS coll

2) Spray pyrolysis (see section 3.2.2)

For **impregnated catalyst**: 20 mg Cu$_{2-x}$S/GNP over 245.4 cm^2 area → 0.08 mg/cm^2 Cu$_{2-x}$S/GNP

For **colloidal Cu$_2$S DDT:** ½ synthesis batch of 406 mg

9.4 Electron diffraction (ED)

In the figures below electron diffractograms are shown for colloidal Cu_2S nanoparticles before (Figure 40) and after -1.2V vs RHE chronoamperometry (Figure 41) are shown. The AuPd calibration diffractograms are also included (Figure 42).
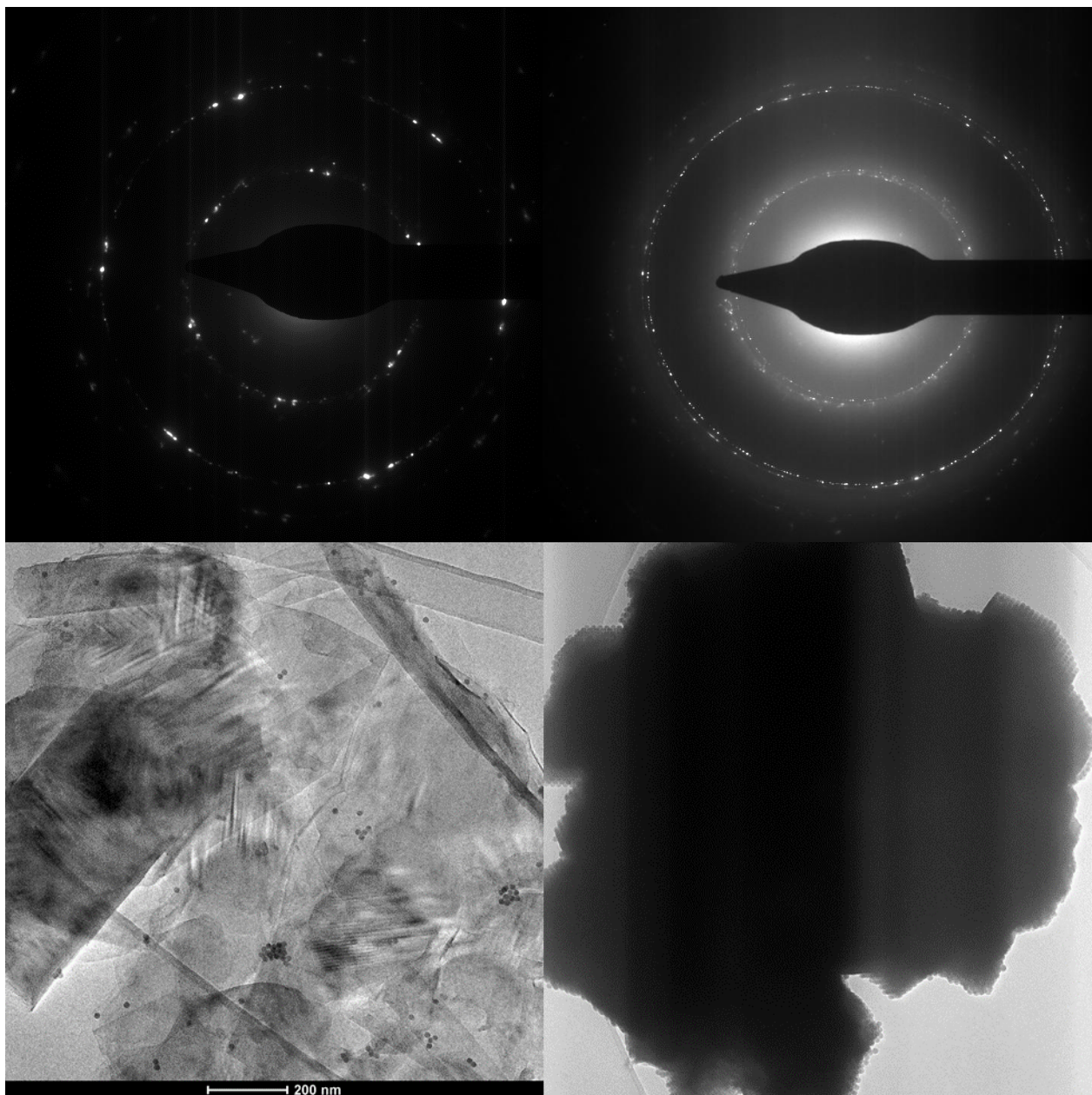

Figure 40: Electron diffractograms with their corresponding TEM images below for Cu₂S colloidal nanoparticles after synthesis.
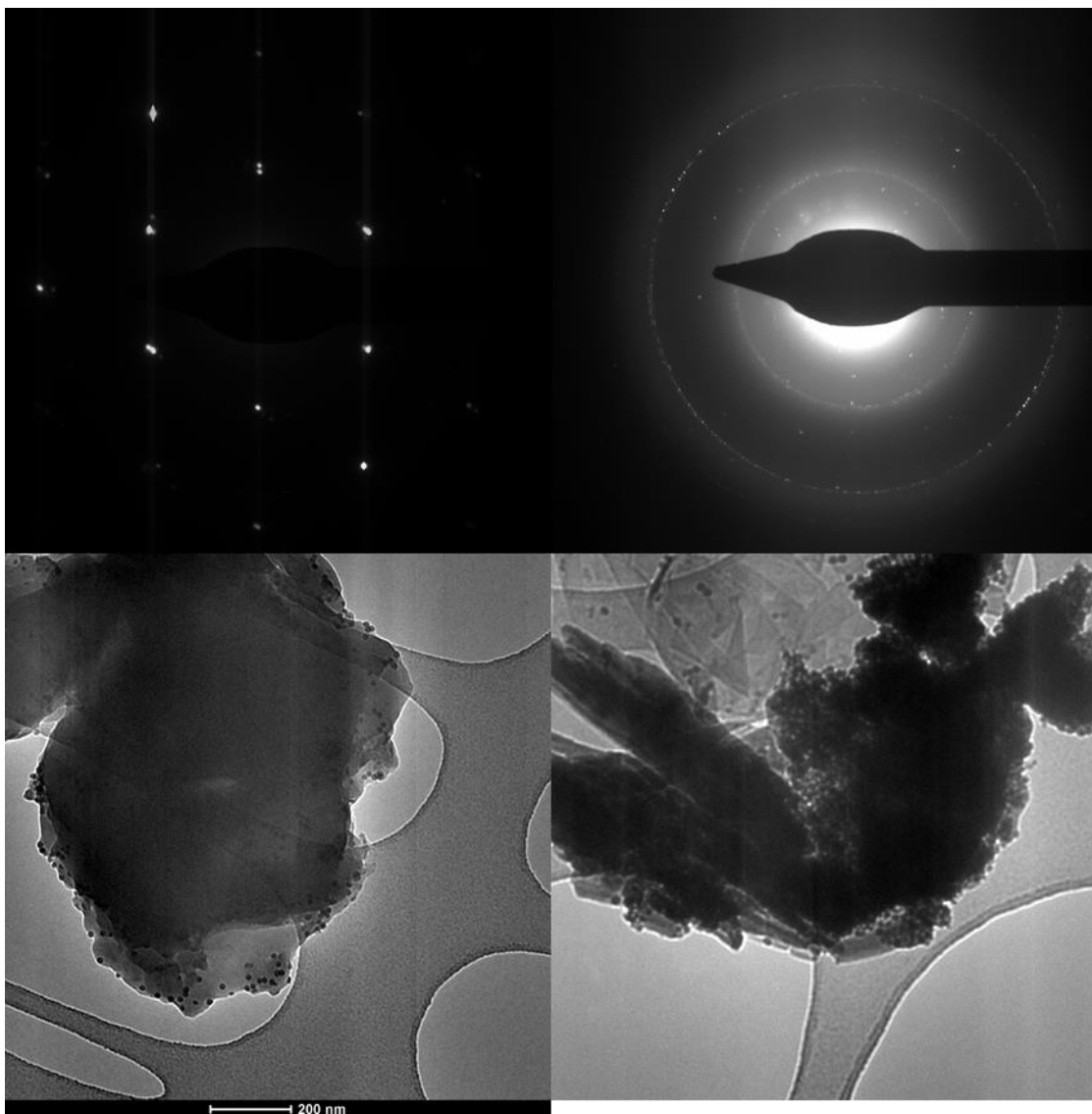
Figure 41: Electron diffractograms and their corresponding TEM pictures of the same Cu2S colloidal nanoparticles after having been loaded on an electrode and used for CO2RR @ -1.2V vs RHE.
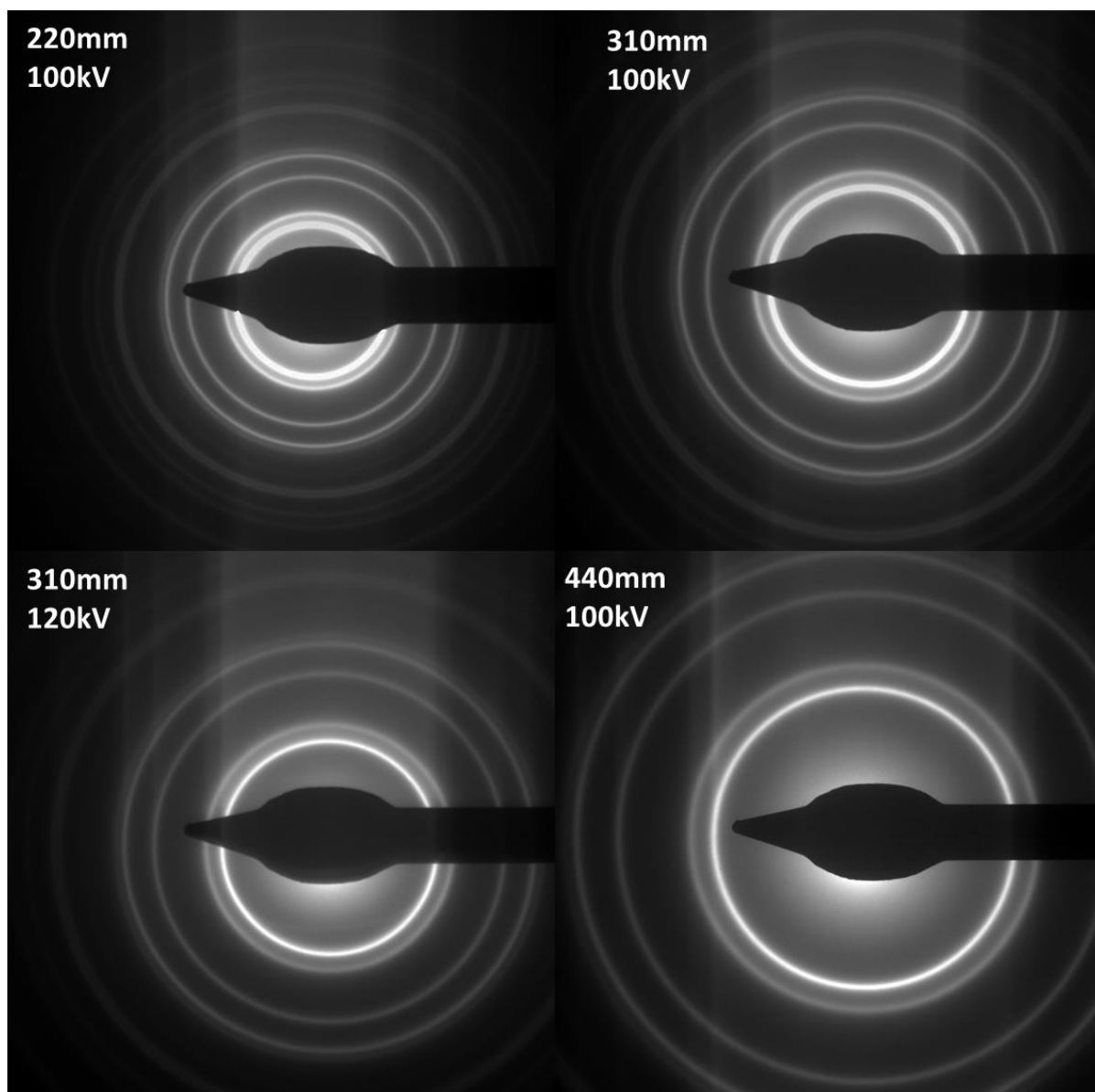
Figure 42: Electron diffractograms for AuPd with cross grating length shown.

9.5 Platinum as counter electrode

During the research, questions were raised if using Platinum as counter electrode may produce flawed results. The reason for this is that Platinum is not entirely stable and can form oxidized species. These oxidized species may deposit either on the proton exchange membrane or diffuse entirely through this membrane and deposit on the working electrode. If this occurs, the reduction/oxidation current may be higher than is the actual case for faradaic processes. Alternatively, the deposited platinum may contribute to CO_2RR/HER. All the above is undesired. But since no platinum deposition on the working electrode was registered with EDX, it was decided keep using a platinum counter electrode.